

This is a non peer reviewed preprint submitted to EarthArxiv.

*This paper is now published in G3. Please refer to that
version. <https://doi.org/10.1029/2023GC011025>*

Geophysical and Geochemical Constraints on Magma Storage Depths along the Cascade Arc: Knowns and Unknowns

Penny E Wieser^{1,2*}, Adam J.R. Kent², Christy B. Till³, Geoff A. Abers⁴

1. **Corresponding author:** Penny_wieser@berkeley.edu, 541–908–4572. Department of Earth and Planetary Sciences, McCone Hall, UC Berkeley, 94720, USA
2. College of Earth, Ocean and Atmospheric Sciences, Oregon State University, 97331, USA
3. School of Earth and Space Exploration, Arizona State University, Tempe, AZ 85281, USA
4. Earth and Atmospheric Sciences, Cornell University, Ithaca, NY 14850, USA

We have submitted to G3 (geochemistry, geophysics, geosystems).

We welcome any feedback – think we've missed a study? Think we've misrepresented your work? Please let us know! That is why we are posting a preprint (email penny_wieser@berkeley.edu)

1 **Geophysical and Geochemical Constraints on Magma Storage Depths along the Cascade Arc:**
2 **Knowns and Unknowns**

3 Penny E Wieser^{1, 2*}, Adam J.R. Kent², Christy B. Till³, Geoff A. Abers⁴

4 1. **Corresponding author:** Penny_wieser@berkeley.edu, 541–908–4572. Department of Earth and
5 Planetary Sciences, McCone Hall, UC Berkeley, 94720, USA

6 2. College of Earth, Ocean, and Atmospheric Sciences, Oregon State University, 97331, USA

7 3. School of Earth and Space Exploration, Arizona State University, Tempe, AZ 85281, USA

8 4. Earth and Atmospheric Sciences, Cornell University, Ithaca, NY 14850, USA

9 **Key Points (140 characters or less)**

10 1. The availability of magma storage depth constraints along the Cascade arc is highly variable and not
11 well correlated to volcano threat level.

12 2. Available geophysical and geochemical constraints cluster at 0–15 km depth ($\sim 2 \pm 2$ kbar), consistent
13 with global compilations.

14 3. Investigating the potential for deeper storage of the most mafic magmas will require studies
15 accounting for melt inclusion vapour bubble CO₂.

16 **Abstract (can only be 250 words)**

17 The iconic volcanoes of the Cascade arc stretch from Lassen Volcanic Center in northern California,
18 through Oregon and Washington, to the Garibaldi Volcanic Belt in British Columbia. Recent studies
19 have reviewed differences in the distribution and eruptive volumes of vents, as well as variations in
20 geochemical compositions and heat flux along strike (amongst other characteristics). We investigate
21 whether these along-arc trends manifest as variations in magma storage conditions. We compile
22 available constraints on magma storage depths from InSAR, geodetics, seismic inversions, and
23 magnetotellurics for each major edifice, and compare these to melt inclusion saturation pressures,
24 pressures calculated using mineral-only barometers, and constraints from experimental petrology. The
25 availability of magma storage depth estimates varies greatly along the arc, with abundant geochemical
26 and geophysical data available for some systems (e.g. Lassen Volcanic Center, Mount St. Helens), and
27 very limited data available for other volcanoes, including many which are classified as “very high threat”
28 by the USGS (e.g., Glacier Peak, Mount Baker, Mount Hood, Three Sisters). Acknowledging the
29 limitations of data availability and the large uncertainties associated with certain methods, available
30 data is indicative of magma storage within the upper 15 km of the crust ($\sim 2 \pm 2$ kbar) beneath the main
31 edifices. These findings are consistent with previous work recognising barometric estimates cluster
32 within the upper crust in many arcs worldwide. There are no clear offsets in magma storage between
33 arc segments that are in extension, transtension or compression, although substantially more
34 petrological work is needed for fine scale evaluation of storage pressures.

35 **Plain language summary**

36 The Cascade arc contains a number of large volcanoes which present a significant hazard to human
37 populations and infrastructure (e.g., Mount St. Helens, Mount Rainier). Until now, there has been no
38 wide-scale review of where magma (molten rock) is stored in the crust beneath these volcanoes, even
39 though understanding where magma is stored is very important to help monitor unrest at these
40 volcanoes and to predict future activity. We compile all available data on magma storage for each
41 volcano, and find that there are many volcanoes have had very few studies investigating them, despite
42 the risk they pose to society. The available data (albeit sparse) suggests that most magma is stored at
43 0–15 km depth before eruption.

44 **Introduction**

45 Determining the depths at which magmas are stored in continental arcs is a key parameter to help
46 inform models of the formation and evolution of the continental crust (e.g., Ducea et al., 2015; Lee and
47 Anderson, 2015; Rudnick, 1995), as well as to aid our understanding of volcanic eruptions and hazards.
48 For example, precise determinations of magma storage depths help to distinguish between end-
49 member models, where magmas may be distributed in a mush zone spanning the entire crust
50 (Cashman et al., 2017), or concentrated in distinct magma storage reservoirs, such as Kilauea Volcano,
51 (Poland et al., 2014; Wieser et al., 2021) and Benzmianny Volcano (Turner et al., 2013). Magma
52 storage depths also influence the eruptive style, size and frequency of volcanic eruptions (Huber et al.,
53 2019), and can be used to help interpret signals of volcanic unrest in monitoring data (Pritchard et al.,
54 2019). Integration of petrological and geophysical constraints on magma storage depths was also
55 identified as vital to improve our understanding of magma storage, staging and transport by the
56 Subduction Zones in 4D (SZ4D) initiative (Hilley et al., 2022).

57 The Cascade arc presents an interesting case study to investigate magma storage depths, because of
58 the wide variability in volcano morphology, magma compositions, and parameters relating to magma
59 production along the arc (Hildreth, 2007; Till et al., 2019). The Cascade arc trends North-South along
60 the Western margin of the US and Canada, forming as the result of the eastward subduction of the Juan
61 de Fuca and Gorda plates beneath the North American plate. Quaternary activity in the Cascades has
62 occurred at >2300 individual vents, with at least 30 topographically prominent edifices representing
63 longer-lived magmatic systems (Hildreth, 2007). These larger edifices stretch from Lassen Peak in
64 North California (USA) to Mount Meager in British Columbia (Canada) along an approximately linear
65 trend, erupting mostly intermediate and silicic magmas (Fig. 1). The more distributed off-axis fields of
66 smaller, often monogenetic vents are characterized by more mafic compositions (O'Hara et al., 2020).
67 In addition to activity focused around the arc axis, there are also three prominent rear-arc
68 volcanoes/volcanic fields (Simcoe Mountains, Newberry Volcano, and Medicine Lake; Donnelly-Nolan
69 et al., 2008; Hildreth and Fierstein, 2015; Sherrod et al., 1997). This off axis volcanism is thought to be
70 associated with the impingement of the Basin and Range extensional province on the eastern limit of
71 Cascade volcanism (Guffanti and Weaver, 1988; Priest et al., 2013).

72 Volcanism in the Cascades presents a significant societal hazard. Fourteen Cascade edifices have
73 been active since the late Holocene. 11 are classified by the USGS National Volcanic Threat
74 assessment as "Very High Threat" (Mount St. Helens, Mount Rainier, Mount Shasta, Mount Hood,
75 Three Sisters, Lassen Volcanic Center, Newberry Volcano, Mount Baker, Glacier Peak, Crater Lake;
76 Ewert et al., 2018), while Mount Adams and Medicine Lake are listed as "High Threat" (Fig. 1).

77 Over the last few decades, a number of studies have reviewed various aspects of Cascade volcanism
78 on an arc-scale. Hildreth (2007) provided a comprehensive summary of the number, location, and
79 distribution of Quaternary vents, along with descriptions of eruptive activity and approximate volume
80 estimates of different vents along the arc. Poland et al. (2017) reviewed geodetic data collected over
81 several decades in the Cascades to investigate the diverse causes of surface deformation. From a
82 geochemical perspective, Schmidt et al. (2008) and Pitcher and Kent (2019) reviewed the major, trace
83 and isotopic composition of samples to assess compositional variability along the arc. Integrating
84 geophysics and geochemistry, Till et al. (2019) examined variations in erupted volumes and
85 compositions, heat budget, and seismic velocities along the Cascade arc to investigate the influence of
86 crustal processes (e.g., tectonic stress state) vs. mantle processes (e.g., magma generation, variations
87 in subduction parameters, mantle wedge dynamics) on Cascade variability.

88 While geophysical and petrological studies have been performed at individual centres to investigate the
89 pressures, temperatures and timescales associated with the magmatic plumbing system, there has
90 been no detailed arc-scale review of magma storage conditions. A brief compilation was presented by
91 Dufek et al. (2022, their Fig. 3). However, data sources and uncertainty associated with each estimate
92 were not discussed, and we have identified many additional constraints, both from the literature and
93 our own petrological calculations. Based on the correlation between low seismic phase velocities and
94 crustal heat flow, Till et al. (2019) suggest that crustal seismic structure and heat flow are primarily
95 controlled by magmatic processes and advection of heat occurring in the upper mantle/deepest crust,
96 and that the flux of mantle-derived basalt varies by a factor of two along strike in the Quaternary

97 Cascades. In ocean-island basalts, it has been shown that volcanoes with longer repose periods (a
98 proxy for magma supply rate) are characterized by deeper magma storage (Gleeson et al., 2021). This
99 correlation may indicate that large melts fluxes are required to maintain active crustal storage reservoirs
100 in the cooler upper crust. Thus, it may be expected that shallower magma storage depths are found in
101 regions of the arc with higher mantle supply. Alternatively, magma storage in the Cascades may be
102 controlled by crustal processes such as the crustal stress state, prominent lithological or density
103 boundaries within the crust (Chaussard and Amelung, 2014), or magmatic H₂O contents (Rasmussen
104 et al., 2022).

105 Numerous methods have been used to determine magma storage depths in the Cascades and
106 elsewhere. These can broadly be subdivided into geophysical and petrological methods. One common
107 petrological method is thermobarometry, which relies on pressure-sensitivity of the exchange of
108 chemical components within a single mineral, between two minerals, or between minerals and the liquid
109 from which they crystallize or re-equilibrate with (see Putirka, 2008). In the Cascades, equilibrium
110 between clinopyroxene and liquid (Cpx-Liq), clinopyroxene-orthopyroxene (Cpx-Opx), and amphibole-
111 liquid (Amp-Liq), as well as liquid compositions themselves have been used to determine magma
112 storage conditions (e.g., Blundy, 2022; Hollyday et al., 2020; Scruggs and Putirka, 2018). Melt inclusion
113 barometry is another petrological technique that has been applied to the Cascades (e.g., Aster et al.,
114 2016; Ruscitto et al., 2010; Wright et al., 2012), which relies on the strong relationship between pressure
115 and the concentration of CO₂ and H₂O in a volatile-saturated silicate melt (e.g., Dixon, 1997; Ghiorso
116 and Gualda, 2015; Shishkina et al., 2014). After measuring the volatile (and major element) contents of
117 melt inclusions (MIs) at the time at which these pockets of melt were trapped within crystals, a mixed
118 fluid solubility model can be used to calculate the minimum pressure at which the magma was volatile
119 saturated. Finally, experimental petrology can be used to determine the conditions of magma storage,
120 by comparing the chemistry of erupted products to experiments conducted at varying pressure,
121 temperature, fluid compositions (e.g., Mandler et al., 2014; Quinn, 2014).

122 Various geophysical methods for imaging magma bodies have been applied to the Cascades.
123 Magnetotellurics is used to image the conductivity structure of the crust, which can help identify regions
124 of melt and fluid, as well as hot intrusions (e.g., Bedrosian et al., 2018; Bowles-Martinez and Schultz,
125 2020). Seismic tomography using natural earthquakes or controlled sources (e.g., Kiser et al., 2016;
126 Moran et al., 1999; Ulberg et al., 2020; Zucca and Evans, 1992) and methods that use the ambient
127 seismic noise wavefield (e.g., Flinders and Shen, 2017; Heath et al., 2018; Jiang et al., 2023) have
128 been used to probe the elastic velocity structure of the crust. Seismic wave velocities are sensitive to
129 composition and mineralogy, temperature, and the presence of melt or other fluids, while the attenuation
130 of seismic waves is relatively more sensitive to temperature and fluids (Abers and Hacker, 2016; Magee
131 et al., 2018).

132 A variety of geodetic methods (e.g., tilt, levelling, GPS and InSAR; Dzurisin et al., 2009; Mastin et al.,
133 2008; Poland et al., 2017) can be used to identify changes in the ground surface around volcanoes,
134 which can help identify intrusion of new magma into the crust. Seismicity also provides an indicator of
135 deformation associated with magma movement, delineating pathways of magma transport (e.g., Jones
136 and Malone, 2005). However, as for petrological methods, many caveats exist for these geophysical
137 methods. For example, ground deformation and earthquakes can arise from both volcanic and tectonic
138 processes (Dzurisin et al., 2006; Jones and Malone, 2005; Poland et al., 2006), and it can be difficult
139 to robustly distinguish crustal velocity and conductivity anomalies from magma, hot but solidified
140 intrusions, and other compositional variations such as sedimentary units (e.g., Bedrosian et al., 2018
141 vs. Flinders and Shen, 2017; Bowles-Martinez and Schultz, 2020).

142 Here, we compile available geophysical and geochemical magma storage depths for the main Cascade
143 volcanic centres (Fig. 1). We anticipate that this review will serve several purposes. Firstly, it can be
144 used as a reference of available storage depths at each volcano. Perhaps more importantly, it is very
145 helpful to identify high threat volcanoes where data is very sparse, and future work should be prioritized.

146 [Methods](#)

147 When compiling and collating magma storage depths along the arc into a single coherent database, it
148 is important to ensure consistency between published depth estimates from different volcanoes. We
149 discuss the approaches used below for each proxy to ensure consistency along-arc.

150 **Mineral barometry**

151 For mineral-melt barometry, we compile Amp and Cpx compositions from a wide variety of studies,
152 along with a smaller number of matched Opx-Cpx analyses. In many cases, we could not obtain
153 contextual information of whether the analysis was taken at a core or rim. A notable exception is the
154 data of Streck and Leeman, (2018) who overlay their measurements on thin section images. One
155 problem with literature compilations of mineral compositions is that a number of published analyses are
156 labelled as Cpx are actually Amp or Opx or vice versa. To automatically sort through these, we use a
157 sklearn support vector classification machine learning algorithm (linear kernel) trained on a compilation
158 of pyroxenes, feldspars, amphiboles, apatites, olivines and oxides. Analyses classified as pyroxenes
159 are further filtered to only use analyses with cation sum between 3.95 and 4.05, and Ca/(Ca+Mg+Fe)
160 ratios between 0.2 and 0.5 for Cpx and 0–0.06 for Opx (excluding pigeonites). We filter out Amp with
161 cation sums outside of 15–16. All thermobarometry and filtering calculations were performed using the
162 open-source Python3 tool Thermobar (Wieser et al., 2022).

163 Cpx-based barometry in the Cascades has utilized a variety of models to convert measured phase
164 compositions into pressures (and temperatures). Hollyday et al. (2020) and Scruggs and Putirka (2018)
165 use the Cpx-Liq barometry of Neave and Putirka (2017) iterated with the Cpx-Liq thermometer of Putirka
166 (2008, eq33). Sas et al. (2017) use the Cpx-Liq barometer from Putirka (2008, eq32c) with an
167 unspecified thermometer. However, applying different Cpx-Liq barometry equations to the same Cpx-
168 Liq pairs yield pressures that can differ by 3–12 kbar (~10–45 km, see Wieser et al., 2023b), which is
169 an offset equivalent to the entire thickness of the Cascade crust (~10–45 km, Das and Nolet, 1998).
170 Additionally, Cpx-Liq barometry relies on identifying or reconstructing a liquid composition in equilibrium
171 with each Cpx composition (Scruggs and Putirka, 2018), which is challenging in arcs where whole-rock
172 compositions may not necessary represent true liquids (Kent et al., 2010) and many equilibrium tests
173 perform badly (Wieser et al., 2023b). Given that Cpx-only and Cpx-Liq barometers show similar
174 performance for a dataset of arc-like experimental products (Wieser et al., 2023b), we avoid melt-
175 matching complications by using the Cpx-only barometers of Jorgenson et al. (2022, hereafter J2022)
176 and Wang et al. (2021 eq1, hereafter W2021). These two Cpx-only barometers show the best RMSE
177 and R^2 values (J2022: $R^2=0.78$, RMSE=1.9 kbar, W2021: $R^2=0.66$, RMSE=2.4 kbar) and least
178 systematic error when applied to the ArcPL experimental dataset consisting of several hundred
179 experiments relevant to arc magmas conducted at 0–17 kbar which were not used in model calibration
180 (Wieser et al. 2023b). These RMSE mean that these two Cpx-only barometers can identify magma
181 storage depths within a window spanning ~15–18 km at 1σ confidence. The relatively thick crust in the
182 Cascades (~40–50 km, Jiang et al., 2023; Kiser et al., 2016; Parsons et al., 1998; Shehata and
183 Mizunaga, 2022) means that Cpx-based barometry can roughly distinguish between storage in the
184 upper, mid and lower crust at best. Another advantage of these two barometers is that they are
185 independent of temperature and H₂O content, which are difficult to estimate from Cpx compositions
186 alone (Wieser et al., 2023b). An additional complication with literature compilations is that the quality of
187 mineral analyses in our compilation is not known, as publications do not quote the analytical precision
188 of each measurement. Analytical uncertainty related to the measurement of Na₂O in pyroxene can
189 easily yield errors spanning 3–5 kbar on each individual Cpx measurement (Wieser et al., 2023a).
190 Averaging multiple Cpx compositions at each volcano can help to mitigate these random analytical
191 errors (Putirka et al., 1996), and results in a substantial improvement when applied to the experimental
192 data investigated by Wieser et al. (2023b). Thus, we predominantly focus on median pressures
193 calculated for each volcano.

194 Identifying equilibrium Amp-Liq pairs is even more challenging than for Cpx-Liq, because the only
195 widely-used equilibrium test to assess equilibrium is the exchange of Fe-Mg (K_D^{Fe-Mg}). Tests on
196 experiments in the ArcPL dataset not used to calibrate the Amp-only barometer of Ridolfi (2021,
197 hereafter R2021) performs moderately well (RMSE=2.7 kbar, $R^2=0.67$), as long as extreme care is
198 taken to ensure that the barometer is being used within the P-T-X limits of the calibration (Wieser et al.,
199 2023c). When displaying Amp-only pressures, grey kernel distributions and black crosses show
200 amphiboles that pass the compositional filters of Ridolfi (2021, Fig. 2–12). We also apply an additional
201 filter to remove Amp with atomic proportions on the basis of 13 cations >6.8 for Si, and <1.1 for Al,
202 which lie outside the calibration range of the Ridolfi model (these filtered pressures are shown with a
203 green kernel distribution and grey crosses, Fig. 2–12, see supporting Fig. S1–2). In general, these two
204 additional filters remove Amp with the lowest calculated pressures, pushing the median pressure

205 substantially deeper. A large number of Amp at Lassen (N=260, Fig. 2) are excluded using this filter,
206 affecting the interpretation of magma storage, but at other volcanoes this filter has a minor influence on
207 the median pressure.

208 For Cpx-Opx, we calculate pressures by iterating Putirka (2008) eq36(T)-eq39(P) and eq37(T)-eq39(P).
209 Using a new dataset of arc mineral and liquid compositions not used to calibrate such models (Wieser
210 et al., 2023a, 2023b) we find that these two-pyroxene barometers behave poorly for Cpx with $Mg\# < 0.68$,
211 so we filter out such pairs. Even for $Mg\# > 0.67$, it should be noted that Cpx-Opx barometry has a large
212 RMSE (3.7-4.1 kbar).

213 Blundy (2022) released a liquid-only thermobarometry method to calculate temperature, pressure and
214 fluid composition (X_{H_2O}) from the composition of a liquid saturated in Cpx-Amp-Opx-Plag-Magnetite-
215 Ilmenite (CHOMPI). They examine experiments specific to Mount St. Helens, and produce an empirical
216 expression which can be used more generally to obtain the conditions of storage of CHOMPI-saturated
217 magmas. They apply this method to the youngest rocks erupted from 16 Cascade volcanic centers.
218 However, no independent test dataset was used by Blundy (2022) to assess the performance of this
219 model, and the influence of false positives was not widely assessed (e.g., the algorithm classifying the
220 liquid as CHOMPI-saturated when it was not). By coding CHOMPI into Python3 (available in Thermobar,
221 Wieser et al. 2022a), we are able to perform such independent tests. Using the same criteria Blundy
222 (2022) use for the Cascades, CHOMPI calculations in Thermobar returned a false positive rate of ~46%,
223 and a very poor relationship between experimental and CHOMPI pressure (Fig S3, see Text S1, Fig.
224 S3). Thus, we do not discuss the results from this method further.

225 We also compile experimental constraints where directly relevant to a specific Cascade edifice. We
226 quote these pressures as published.

227 [Melt inclusion saturation pressures](#)

228 Solubility models can be used to estimate the pressure at which a melt with a given major element
229 composition, volatile content and temperature becomes volatile-saturated. Thus, assuming a melt
230 inclusion was trapped from a volatile-saturated magma, the pressure at the time of melt inclusion
231 entrapment can be calculated. However, Cascade MI studies have used a wide variety of solubility
232 models (see Supporting Table S1). Because the calibration datasets of many of these models span a
233 limited compositional range, calculated saturation pressures can easily differ by a factor of two or more
234 (Wieser et al., 2022b). Thus, the use of different models at different volcanoes adds considerable
235 uncertainty when comparing depths determined from different research groups over different time
236 periods, both of which influence the choice of model. For consistency, we use published major element
237 and volatile contents to recalculate all saturation pressures using the solubility model MagmaSat
238 implemented in the Open-source Python3 tool VESlcal (Iacovino et al., 2021); Wieser et al. (2022b)
239 show that this model best recreates experimental data for andesitic and dacitic compositions, and has
240 the largest calibration dataset of all available models.

241 MI saturation pressures have other limitations. If crystals are growing and trapping melt inclusions
242 during storage in the crust, the distribution of melt inclusion saturation pressures will reveal the main
243 magma storage regions. However, melt inclusions can also form during ascent towards the surface,
244 because degassing of H_2O is often accompanied by crystallization (Applegarth et al., 2013; Lipman et
245 al., 1985). This can result substantial 'smearing' of saturation pressures towards shallower pressures.
246 It is also becoming increasingly apparent from Raman spectroscopic analyses that a large proportion
247 of the total CO_2 in a MI is held within the vapour bubble in olivine-hosted MIs in arc magmas (e.g.
248 Mironov et al., 2020; Moore et al., 2018, 2015). Accurate Raman measurements require each laboratory
249 to carefully determine the relationship between Raman spectral features and CO_2 densities using an
250 optical apparatus where CO_2 gas is held at varying pressure conditions and temperature is closely
251 controlled (DeVitre et al., 2021; Lamadrid et al., 2017), or reference materials are obtained from a
252 laboratory where they were measured with an optical apparatus (e.g., Mironov et al., 2020, Wieser et
253 al., 2021). Only the MI vapour bubbles from two cinder cones near Lassen Peak by Aster et al. (2016)
254 have been measured on a calibrated Raman system. Venugopal et al. (2020) perform Raman
255 measurements but use a literature calibration line rather than an instrument-specific calibration. The
256 large number of their bubbles measured at room temperature with reported CO_2 densities above the
257 thermodynamical limit indicates that their calibration may have overestimated CO_2 densities (DeVitre et

258 al., 2023). Other studies reconstruct vapour bubbles using bubble growth models (Johnson and
259 Cashman, 2020; Walowski et al., 2019). However, these reconstructions require a precise estimate of
260 the amount of post-entrapment crystallization (PEC) experienced by MIs, which in turn, requires
261 accurate estimates of the initial FeO_t content of each MI (Danyushevsky and Plechov, 2011). Estimating
262 initial FeO_t is very challenging for monogenetic cones, where the fractionation path is uncertain because
263 only a very narrow range of liquid compositions were erupted. The remaining studies of olivine-hosted
264 MIs do not measure or reconstruct the vapour bubble (e.g. Ruscitto et al., 2010; Walowski et al., 2016).
265 As a result, saturation pressures obtained from published MI data must be interpreted with extreme
266 caution, due to uncertainty regarding total CO_2 contents.

267 To obtain a self-consistent database, we calculate saturation pressures using bubble CO_2 from Aster
268 et al. (2016) for MI saturation pressures, and bubble + glass reconstructions from Venugopal et al.
269 (2020), with the important caveat that the Venugopal et al. (2020) Raman measurements may have
270 overestimated CO_2 because of the absence of an instrument-specific calibration. We do not use
271 modelled bubble reconstructions, because of the wide variability of different approaches used, and the
272 sensitivity of these methods to reliable estimates of the amount of PEC, H_2O -loss etc, which we do not
273 have sufficient data to reliably estimate for many datasets. Thus, it is important to recognise that the
274 pressures shown for the mafic MI from studies other than Aster et al. and Venugopal et al. are very
275 much minimum estimates, and the pressures would likely increase dramatically if bubble CO_2 were
276 accounted for. For more silicic melt inclusions, it is very difficult to assess the possible influence of the
277 vapour bubble, given a lack of available measurements globally.

278 Trends at a single volcano

279 Ideally, we would look at trends in magma storage through time at each volcano, and variations in
280 storage as a function of magma chemistry. Where possible, we split data by major volcanic phase (e.g.,
281 Fig. 2 – Lassen domefield vs. Brokeoff Volcano). We also indicate the mineral hosting melt inclusions
282 (e.g., Ol-hosted melt inclusions indicate storage of the most mafic magmas, Qtz-hosted the most silicic).
283 Determining the relationship between storage and magma composition is particularly challenging with
284 Cpx and Amp barometry. Given that magma mixing is ubiquitous in the Cascade arc, minerals were
285 erupted in a silicic magma cannot be assumed to have grown in that composition magmas (and vice
286 versa for minerals erupted in a mafic magma). In Figs. S3–S8, we show Cpx barometry results plotted
287 against Cpx Mg# and grouped by study. No robust trends appear, although there is a possible hint that
288 the most mafic magmas are indeed stored deeper. We show using experimental data that calculating
289 liquid compositions from Amp to compare to pressures generates spurious trends, because similar Amp
290 components are used to calculate chemistry and pressure (Supporting Fig. S4). Detailed work at each
291 edifice would be required to resolve differences in magma storage as a function of magma chemistry
292 that are not apparent in our literature compilation.

293 Calculating depths and reconciling different reference levels

294 Melt inclusion saturation pressure and mineral barometers yield pressures, which are then converted
295 to depths (H) using assumptions about crustal density (e.g., $P=\rho gH$, or a crustal density model).
296 Cascade MI and thermobarometry studies have used a wide variety of crustal densities to convert
297 pressures into depths in the crust ($\rho=2200 \text{ kg/m}^3$ by Bacon et al., 1992, $\rho=2700 \text{ kg/m}^3$ by Hollyday et
298 al., 2020, $\rho=2800 \text{ kg/m}^3$ by Johnson and Cashman, 2020, $\rho=2200 \text{ kg/m}^3$ for the first 2 km and $\rho=2800$
299 below that by Gardner et al. 1995). Here, we convert pressures to depths using a uniform crustal density
300 of $\rho=2700 \text{ kg/m}^3$.

301 In contrast, geophysical methods generally determine depths relative to a variety of reference levels.
302 We abbreviate these as: below sea level (bsl), below ground level (bgl), below average station level
303 (basl), or reference level unknown (rlu). When comparing geophysical depths to one another, and to
304 petrological estimates, it is important to account for different reference levels. For consistency, we adjust
305 all measures to yield depth below the summit of each volcano. This means that geophysical estimates
306 will match petrological estimates if the magma chamber is centrally-located. However, given evidence
307 for magma reservoirs being offset from the volcanoes summit (Lerner et al. 2020), this correction could
308 lead to a systematic offset between petrological and geophysical estimates. To allow visual assessment
309 of these possible offsets, we include a topographic profile across each major edifice on each diagram,
310 extracted from the ASTER global digital elevation model V003 using QGIS (NASA/METI/AIST/Japan

311 Space systems And U.S./Japan ASTER Science Team, 2019; QGIS.org, 2022). Petrological and
312 geophysical estimates could be displaced from one another by a vertical distance equivalent to the
313 maximum height of the topographic profile.

314 Seismic data coverage

315 To obtain the km-scale resolution required to image magma bodies using seismic or magnetotelluric
316 methods, it is normally necessary to obtain data using short-term high-density array deployments (e.g.,
317 Bedrosian et al., 2018; Kiser et al., 2018; Zucca and Evans, 1992). At relatively well-monitored
318 volcanoes such as Mount Rainier and Mount St. Helens, these arrays can be used in conjunction with
319 permanent volcano-monitoring networks (e.g., Moran et al., 1999; Ulberg et al., 2020; Waite and Moran,
320 2009). To help conceptualize the evolution in the quality and amount of seismic data available at
321 different volcanoes, we plot the position of seismometers within ~20 km (0.18°) of the summit of each
322 major edifice. We display this data on a map and a timeline for each major US Cascade volcano (Fig.
323 2–14). The underlying station metadata was pulled from the IRIS GMAP server (<http://ds.iris.edu/gmap/>)
324 and the Pacific Northwest Seismic Network (PNSN) compilation (<https://pnsn.org/seismograms/map>,
325 both updated, Sept 5th, 2022, <http://ds.iris.edu/gmap/>). We classify stations based on their station code
326 as 1 component short period (1sp), 3 component short period (3sp) or 3 component broadband (3bb).
327 Short-period stations are often older, analog-telemetered with limited dynamic range. Waveform-based
328 measurements (such as ambient noise tomography, receiver functions, attenuation measurements)
329 tend to be challenging using this data. Those stations are most useful for local earthquake travel-time
330 tomography (e.g., Moran et al., 1999). Newer broadband stations, generally installed in the mid-late
331 2010's, provide more imaging options.

332 As permanent monitoring networks are densified and older 1– or 3–component seismometers are
333 replaced with modern broadband seismometers, the potential for a new generation of imaging using
334 only permanent installations increases (both through increased station density, and the potential for
335 wavefield-based imaging methods using broadband data). For example, broadband data enables
336 ambient-noise imaging, which provides high-accuracy estimates of shear-wave velocity (V_s) at the
337 upper-crustal depths where magma storage frequently occurs (e.g., Crosbie et al., 2019; Jiang et al.,
338 2023). We also summarize the presence and depth of Deep Long Period earthquakes (DLPs, Nichols
339 et al., 2011), although exactly how these signals relate to the volcanic plumbing system is still enigmatic.

340 Results

341 Data coverage varies widely along the Cascades (Fig. 1–15). Some edifices such as Mount St. Helens
342 have an abundance of petrological and geophysical studies using a variety of methods (seismics,
343 magnetotellurics, geodetics, Fig. 10). Some volcanoes are relatively well studied using one method but
344 not the other (e.g., very little petrology but moderate to good geophysical coverage at Newberry and
345 Mount Rainier, Fig. 7, Fig. 12), while other volcanoes have very little data from either method (e.g.,
346 Three Sisters, Glacier Peak, Fig. 6, Fig. 13). The variability of available data reflects a combination of
347 the heavy focus of research efforts on certain volcanoes (particularly for petrology), quiescence or noisy
348 geophysical signals at certain centres (Poland et al., 2017), and often-insurmountable issues
349 associated with permitting any monitoring equipment within protected wilderness areas and parks
350 (Moran and Benjamin, 2021). It is interesting that there is no apparent correlation between the estimated
351 threat level or ranking out of all US volcanoes and the availability of data (Ewert et al., 2018. Fig. 1).

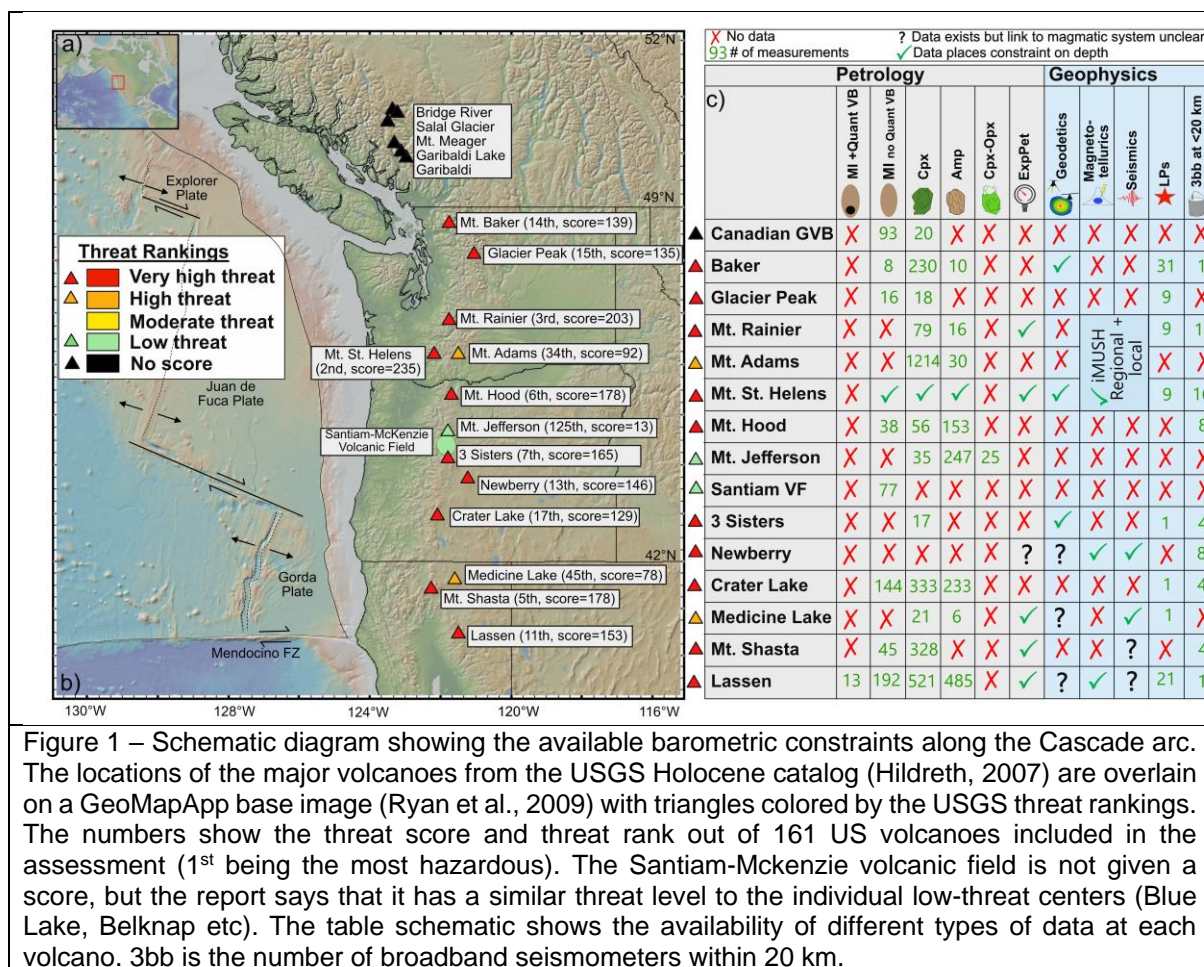


Figure 1 – Schematic diagram showing the available barometric constraints along the Cascade arc. The locations of the major volcanoes from the USGS Holocene catalog (Hildreth, 2007) are overlain on a GeoMapApp base image (Ryan et al., 2009) with triangles colored by the USGS threat rankings. The numbers show the threat score and threat rank out of 161 US volcanoes included in the assessment (1st being the most hazardous). The Santiam-Mckenzie volcanic field is not given a score, but the report says that it has a similar threat level to the individual low-threat centers (Blue Lake, Belknap etc). The table schematic shows the availability of different types of data at each volcano. 3bb is the number of broadband seismometers within 20 km.

352

353 **Lassen Volcanic Center**

354 Activity at Lassen Volcanic Center is subdivided into three main eruptive stages: 1) the Rockland
 355 Caldera Complex (825 – 609 ka), 2) Brokeoff Volcano (590 – 385 ka), and 3) the Lassen domefield
 356 (~300 ka to present, Clynne et al., 2008). Three dominant Holocene eruptions have occurred during the
 357 Lassen domefield stage; Chaos Crags (~850 AD, Clynne et al., 2008), Cinder Cone (1666 AD,
 358 Sheppard et al., 2009), and Lassen Peak (1914–1917 AD; Clynne, 1999). There are also abundant
 359 mafic cinder cones within the Lassen segment of the Cascades, with both calc alkaline and tholeiite
 360 compositions (Walowski et al. 2019).

361 **Mineral Compositions:** Unpublished Cpx compositions were obtained from M. Clynne and B. Platt for
 362 samples from a range of formations from Brokeoff Volcano as described in Bullen and Clynne (1990)
 363 and Clynne et al. (2008). These include andesites from the Diller sequence (470–385 kyrs ago, e.g.,
 364 Rice Creek, Mount Diller) and the Mill Canyon sequence (470–590 kyrs, Clynne and Muffler, 2010).
 365 Platt (2020) measured core-rim traverses for Cpx crystals from Brokeoff Volcano. We extract core and
 366 rim compositions from these profiles, except for the longest traverses, where we extract core,
 367 intermediate and rim analyses for Cpx-only calculations.

368 Underwood et al. (2012) analyse Amp from the several Lassen domefield stage eruptions for hydrogen
 369 isotopes, water contents and ferric/ferrous ratios and major elements which we use for Amp-only
 370 barometry (N=316). These units represented by these analyses are the ~35 ka Kings Creek unit, 28.3
 371 ka dacite dome on Lassen Peak, 850 AD Chaos Crags, and 1914–1917 AD Lassen Peak.

372 Hollyday et al. (2020) perform Cpx-Liq thermobarometry calculations on samples from a cinder cone
 373 from the basaltic-andesite of Box Canyon (middle Pleistocene age). They combine N=20 core analyses
 374 with a primitive MI composition from the basalt of Big Lake (BBL) from Walowski et al. (2016), and
 375 obtain pressures of 460–700 MPa using the Cpx-Liq barometer of Neave and Putirka (2017). However,

376 we were not able to obtain the exact liquid composition used by the authors and could not recreate
377 these pressures. Considering all PEC-corrected MIs from BBL, we instead obtain pressures distributed
378 between -0.5 to ~2.5 kbar (regardless of the exact equilibrium tests used). This discrepancy makes the
379 inference from Hollyday et al. (2020) of lower crustal storage difficult to validate.

380 Overall, Cpx-only barometry using W2021 yields median pressures of ~0.6 kbar for Brokeoff volcano,
381 and ~1.9 kbar for the Lassen domefield. Pressures using J2022 are slightly deeper compared to W2021
382 for both formations (median=1.4 kbar for Brokeoff, 2.6 kbar for the domefield). These deeper pressures
383 likely result from the fact that extra-tree regression strategies used by J2022 never yield negative
384 numbers, skewing averages towards anomalously high pressures. If Amp-only pressures are calculated
385 using just the filters of Ridolfi (2021), the median pressure is 1.2 kbar. However, if we also discard
386 amphiboles with Al and Si cation fractions outside the range of the calibration dataset, we obtain
387 substantially higher pressures (3.2 kbar). We favour the deeper, more extensively filtered median
388 pressures (~3.2 kbar), as none of the experiments used to calculate the R2021 barometer were
389 performed at <1.3 kbar. Overall, considering the errors on these methods, Amp- and Cpx-only
390 barometry are broadly consistent with magma storage in the upper ~0.5 to 4 kbar of the crust at Lassen
391 Volcanic Center. It is possible that a small number of erupted minerals originated deeper, but this is
392 hard to distinguish from uncertainty given the lack of analytical metadata (Wieser et al. 2023a).

393 **Melt inclusions:** The majority of melt inclusion measurements in mafic samples have focused on the
394 cinder cones surrounding Lassen, rather than the main edifice. Saturation pressures may be
395 representative of the storage depths of the most mafic magmas supplied to the edifice. Aster et al.
396 (2016) analyse olivine-hosted MIs from two cinder cones near Lassen (Basalt of Round Valley Butte -
397 BRVB, and Basalt of old Railroad Grade – BORG), measuring CO₂ and H₂O in the melt phase using
398 FTIR, and performing the first measurements of vapour bubble CO₂ in the Cascades using Raman
399 Spectroscopy. The limited number of MIs where both the bubble was measured, and the MI was large
400 enough for FTIR analyses means that there are only N=9 analyses from BORG and N=4 analyses from
401 BRVB where both phases were directly measured in the same inclusion. In addition to direct Raman
402 measurements, Aster et al. (2016) produce a model to reconstruct vapour bubble CO₂, tracking the
403 volume of a growing vapour bubble during post-entrapment crystallization using volume and density
404 information from crystallization simulations in rhyoliteMELTS (Gualda et al., 2012). The composition of
405 the vapour phase in the modelled bubble volume was then calculated using the solubility model of
406 Iacono-Marziano et al. (2012). While there is a broad correlation between modelled and reconstructed
407 vapour bubble CO₂ contents when all samples are considered (Cascades, Parícutin, and Jorullo), the
408 correlation for Lassen samples is poor ($R^2=0.01$, gradient = 0.09). Model-reconstructed values both
409 over and underestimate the amount of CO₂ measured by Raman spectroscopy, and there is no clear
410 association between this discrepancy and whether the bubble contained carbonates. We suggest that
411 discrepancies between Raman measurements and models may result from large uncertainties in
412 determining the exact amount of post-entrapment crystallization experienced by each MI (which
413 controls the calculated bubble volume), as well as the quench rate, and the amount of H₂O loss. The
414 reconstructions of Aster et al. use Petrolog3 to perform post-entrapment crystallization corrections,
415 which requires the user to estimate the initial FeO_t content of each MI, a quantity that is very challenging
416 to estimate in volcanic fields/systems where there is no single liquid line of descent. This is particularly
417 true at Lassen, where different eruptive centres have a wide range of FeO_t contents at similar MgO
418 contents (Clynne, 1999). Thus, we do not calculate pressures for the Aster et al. (2016) MIs where they
419 reconstruct the bubble using their model, and only consider those where the bubble was directly
420 measured by Raman spectroscopy.

421 Walowski et al. (2016) perform FTIR measurements of olivine-hosted MIs (N=115) from a wide variety
422 of Quaternary cinder cones in a large volcanic field surrounding Lassen Peak. Walowski et al. (2019)
423 perform FTIR measurements of olivine-hosted MIs from the 1666 CE eruption of Cinder Cone. Neither
424 study performed direct vapour bubble CO₂ measurements, but Walowski et al. (2019) performed
425 reconstructions using the method of Aster et al. (2016). Specifically, they calculated the amount of PEC
426 assuming an initial FeO_t content of 7 wt%. However, as described above, a similar method perform
427 poorly for the Lassen samples of Aster et al. (2016), and is very sensitive to the amount of PEC (and
428 thus the initial FeO_t content of the melt inclusion). Cinder Cone lavas and tephra samples have FeO_t
429 contents ranging from 5.5–7 wt%. Using Petrolog3, MI LCC-9–OL-01 has experienced 9.9 wt% PEC if

430 reconstructed to 7 wt% FeO, but only 2.8 % PEC if reconstructed to 5.5 wt% FeO (most MIs have
431 differences of 6–7 % PEC). The resulting change in temperature (ΔT), and therefore the volume of the
432 bubble, and the total mass of bubble CO_2 , is 2.5x less if FeO is set at 5.5 wt% vs. 7 wt%. Given the
433 large uncertainties associated with bubble reconstructions, we only show measured H_2O - CO_2 contents
434 for Walowski et al. (2016, 2019) MIs, with the caveat that they are very much minimum estimates.

435 When all MI saturation pressures are recalculated using MagmaSat (Ghiorso and Gualda, 2015), the
436 measurements of Aster et al. (2016) yield pressures spanning 1.4–5.5 kbar. Melt-only saturation
437 pressures from Walowski et al. (2016, 2019) are significantly shallower, as expected, and are likely not
438 a useful constraint on magma storage.

439 The only melt inclusion constraint on storage beneath the main edifice comes from FTIR analyses of
440 Qtz-hosted MIs from the Chaos Craggs rhyodacite by Quinn (2014). Discarding MIs with <3 wt% H_2O
441 which they suggest have undergone leakage, leaves 34 MIs, which yield pressures of ~1–2 kbar.
442 Vapour bubbles are not mentioned in this study, so it is difficult to assess the impact of bubbles on CO_2
443 contents. If these vapour bubbles are CO_2 -poor, these results may indicate that more evolved magmas
444 are stored at shallower depths than the regional basaltic magma supply examined by Aster et al. (2016).

445 **Experimental Petrology:** Schwab and Castro, (2007) perform H_2O -saturated experiments to
446 determine pre-eruptive storage conditions for the dacitic pumice erupted in 1915 from Lassen Peak.
447 Comparison of natural and experimental products indicate that the dacitic magma equilibrated at 0.5
448 kbar and 800–875°C prior to mixing with an andesitic end member. Quinn (2014) perform H_2O -saturated
449 experiments to assess the pre-eruptive storage conditions of the rhyodacitic magma erupted at Chaos
450 Craggs. By comparing textures and phase assemblages in natural samples with experimental products,
451 they infer that the most probable conditions of magma storage for these silicic magmas were 1.45 ± 0.25
452 kbar and $770 \pm 10^\circ\text{C}$.

453 **Geophysics:** The first geophysical interpretation of magma storage under Lassen Volcanic Center
454 came from Benz et al. (1992), who used teleseismic P wave arrival times to investigate lithosphere
455 structure in northern California. They invoked a low-velocity zone (average -7.2%) beneath Lassen
456 Volcanic Center (as well as Medicine Lake) within Layer 1 of their model, which spans 0–15 km depth.
457 More precise depth estimates cannot be obtained from such teleseismic models. However, the low is
458 displaced 30–50 km NE from Lassen, and extends to depths of 70 km, perhaps as an artifact of vertical
459 smearing (Thurber et al., 2009). Park and Ostos (2013) show P-wave tomography from an MSci thesis
460 (Reeg, 2008) investigating measurements conducted using the Sierra Nevada EarthScope project
461 (2005–2007) which imaged a 600 km x 150 km area, with Lassen National Park in the north. They
462 identify a low velocity zone, although they cannot determine whether it is a mantle or crustal feature
463 based on the wide station spacing (Park and Ostos, 2013). Overall, these teleseismic studies do not
464 have sufficient resolution to reliably image small crustal magma chambers beneath Lassen Peak.

465 Park and Ostos (2013) examine a 250-km long broadband and long period magnetotelluric line “LASS”
466 along the 40.5°N parallel. This survey line passes 20 km north of Lassen Peak (40.488 °N). No large
467 crustal conductor was observed beneath Lassen Peak, supporting our assertion that the teleseismic
468 studies described above cannot provide useful constraints on upper crustal magma storage. However,
469 they do identify three small conductors within the Lassen Volcanic Center at ~15–30 km (rlu, presumed
470 bsl), which they suggest are basaltic reservoirs that may heat and melt the lower crust.

471 Another possible constraint comes from a compilation of the depths of earthquakes recorded from 1984
472 to 2016 (see Fig. 6b of Taira and Brenguier, 2016). These depths show a prominent peak at ~4–6 km
473 (rlu). Such high-frequency or volcano-tectonic earthquakes require brittle (velocity-weakening)
474 conditions, indicating temperatures far below the solidus, and are usually seen at a few km from sites
475 of eruption (e.g., White and McCausland, 2016). The simplest interpretation is that the main magma
476 storage region must be deeper than this high-frequency seismicity.

477 Pitt et al. (2002) report the depths of N=20 long-period earthquakes ranging from ~12–27 km depth
478 (basl), which may represent magma recharge (indicating that the main magma storage region is above
479 these). The absence of further seismic constraints at Lassen results from the fact that the permanent

480 network is very small (Fig. 2f-g), and that no high-resolution study has even been performed in the
 481 region.

482 Unfortunately, geodetic measurements at Lassen Volcanic Center do not help constrain magma storage
 483 depths. Lassen Volcanic Center has experienced broad, regional subsidence since 1992, consistent
 484 with a point source at ~ 8 km depth. However, the source of this subsidence is unclear, with dominant
 485 contributions likely from regional extension, changes in the location of hydrothermal/magmatic fluids,
 486 and a possible minor influence of the cooling and crystallization of a magma body (Parker et al., 2016;
 487 Poland et al., 2004). Regional GPS will likely be vital to deconvolve the relative role of crustal extension
 488 compared to hydrothermal and magmatic processes. Given the ambiguity, we do not include this
 489 deformation source on Fig. 2.

490 **Summary and future work:** Cpx-only and Amp-only barometry, Qtz-hosted MI saturation pressures,
 491 and available experimental constraints indicate that the majority of magma storage surrounding Lassen
 492 is within the upper crust (<4 kbar, <15 km). These depths are not inconsistent with the distribution of
 493 shallow earthquakes thought to overly the magma chamber, but further geophysical constraints from
 494 short-term high-density arrays, and/or the addition of more broadband seismometers providing an
 495 opportunity for passive-source tomography, would help to confirm the location of the shallow magma
 496 reservoir. Based on the downward spread of Cpx-only and Amp-only pressures, the presence of higher
 497 saturation pressures from Aster et al. (2016), and the seismic results of Park and Ostos (2013), further
 498 work is certainly needed to investigate whether there is deeper magma storage of more mafic magmas.
 499 This could be targeted through a study focusing on vapour bubble CO₂ in a large suite of melt inclusions,
 500 experiments on relevant starting compositions, or a local high resolution seismic survey.

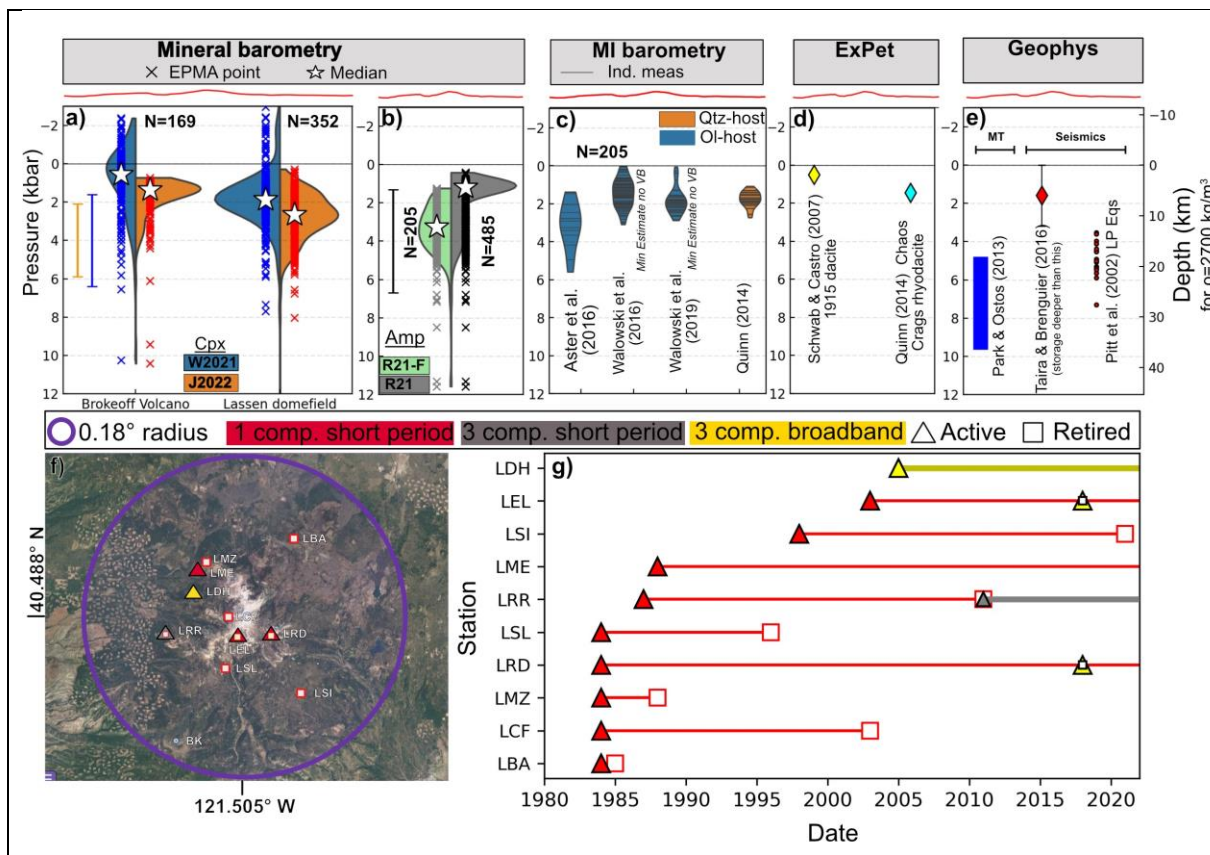


Figure 2: **Compilation of magma storage depths at Lassen Volcanic Center (a-e) and summary of the seismic network (f-g).** Violin plots show the distribution of pressures estimated from Cpx and Amp barometry, with individual pressures shown as crosses, and the median pressure shown with a white star. We overlay the \pm RMSE of each barometry method estimated using a dataset of arc magmas not used in model calibration (Wieser et al. 2023b,c). The depth axis on a-e) is relative to the volcanoes summit. The red profile shows the height above sea level (the top of the chart) across a W-E section spanning 15 km section transecting the summit. As we could not obtain the exact earthquake catalog used by Taira and Brenguier (2016), we show the peak of their histogram \pm the

minimum and maximum values present with error bars. Magma is likely stored deeper than these earthquakes (red diamond). f) Map of seismic stations within 0.18° (~ 20 km) of Lassen Peak's summit. g) Schematic showing seismic station types vs. time (lines changing color show station upgrades), within a circle with radius of 0.18° of the latitude and longitude shown on f). Data from IRIS.org.

501

502 **Mount Shasta**

503 The position of Mount Shasta west of the Cascade arc axis and only ~ 70 km above the subducting plate
 504 means that it could be considered a fore-arc volcano (Christiansen et al., 2017; McCrory et al., 2012).
 505 Mount Shasta is a composite edifice, mostly comprised of five cones (Sand Flat, Sargents Ridge, Misery
 506 Hill, Hotlum and Shastina, Christiansen et al., 2020) which have a primarily calc-alkaline, high-silica-
 507 andesitic to low-silica-dacitic composition (60–67 wt% SiO_2). Quenched mafic inclusions of more MgO-
 508 rich magma are common. The last 10 kyr of eruptive history at Mount Shasta indicates that eruptions
 509 occur every 600–800 years, with the most likely hazards being ash, lava flows, domes, pyroclastic flows
 510 and debris flows (Christiansen et al., 2017; USGS, 2022). Tephra is rare, with most pyroclastic deposits
 511 resulting from dome collapse (Christiansen et al., 2020). In addition to the main volcanic edifice, Mount
 512 Shasta is surrounded by a number of basaltic-andesite to andesitic shields (Ash Creek Butte, The
 513 Whaleback, Deer Mountain, Miller Mountain etc.), and less common basaltic to basaltic-andesitic cinder
 514 cones (Christiansen et al., 2017). While the majority of erupted material has a more evolved
 515 composition, small amounts of primitive magnesian andesite (PMA), high magnesian andesite (HMA)
 516 and high-alumina olivine tholeiite (HAOT) with high Mg#s are found in cinder cones and on Mount
 517 Shasta's flanks (Christiansen et al., 2013).

518 **Mineral Compositions:** Recent petrological work around Mount Shasta has largely focused on the
 519 HMA erupted at the S17 cinder cone near The Whaleback, ~ 20 km NNE of the main edifice. Interest in
 520 this cinder cone reflects a long-standing debate over whether HMAs are near primary mantle melts
 521 (Baker et al., 1994; Barr et al., 2007; Grove et al., 2002) or the result of magma mixing and crustal
 522 contamination (Streck and Leeman, 2018). Streck and Leeman (2018) display their EPMA data in an
 523 interactive tool overlain on a BSE image, allowing us to identify pairs of EPMA points on touching Opx-
 524 Cpx pairs. We assess all possible combinations of Cpx-Opx analyses for touching grains (e.g., for three
 525 EPMA spots on a Cpx, and two for a touching Opx, we obtain six pairs). This yields a total of $N=122$
 526 pairs. We also manually extract $N=328$ Cpx analyses where the location in the crystal could be classified
 527 (Core, Rim). Phillips and Till, (2022) measure Cpx and Opx compositions from the same HMA S17
 528 cinder cone, although from the data it is not possible to distinguish which analyses represent touching
 529 pairs. Given there is only one equilibrium test for Cpx-Opx (K_D , Fe-Mg) which shows limited success for
 530 hydrous experiments (Wieser et al., 2023c), we do not consider pairs when the textural context is
 531 unknown. Cpx-only pressures from these HMA are highly variable, ranging from 1–6 kbar (with very
 532 similar distributions and medians for J2022 and W2021). Cpx-Opx pressures are offset ~ 2 –3 kbar
 533 deeper, but certainly overlap with the distribution of Cpx-only pressures (particularly given the 3-4
 534 RMSE on each method, Wieser et al. 2023c).

535 Baker et al. (1994) perform mineral analyses on a series of basaltic andesite lavas associated with the
 536 Sargents Ridge and Misery Hill dome building episodes, located ~ 15 km to the N and NW of Shasta's
 537 summit clustered around Highway 97 (e.g., at $\sim 4000''$, summit at $\sim 14,000''$). They report $N=3$
 538 representative Cpx compositions. However, M. Baker (written coms) suggest that these analyses were
 539 low precision, with the WDS background only being collected once per thin section, so should not be
 540 used for barometry. Grove et al. (2005) measure mineral compositions in a wide variety of lavas
 541 representing the Hotlum, Shastina, Misery and Sargents eruptive phases from on/around the main
 542 Shasta edifice. However only representative mineral composition are reported (a total of $N=4$ Cpx, $N=2$
 543 Amp). Given the sparsity of available data, we do not perform any barometry on the main edifice, as
 544 these numbers are too small to sufficiently average out random analytical error (Wieser et al., 2023a).

545 **Melt inclusions:** Anderson (1974) perform EPMA analyses on olivine-hosted MIs from the S17 cinder
 546 cone, calculating H_2O by volatiles by difference. Sisson and Layne (1993) measure glass inclusions
 547 from Goosenest volcano and Copco Cone, ~ 35 km and ~ 60 km North of Shasta by SIMS. However,
 548 because of the lack of glass (and bubble) CO_2 measurements, as well as uncertainties associated with

549 volatile-by-difference methods (see Hughes et al., 2019), we do not calculate saturation pressures for
550 these inclusions.

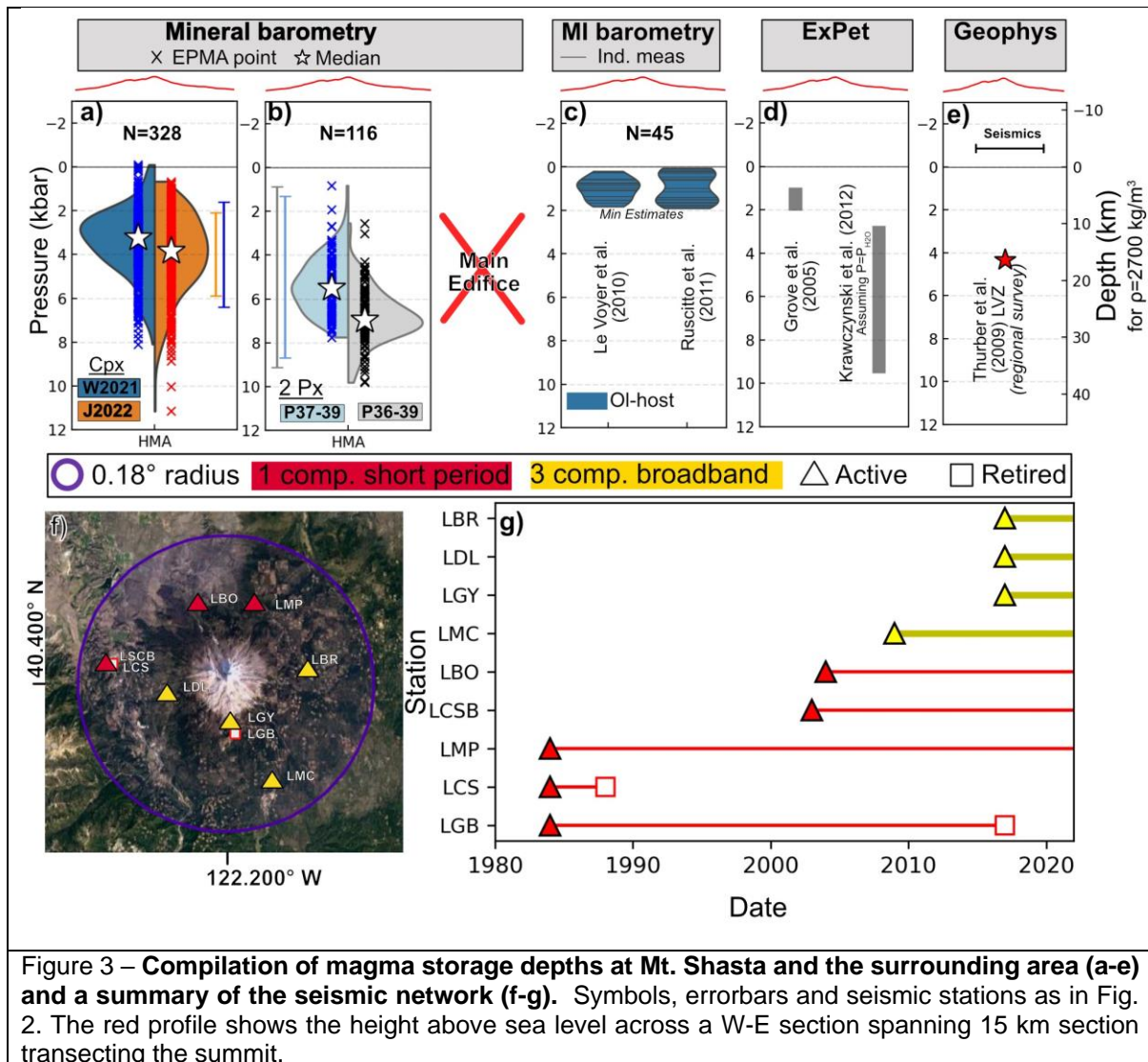
551 Le Voyer et al. (2010) perform SIMS measurements of reheated olivine-hosted MIs from H₂O-poor high
552 aluminium olivine tholeiites (HAOTs) and H₂O-rich basaltic andesites from mafic flank eruptions from
553 Mount Shasta. Their measured basaltic-andesite H₂O contents are lower than estimated by Baker et
554 al. (1994), which may reflect diffusive loss from the olivine (adding uncertainty to the saturation
555 pressure). We calculate saturation pressures for the N=25 MIs with major element and volatile data.

556 Ruscitto et al. (2011) perform FTIR measurements of naturally quenched primitive basaltic andesite
557 and high magnesian andesite olivine-hosted MIs from the S17 cinder cone. We calculate saturation
558 pressures for the N=20 MIs with major element and volatile data. Both datasets yield pressures
559 spanning ~0–2 kbar. However, all Shasta MI studies note the presence of abundant vapour bubbles,
560 many of which remain even after experimental homogenization (Le Voyer et al., 2010). Thus, it is very
561 likely that these calculated saturation pressures are very much minimum estimates for storage of mafic
562 magmas at Mount Shasta.

563 **Experimental phase equilibrium:** Grove et al. (2005) compare whole-rock and mineral compositions
564 from the main edifice of Mount Shasta to the experiments of Grove et al. (2003) to infer shallow crustal
565 differentiation of plagioclase (Plag) and pyroxene (Px) in a reservoir at 1–2 kbar (3–6 km, see also
566 Baker et al., 1994). In the schematic model presented in Grove et al. (2005, their Fig. 14), two additional
567 storage zones are depicted: 1) a reservoir fractionating Olivine (Ol)+Px at 7–10 km, and 2) a reservoir
568 fractionating Ol+Amp+Px at 15–25 km (based on high amphibole Mg#s and H₂O-rich MIs). Krawczynski
569 et al. (2012) perform additional experiments at 200, 500 and 800 MPa, and use these experiments to
570 calibrate a barometer estimating P_{H₂O} from the highest measured Amp Mg# in a given suite of samples.
571 By applying this equation to Shasta Amps, P_{H₂O} values of 2.8–9.5 kbar are obtained. However, these
572 pressures may be significant underestimates if CO₂ is present in the exsolved fluid at depth, such that
573 P_{tot} ≠ P_{H₂O}. Additionally, their Fig. 8 shows that the simple relationship between Amp Mg# and P is more
574 complex in mixed H₂O-CO₂ fluid experiments (and mafic melts beneath Shasta are likely in equilibrium
575 with a mixed fluid).

576 **Geophysics:** Thurber et al. (2009) present a regional 3D tomographic model of P wave velocity for all
577 of Northern California using a double-difference tomography algorithm (Zhang et al., 2004) with nodes
578 15–20 km apart. They image a low velocity zone (~5.5 km/s, 5% reduction) beneath Mount Shasta
579 centred at ~12 km depth (bsl). However, the 40–km horizontal extent of this body makes it impossible
580 to distinguish thermal vs. magmatic contributions to the local velocity low. The lack of high resolution,
581 local seismic inversions reflects the fact that no high density temporary deployments have ever been
582 deployed around Shasta to our knowledge (unlike iMUSH at Mount St. Helens). Additionally, Shasta
583 also shows relatively few earthquakes (Weaver et al., 1990), despite a long-lived short-period
584 monitoring network. This network has been recently upgraded with four three component broadband
585 seismometers (Fig. 3g). Meaningful inversions on this new network will be reliant on recording sufficient
586 earthquakes. From a geodetic perspective, there has been no detectable deformation at Mount Shasta
587 since at least the 1980s (Poland et al., 2017). To our knowledge, there are no other geophysical
588 constraints on magma storage beneath Shasta.

589 **Summary and Future work:** Despite the clear hazard potential of the main edifice of Mount Shasta
590 (ranked as the 5th most hazardous US volcano), we have remarkably few constraints on the magmatic
591 plumbing system under the main edifice. While the S17 high magnesian andesite cinder cone is
592 academically interesting from the perspective of the generation of arc magma compositions, this cone
593 has little relevance to future eruptions at Mount Shasta given the relative paucity of these high-
594 magnesian andesite compositions in this volcanic field and its age pre-dating construction of the modern
595 edifice (see Phillips and Till, 2022). We suggest that further work targeting MIs, mineral compositions
596 and phase equilibration experiments in the presence of mixed fluids from the main edifice is needed.
597 From a geophysical perspective, a high-density temporary deployment of seismometers using active
598 sources would help, although permitting would be non-trivial. Soon, we expect sufficient earthquakes
599 to be collected on the upgraded seismic network for a first-order seismicity assessment.



600

601 **Medicine Lake**

602 Medicine Lake Volcano is located ~50 km E-NE of Mount Shasta and the main Cascade front, on the
 603 western edge of the Basin and Range extensional province (Donnelly-Nolan et al., 2008). It has a broad
 604 shield shape, and is the most voluminous volcano in the Cascades. It has erupted a wide variety of
 605 magma compositions, ranging from hydrous calc-alkaline magmas (basalt to rhyolite), to relatively
 606 anhydrous, high-aluminium olivine tholeiites. In general, basalts and andesites form the flank of the
 607 volcano, with rhyolites and small volumes of dacites occurring at the summit (Donnelly-Nolan, 2008).

608 **Mineral Compositions:** Despite a number of detailed petrological studies, there is a notable paucity of
 609 published mineral data, with most papers only publishing representative analyses:

- 610 • Gerlach and Grove (1982) report N=8 Cpx from a variety of units (Modoc basaltic-andesite,
 611 older and later platy olivine andesite, Medicine Lake Dacite, Glass Mountain Rhyolite).
- 612 • Grove and Donnelly-Nolan (1986) report N=4 Cpx and N=3 Amp from three types of magmatic
 613 inclusions from Pleistocene-Holocene silicic flows.
- 614 • Grove et al. (1997) present data from N=1 Cpx and N=3 Amp from Glass Mountain
- 615 • Grove et al. (1988) report N=4 Cpx analyses from the Burnt Lava flow
- 616 • Kinzler (1985) and Kinzler et al. (2000) report the composition of a N=5 and N=1 Cpx from the
 617 Callahan lavas respectively.

618 We obtain $N=21$ Cpx and $N=6$ Amp after filtering for quality. Cpx return a median pressure of 0.8 kbar
619 using W2021, and 1.7 kbar using J2022, and Amp return a median pressure of ~ 2.5 kbar.

620 **Melt Inclusions:** Sisson and Layne (1993) measure a H_2O content of ~ 0.2 wt% from Black Crater MIs
621 using SIMS. Kinzler et al. (2000) report an Amp-bearing MI within an Mg-rich olivine with ~ 3 wt% H_2O .
622 No CO_2 data exists for either the melt phase or the bubble in these studies. Thus, we do not calculate
623 saturation pressures for these inclusions. MI work analysing the melt and vapour phase for H_2O and
624 CO_2 in the Paint Pot basaltic deposit is currently in progress (see Couperthwaite et al., 2022). To our
625 knowledge, there has been no melt inclusion work performed on the more silicic compositions at
626 Medicine Lake. This may reflect the paucity of rapidly-quenched tephra at this volcano dominated by
627 lava flows; only two ash falls are documented from the Holocene (Heiken, 1978).

628 **Experimental phase equilibrium:** Grove et al. (1982) conducted experiments investigating the origin
629 of the calc-alkaline series at Medicine Lake. However, other than demonstrating that $P_{\text{H}_2\text{O}}$ must be
630 greater than 1 kbar to generate calc-alkaline compositions, no further constraints are placed on magma
631 storage depths. Wagner et al. (1995) performed experiments on the Late Pleistocene Lake Basalt,
632 reproducing lava compositions and phenocrysts in 1 kbar H_2O -saturated experiments. However, they
633 do not perform experiments at different pressures, so the same relationships may be have reproduced
634 at other pressures (e.g. 0.5, 2 kbar). Grove et al. (1997) perform experiments at 1, 1.5, and 2 kbar to
635 investigate the origin of the Rhyolite of Glass Mountain. They suggest that the presence of Amp in more
636 mafic inclusions indicates crystallization at >2 kbar, while Ol-Plag and Ol-Plag-Cpx inclusions indicate
637 crystallization at near H_2O -saturated conditions at ≤ 1 kbar. Finally, Bartels et al. (1991) perform
638 experiments at 1 atm, 10 and 15 kbar on high-aluminium basalts from Medicine Lake, demonstrating
639 that these liquid compositions are close to equilibrium with a mantle lherzolite source. However, the
640 high-pressure nature of these experiments mean they do not provide insights into the depth at which
641 magma is stored in the crust beneath Medicine Lake.

642 **Geophysics:** Evans and Zucca (1988) and Chiarabba et al. (1995) use active source seismic
643 topography (the NeHT experiment of 1985) and seismic refraction studies conducted in 1982 and 1984
644 to image P-wave velocity and attenuation beneath Medicine Lake. Evans and Zucca (1988) obtain ~ 1 –
645 2 km depth resolution in the upper 5–7 km of the crust, and image a low Q (high attenuation), low
646 velocity region in their layer 3 beneath the east central caldera with a volume of a few 10^3 of km^3 (1.2–
647 3.25 km depth bsl, 3.6–5.6 km below ground level). Chiarabba et al. (1995) experiment with alternative
648 inversion strategies and find that the low-velocity body is well resolved at 3–5 km depth (bgl), although
649 some less-stable inversion strategies suggest that the low velocity zone is deeper (>6.8 km). Overall,
650 Chiarabba et al. (1995) conclude that the low velocity zone likely occurs at 3–4 km depth (bgl), but could
651 exist as deep as 7 km depth. The small size of the low velocity anomaly identified in these two seismic
652 studies, roughly 10 km wide horizontally, can account for the fact it is not seen in teleseismic studies
653 (e.g., Ritter and Evans, 1997).

654 Pitt et al. (2002) report 1 LP EQ beneath Medicine Lake in Dec 1989 (15 km bsl). The notable paucity
655 of seismometers (particularly three component broadband) means that there have not been any more
656 recent investigations of magma storage using passive source techniques since the flurry of geothermal
657 exploration in the 1980s (Fig. 4g).

658 Interpreting geodetic data is complicated by the fact that Medicine Lake impinges on the western edge
659 of the Basin and Range, meaning it is subject to regional extension. Additionally, Medicine Lake's large
660 volume, and therefore mass, means that it loads and deforms the surrounding crust. These
661 "background" signals make it difficult to distinguish the smaller signals resulting from inflation and
662 deflation of crustal magma chambers (Dzurisin et al., 1991; Poland et al., 2006). Dzurisin et al. (1991)
663 and Dzurisin et al. (2002) examined levelling surveys from 1954–1989, a small summit survey from
664 1988, and seismicity occurring 1978, 1981, and 1988. They infer that regional/loading signals
665 overwhelm the minor amount of signal which may arise from crystallization and magma withdrawal.

666 Poland et al. (2006) investigated campaign GPS data and InSAR data from Medicine Lake Volcano.
667 InSAR identifies ~ 10 mm/yr of approximately radially symmetric subsidence centred on the caldera
668 region (consistent with GPS and levelling data). They show that the GPS horizontal displacements are
669 inconsistent with the model of Dzurisin et al. (2002) of volume being lost at 10–11 km depth, because

670 this should produce radially-inward horizontal deformation up to 40 km radius. Instead, they invert for a
 671 Mogi point source at shallower depths (~6 km) to explain the fact only GPS stations within ~10 km of
 672 the summit show inward deformation. This deformation source can also be fitted as a deflating sill at 5
 673 km depth. However, this sill fit has a higher misfit, and doesn't effectively recreate the vertical
 674 deformation of the 1954–1989 levelling survey of Dzurisin et al. (1991). Overall, Poland et al. (2006)
 675 suggested the dominant signal is edifice loading and extension of a hot weak crust, rather than magma
 676 withdrawal. Similarly, Parker et al. (2014) examined additional InSAR data (up to 2011), suggesting that
 677 deformation is caused by tectonic extension and gravitational loading, with a possible role for cooling
 678 and crystallization of an intrusive body at depth (rather than an active magma chamber). Given that
 679 geodetic signals appear not to represent magmatic processes at Medicine lake, we do not include them
 680 on Fig. 4.

681 **Other:** Another possible constraint on magma storage depth comes from geothermal exploration
 682 drilling, which encountered hydrothermally-altered granitoid rocks at 2–2.9 km depth below the summit
 683 caldera (Zircon dates of ~332 ka, Donnelly-Nolan et al., 2008; Lowenstern, 2003). While down dropping
 684 of the caldera and erosion over 100s of kyrs can alter the current depth vs the emplacement depth,
 685 down dropping is thought to have been limited to ~240–440 m, and erosion is relatively negligible in the
 686 high desert (Donnelly-Nolan et al., 2008, Donnelly-Nolan written communications).

687 **Summary and future directions:** We suggest that the most precise constraints on magma storage
 688 beneath Medicine Lake could be obtained by performing detailed MI studies on rapidly quenched
 689 material where available. For slower-cooled lava flows, detailed analysis of minerals and any fresh
 690 glasses could help provide barometric constraints to supplement the small amounts of publicly-available
 691 mineral data. Without densification of the seismic network with three component broadband
 692 seismometers, or targeted local studies, additional geophysical constraints are unlikely to be obtained
 693 in the near future.

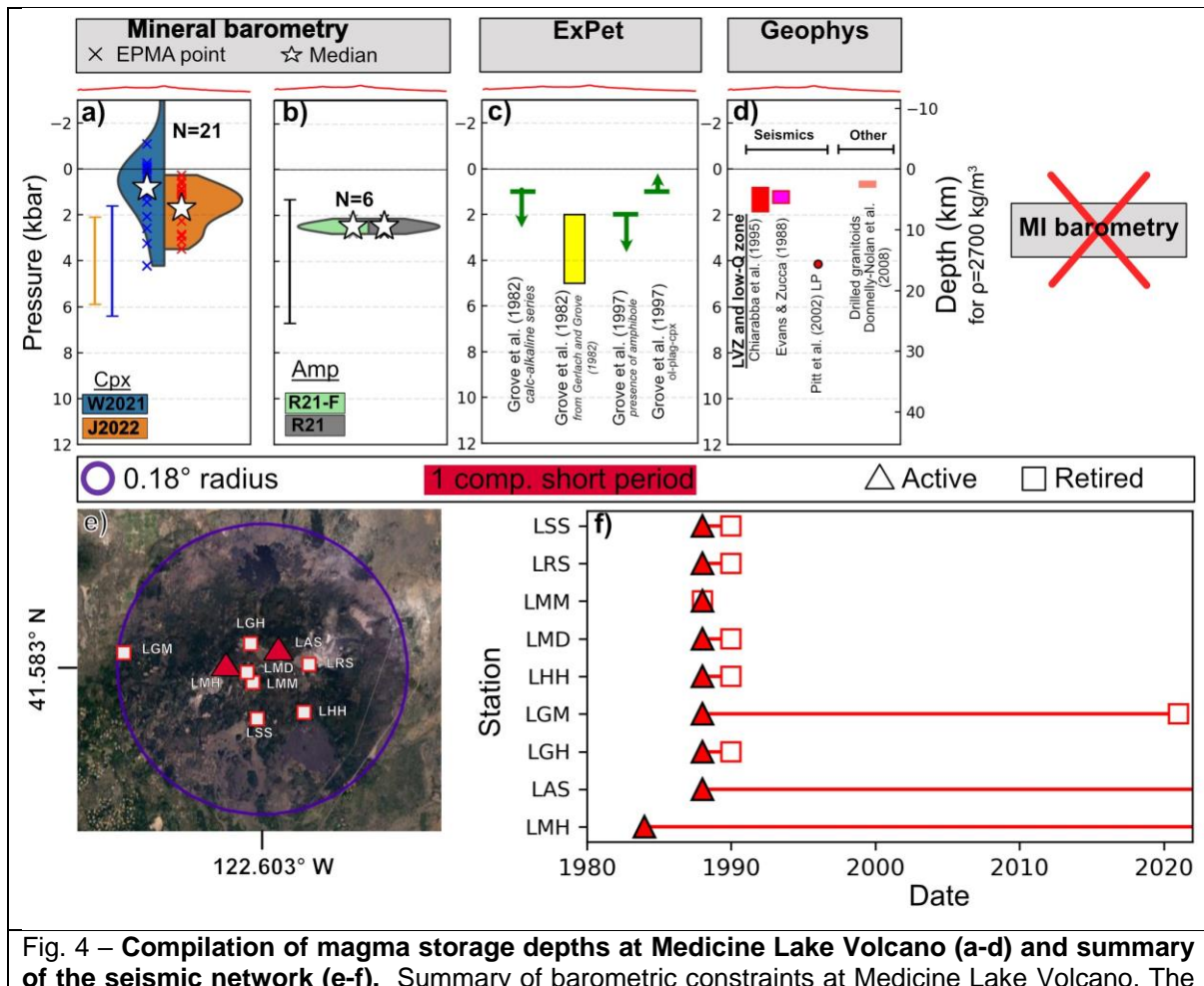


Fig. 4 – Compilation of magma storage depths at Medicine Lake Volcano (a-d) and summary of the seismic network (e-f). Summary of barometric constraints at Medicine Lake Volcano. The

red profile shows the height above sea level across an N-S section spanning 30 km transecting the summit

694

695 **Crater Lake/ Mount Mazama**

696 The climatic eruption of Mount Mazama at ~7.7 ka produced the modern-day caldera known as Crater
 697 Lake. Activity at Mount Mazama began around ~420 ka, producing basaltic andesite, medium-K
 698 andesites and dacites. The first preclimactic rhyodacites erupted at ~27 ka, and the evolution of this
 699 silicic reservoir was terminated by the massive climatic eruption of ~50 km³ at 7.7 ka (Bacon and
 700 Lanphere, 2006). Post-caldera volcanism was dominated by andesite for 200–500 yrs after the climatic
 701 event, followed by an eruption of a rhyodacite at 4.8 kyrs. There are also 20 cinder cones within Crater
 702 Lake National Park (Prueher and McBirney, 1988).

703 **Mineral Compositions:** We compile the following mineral data:

- 704 • N=16 Cpx from preclimactic rhyodacites from Nakada et al. (1994)
- 705 • N=126 Cpx analyses from the 8 dacitic-rhyodacitic deposits spanning 71–7.7 ka described in
 706 Wright et al. (2012, kindly provided by the authors).
- 707 • N=194 Cpx and N=245 Amp from the original handwritten datasheets of EPMA analyses for
 708 the climatic samples described in Druitt and Bacon (1989).

709 The dacitic-rhyodacitic deposits at Crater Lake are outside the calibration range of the W2021
 710 barometer, which could explain why calculated pressures are so shallow (median=-0.2 kbar). The
 711 median pressure for the J2022 barometer is ~1.2 kbar, with a skewed distribution to higher pressures
 712 (this barometer does not return very shallow pressures). Si-Al filtered Amp pressures are very similar
 713 to those unfiltered, with median pressures of ~ 3 kbar. There is also a small cluster of Amp-only
 714 pressures at ~7 kbar, from samples 80c444 (Ol-Px rich scoria from top of the climatic ignimbrite),
 715 82C882 (high-Sr scoria from top of climatic ignimbrite), 82C938 (high-Sr enclave from Liao rock) and
 716 1290 (low-Sr scoria from the top of the climatic ignimbrite), all from Druitt and Bacon (1989). It is difficult
 717 to interpret the single Cpx measurement from Wright et al. (2012) yielding a pressures in a similar range
 718 to these high Mg# amphiboles without detailed information on the analytical uncertainty associated with
 719 these measurements (see Wieser et al. 2023a). Additional mineral analyses will be vital to pin down the
 720 possibility of a deeper region of more mafic magma storage.

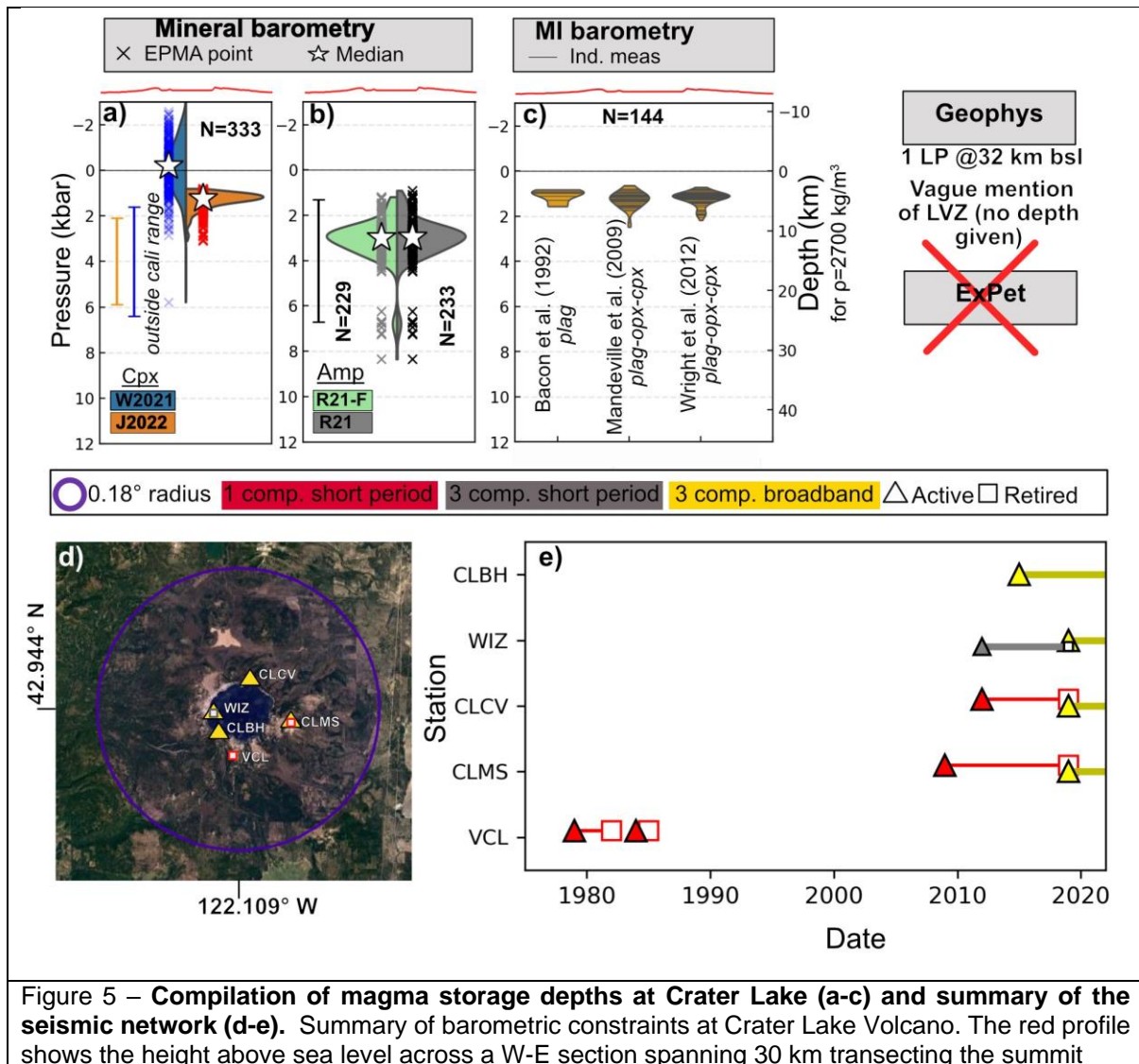
721 **Melt Inclusions:** Bacon et al. (1992) analyse plagioclase-hosted MIs from three rhyodacitic Holocene
 722 eruptions (~7kyrs-6.8 yrs BP) from Crater Lake by FTIR (Liao Rock, Cleetwood, and the climatic event).
 723 CO₂ concentrations in these MIs are <25 ppm, and often undetectable by FTIR. We remove MIs with
 724 low H₂O contents (<3.1 wt%) which the authors suggest may have a connection to the outside, leaving
 725 N=10 MIs. Mandeville et al. (2009) analyse plagioclase and pyroxene-hosted MIs from the same three
 726 eruptive episodes as Bacon et al. (1992), also using FTIR. None of the reported N=48 MIs have visible
 727 connections to the outside or cracks, and CO₂ concentrations are below the FTIR detection limit. Wright
 728 et al. (2012) analyse N=127 plagioclase and pyroxene-hosted MIs from 8 dacitic-rhyodacitic deposits
 729 spanning 71–7.7 ka using SIMS (along with a subset by FTIR). They identify high H₂O (3–4.6 wt%) and
 730 low H₂O (<2.4 wt%) populations of MIs. They suggest that the low-H₂O population likely reflects
 731 leakage, and diffusive re-equilibration. Thus, for consistency with Bacon et al. (1992), we do not
 732 calculate saturation pressures for inclusions with <3.1 wt% H₂O. Wright et al. (2012) only detect CO₂
 733 significantly above detection limit in deposits from the 71 ka Pumice Castle. All Crater Lake MI
 734 saturation pressures cluster at ~1 kbar depth. To our knowledge, no vapour bubbles have been
 735 measured in these more silicic MIs, although this doesn't mean they are CO₂-free.

736 **Experimental Petrology:** We are not aware of any published experimental petrology studies placing
 737 constraints on magma storage depths beneath Crater Lake.

738 **Geophysics:** The only seismic constraints at Crater Lake that we are aware of is a single LP at ~32
 739 km depth (Nichols et al., 2011), and a brief mention of a low velocity zone in the lower crust below
 740 Crater Lake in the regional teleseismic study by Harris et al. (1991). However, Harris et al. (1991) do
 741 not provide a depth or place any quantitative constraints on the size of this body, so we do not include
 742 this in our compilation. The lack of seismic constraints on magma storage is not surprising; the seismic
 743 network at Crater Lake was non-existent for more than 20 years in the late 1980s to mid 2000s (Fig.

744 5g), and has only been upgraded very recently with three component broadband seismometers. Once
 745 sufficient earthquakes have been measured on this new network, additional constraints on magma
 746 storage may be possible. Poland et al. (2017) summarize available geodetic constraints at Crater Lake,
 747 which show no deformation resolvable above survey noise since the 1980s.

748 **Summary and Future work:** We suggest that further petrological and experimental work examining
 749 the postclimactic materials erupted at Wizard Island could provide useful insights into the likely storage
 750 depths of the next eruption at Crater Lake. Examination of CO₂ within more silicic MI vapour bubbles
 751 would also be a worthy target, as would melt inclusion measurements on the numerous mafic cinder
 752 cones, which have been suggested to tap magma bypassing the central silicic reservoir (Prueher and
 753 McBirney, 1988). Although permitting would certainly be a challenge, a higher resolution array with
 754 active sources could help provide additional geophysical constraints.



755 **Three Sisters**

756 The Three Sisters volcanic field consists of three prominent summits (North, Middle and South Sister),
 757 as well as a number of distributed vents. North Sister has a very monotonous basaltic-andesite
 758 composition, with activity between ~120–50 ka, including a small shield (Little Brother), and a string of
 759 fissures (Matthieu Lakes fissure, Fierstein et al., 2011; Schmidt and Grunder, 2011). Activity at Middle
 760 and South Sister has been largely contemporaneous, with Middle Sister erupting basalt-andesite and
 761 dacite, while South Sister erupts only intermediate to more felsic compositions. In general, relatively
 762 little petrological work has been done on this area.

763 **Mineral Compositions:** We were only able to compile N=6 Cpx from the Matthieu Lakes Fissure
764 transecting North Sister from Schmidt and Grunder (2011), and N=11 Cpx from South Sister dacites
765 from Waters et al. (2021). The small number of analyses make it harder to average out the effects of
766 analytical uncertainty; the available data suggests storage centred around 1 kbar at North Sister and
767 ~2 kbar at South Sister, although these differences are certainly within uncertainty of one another, and
768 individual analyses show substantial overlap between the two centers.

769 **Melt Inclusions:** To our knowledge, there are no published MI analyses from South or Middle Sister.
770 Mordensky and Wallace, (2018) analyse olivine-hosted MIs from North Sister using FTIR. 9/15 of these
771 MIs had vapour bubbles. They find that minimal PEC has occurred (0–2.3%, representing $\Delta T \sim 20^\circ\text{C}$).
772 They perform a bubble correction similar to that of Aster et al. (2016), and infer ~48–78% of CO_2 is
773 within the bubble. However, for such small amounts of PEC, where the vast majority of the bubble grows
774 during syn-eruptive cooling, bubble reconstructions assuming re-equilibration between vapour bubble
775 and melt can greatly overestimate bubble CO_2 contents (Wieser et al., 2021). Additionally, with such
776 low amounts of PEC, the correction is heavily affected by the choice of FeO_t content, which shows
777 scatter in local whole-rock compositions. Mordensky and Wallace (2018) report PEC-corrected major
778 element data for N=8 North Sister MIs, six of which have CO_2 below-detection limit. Given the small
779 number of analyses, low CO_2 contents in the glass, lack of published major element contents for many
780 MIs, and lack of bubble CO_2 data, we do not perform saturation pressure calculations. Mercer and
781 Johnston (2008) cite unpublished MI data from North Sister, which we were not able to obtain for this
782 study.

783 **Experimental Petrology:** Mercer and Johnston (2008) perform experiments using a North Sister melt
784 composition, mostly to constrain the lower crustal mineralogy the melt last equilibrated with. They
785 propose based on phase relationships and the absence of garnet or amphibole signatures that mantle-
786 derived melts likely stall at ~12 kbar in a deep crustal hot zone, and then ascent to ~1 km where
787 observed phases such as Ol, Plag and Cpx crystallize. We do not include these depths in our
788 compilation, as they are not precise constraints on magma storage locations, but instead constrain the
789 likely ascent path based more on inference of crustal structure than precise experimental constraints
790 on phase stability. While their experiments focus on Newberry Volcano, Mandler et al. (2014) draw
791 comparisons with natural compositions erupted at the Three Sisters, indicating ‘damp’ not wet magmas
792 are present at Three Sisters along the arc front, as well as in the rear-arc.

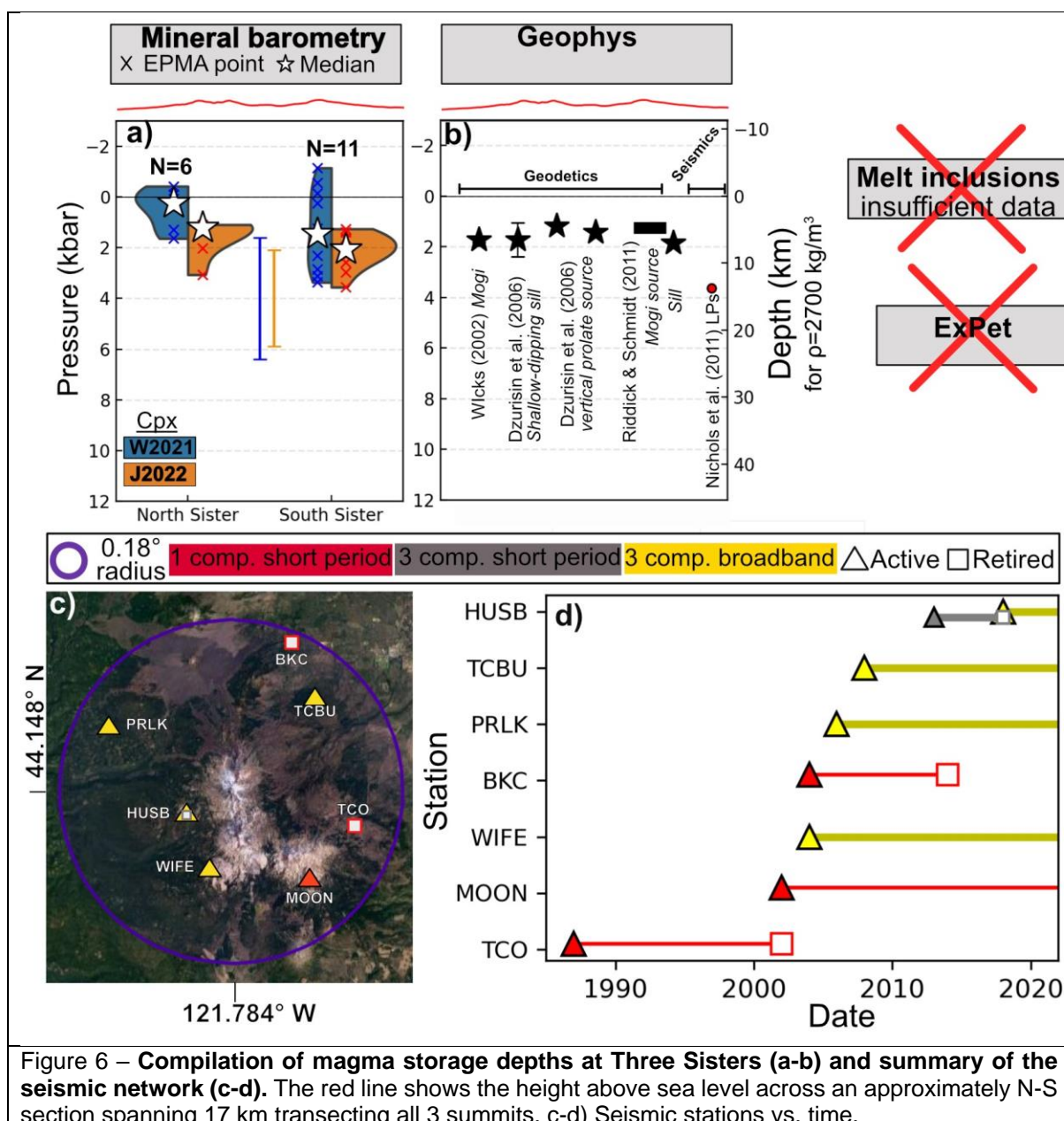
793 **Geophysics:** We are not aware of any seismic constraints on magma storage at Three Sisters, and
794 the PNSN only locates 0–3 earthquakes within 10 km per year. Seismic constraints are not helped by
795 the fact that there are relatively few seismometers within a very broad area, and these were only
796 upgraded to broadband seismometers relatively recently (Fig. 6g).

797 The lightly vegetated flanks around Three Sisters makes it an attractive location for satellite-based
798 geodetics (Poland et al., 2017). InSAR acquisitions between 1992–2000 reveal inflation over a broad
799 area (10 x 20 km) centred ~6 km west of the South Sister summit (Wicks, 2002). InSAR was vital to
800 identify this period of deformation, as it was offset to the west of the electro-optical distance meter
801 (EDM) and tilt-levelling methods installed at the summit between 1985–1986. Wicks (2002) model this
802 inflation with a Mogi point source at 6.5 ± 0.4 km depth (rlu), with a volume increase of 0.0023 ± 0.003
803 km^3 . Dzurisin et al. (2006) supplement InSAR observations with tilt surveys from 1985, 1986 and 2001,
804 EDM surveys from 1985–1986, Campaign GPS surveys from 2001–2002, and levelling in 2002–2003
805 along survey lines intersecting the deformation centre. They invert these four datasets, investigating
806 Mogi point sources, elliptical and dislocation sources, finding that the best fit is a shallowly-dipping sill
807 at 6.5 ± 2.5 km depth bgl. Dzurisin et al. (2009) further supplement this data with InSAR, GPS, and
808 levelling data collected up to 2006. This new data reveals that the inflation rate has been decreasing
809 exponentially. They suggest that the best fit shallowly-dipping sill proposed by Dzurisin et al. (2006)
810 results from combining early InSAR data with later GPS data during this change in deformation, skewing
811 the relative proportions of horizontal motion (which GPS is most sensitive to) and vertical deformation
812 (which InSAR is most sensitive to). Dzurisin et al. (2009) instead propose a vertical prolate source
813 geometry, which provide better fits to the data once these temporal changes are accounted for. This
814 source sits at 4.4 km depth bgl with an aspect ratio of 0.9, which is the best fit if network translation is
815 ignored (the source is 5.4 km bgl with an aspect ratio of 0.86 when accounting for network translation).

816 Riddick and Schmidt (2011) examine C-band InSAR from two satellites (ERS and ENVISAT),
817 suggesting that deformation tails off following two separate linear trends (1998–2003, 2004–2010).
818 Using a Mogi source, they obtain 5.5 km, 6.5 km using an ellipsoidal source, and 7 km using a sill
819 source.

820 Wicks (2002) suggest that the deformation source could result from the injection of new magma, or
821 pressurization of a hydrothermal system, with the former being more likely as hydrothermal activity is
822 often accompanied with seismic activity (and this episode was relatively aseismic). Dzurisin et al. (2009)
823 also conclude based on spring chemistry that an intrusion of magma is a more likely cause of
824 deformation than a hydrothermal system perturbation.

825 **Summary and Future work:** Given recent renewed uplift ~5 km W of South Sister (Jan 2022) in
826 addition to the deformation discussed above, more detailed petrological work on this edifice is
827 warranted. In particular, MI constraints could help determine whether the depth inferred from geodetics
828 is similar to that of magma reservoirs feeding past eruptive episodes. Unlike many Cascade volcanoes,
829 South Sister has silicic tephra fall deposits suitable for such work (and, in fact local ash dispersion is
830 one of the most probable future hazards in this area, Hildreth et al., 2012). In order to investigate the
831 storage depths of the more mafic fissures and cinder cones of North Sister and the surrounding area,
832 a detailed study of vapour bubble CO₂ in MIs is required. Experimental constraints could be used to
833 investigate the relationship between mafic and silicic magmas, combined with new, high precision
834 analyses of mineral compositions, to build a more coherent model of the magmatic plumbing system.



835

836 **Newberry Volcano**

837 Newberry Volcano lies ~50–60 km east of the main arc front and covers the largest area of all Cascade
 838 volcanoes. It is second in volume only to Medicine Lake. Newberry exhibits predominantly bimodal
 839 volcanism; intracaldera eruptions are rhyolitic, while its north-westerly trending rift zone hosts basaltic-
 840 andesite fissures and cinder cones. Newberry caldera was formed at ~75 ka with the eruption of a
 841 compositionally-zoned basaltic-andesite to rhyolite tuff (Donnelly-Nolan et al., 2011).

842 **Mineral Compositions/Melt inclusions:** We were unable to find any published mineral compositions
 843 or MIs from Newberry Volcano.

844 **Experimental Petrology:** Mandler et al. (2014) perform 1 bar (anhydrous) and H₂O-saturated 1–2 kbar
 845 experiments on the ~75 ka caldera-forming tuff from Newberry Volcano. They find that the 1 kbar
 846 experiments best reproduce the samples from the caldera-forming tuff, but that these experiments were
 847 conducted with too high H₂O contents, because differentiation was likely H₂O-undersaturated. They
 848 state that it is difficult to constrain the pressure of storage in these undersaturated systems, where the
 849 effect of pressure on phase equilibria is small at crustal conditions. Overall, they conclude that
 850 differentiation occurred in the upper crust.

851 **Geophysics:** Extensive geophysical work has been performed at Newberry because of its geothermal
852 potential. The teleseismic study of Stauber et al. (1988) indicated that no magma chamber is resolvable
853 within the resolution of their study (e.g., ~5 km width). Using active source tomography with higher
854 resolution, Achauer et al. (1988) identify a low velocity body at 3–5 km depth bgl, which they interpret
855 to be a small silicic or stratified magma body, although the lower end of this body is difficult to resolve
856 in their inversion. Zucca and Evans (1992) investigate P-wave attenuation using the same seismic data
857 as Achauer et al. (1988). They find that the low velocity zone in their layer 3 has average attenuation,
858 such that it may reflect a recently solidified, hot cracked pluton, rather than actual melt (which would
859 have high attenuation). More recently, Beachly et al. (2012) use travel time tomography and forward
860 modelling of arrival times and seismic amplitudes from an active-source seismic experiment with 75
861 three component seismometers in 2008. They identify a central low velocity anomaly at 3–6 km below
862 the caldera floor. They find the best fit is a molten sill with a thin mush region at the bottom - in their
863 schematic the melt body is located at ~4–5 km depth beneath the caldera.

864 The seismic network at Newberry was densified with six new three component broadbands in 2011 and
865 two further upgrades to 3 component short period stations in 2019, increasing the opportunity for
866 passive source techniques when supplemented by data from the active source campaigns. Heath et al.
867 (2015) combine active and passive source seismic data collected on the 2008 array to better constrain
868 seismic velocity, with increased resolution at depths >6 km (the limit of the Beachly et al. 2012 study).
869 They identify the main low velocity volume at 3–5 km depth below the crater floor, with horizontal
870 dimensions of 5 x 3 km, and a vertical thickness of 2 km. They suggest that the location of this body is
871 consistent with it hosting the rhyolitic magmas erupted in the caldera. Their model requires ~10% melt
872 with a minimum melt volume of 2.5 km³ in this region. They also report LPs from PNSN seismometers
873 between 2012 and 2015 at 7–11 km depth (rlu). Finally, Heath et al. (2018) use seismic autocorrelation,
874 and find a coherent P-wave reflection at 2.5 km depth beneath the caldera, which they infer is generated
875 at the top of the magma body.

876 Bowles-Martinez and Schultz (2020) use 3D magnetotellurics to identify a relatively resistive magma
877 chamber beneath Newberry Volcano at 3–4 km depth below the crater floor. The relatively high
878 resistivity of this body does not require melt and could be a fractured pluton. However, for consistency
879 with the seismic studies described above, they show that this body could be melt, if that melt was
880 relatively water-poor (~1.5 wt%). They indicate that such a low H₂O content is reasonable if the rhyolitic
881 melt differentiated from a dryer basalt. However, mafic inclusions in the Big Obsidian Flow have a phase
882 assemblage typical of relatively hydrous magmas (e.g. amphibole, two pyroxene and Fe-Ti oxides,
883 Linneman and Myers, 1990). Additionally, melt inclusions indicate that differentiation of a basalt with
884 ~0.3-0.6 wt% H₂O to a dacite at Kilauea Volcano raises H₂O contents to 2 wt% (Wieser et al., 2022c).
885 Thus, it seems unlikely that fractional crystallization at ~3–5 km depth could produce such a dry rhyolite
886 magma without a substantial contribution from melting of very anhydrous crustal material.

887 Dzurisin (1999) examine levelling data over a period of uplift between 1931–1994. They suggest that
888 one possible mechanism for this uplift is the intrusion of 0.06 km³ of magma ~10 km below the crater
889 floor. It is hard to investigate this deformation source further, because no measurable volcanic
890 deformation has occurred at Newberry since the 1980s (Poland et al. 2017).

891 **Summary and Future work:** Overall, Newberry Volcano has been subjective to extensive geophysical
892 investigation. However, it is clear that substantially more petrological work involving mineral and MI
893 compositions is required. In particular, MI work constraining pre-eruptive H₂O contents will help inform
894 geophysical inversions (e.g., determining whether rhyolitic melts are as dry as suggested by Bowles-
895 Martinez and Schultz, 2020). Additional experiments conducted using volatile contents inferred from
896 melt inclusions could help constrain storage conditions further (Mandler et al., 2014).

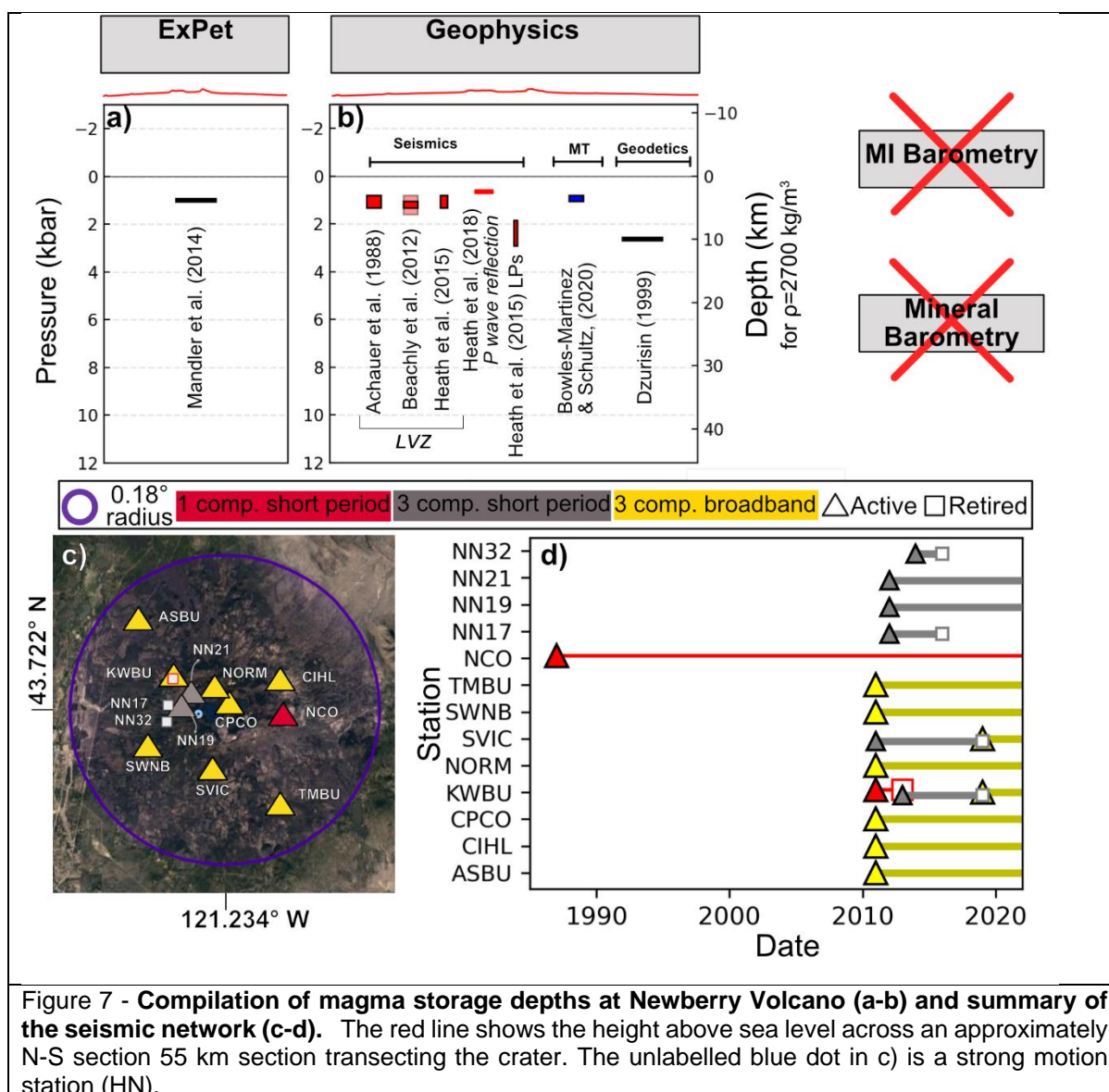


Figure 7 - Compilation of magma storage depths at Newberry Volcano (a-b) and summary of the seismic network (c-d). The red line shows the height above sea level across an approximately N-S section 55 km section transecting the crater. The unlabelled blue dot in c) is a strong motion station (HN).

897

898 Mount Jefferson

899 The area around Mount Jefferson has a complex volcanic history over 4–8 Myrs, with 160 separate
 900 units from monogenetic and composite cones, shields, and domes spread over 150 km² (Conrey, 1991).
 901 A transition from widespread mafic volcanism to more focused intermediate and silicic volcanism and
 902 the development of the modern edifice began at ~300 ka (Conrey, 1991, DiGuilio, 2015). Erupted rocks
 903 are characterized by very complex, heterogenous crystal cargoes (Conrey, 1991, Ustunisik et al., 2016).

904 **Mineral Compositions:** We obtain the following mineral analyses:

- 905 • N=87 Amp analyses from Conrey (1991) representing the last 200 kyrs of stratigraphy at Mt.
 906 Jefferson, from rhyodacites, dacites, and quenched mafic inclusions. While Conrey (1991) also
 907 present Cpx analyses, they do not report Na₂O data, so these measurements cannot be used
 908 with the J2022 and W2021 barometers.
- 909 • N=211 Amp, N=24 Cpx and N=25 Opx-Cpx pairs from various intermediate units from DiGuilio
 910 (2015). This units include the Whitewater Creek intermediate domes (32 ka), the Park Butte
 911 Andesite (154 ka), and the Pleistocene age basaltic andesite of Whiskey Creek. Only N=3 of
 912 these Opx-Cpx pairs are in high-T K_D equilibrium following Putirka (2008).
- 913 • N=32 Amp analyses from the ~10 ka Whitewater Creek andesite reported by Ustunisik et al.
 914 (2016).

915 The median Cpx-only pressure is ~2.5 kbar using W2021 and ~1.9 kbar using J2022. Amp-only median
 916 pressures (~3 kbar) are reasonably similar to these Cpx pressures. In contrast, median Cpx-Opx
 917 pressures are 6.7 kbar using Eq37–39 and 5.7 kbar using Eq36–39 from Putirka (2008). Given the
 918 relatively poor performance of Cpx-Opx barometers in arc magmas (Wieser et al., 2023c) and the
 919 relatively small number of Opx-Cpx analyses, we suggest that more substantial evidence is needed to
 920 infer a deeper magma storage zone.

921 **Melt Inclusions:** The only MI measurements from Mount Jefferson to our knowledge are from Ustunisk
 922 et al. (2016). However, they do not measure MI H₂O or CO₂, so no barometric constraints can be
 923 obtained from these samples.

924 **Experimental Petrology:** To our knowledge, there are no experimental constraints on magma storage
 925 at Mount Jefferson.

926 **Geophysics:** We are not aware of literature describing seismic or magnetotelluric investigations of
 927 magma storage. Given there is only a single one component short-period seismometer >10 km from
 928 the summit, and that the PNSN locates an average of 0 earthquakes per decade, the absence of seismic
 929 constraints on magma storage is unsurprising. No-ground based geodetic studies have been performed
 930 at Mount Jefferson. InSAR from the 1990s-2000s shows coherence, but no deformation (Poland et al.,
 931 2017).

932 **Summary and Future work:** Further petrological work would help to further investigate the plumbing
 933 system, particularly MI or experimental petrology. However, the low threat ranking of Jefferson, this
 934 work is perhaps not as urgent as similar data gaps at higher threat volcanoes (Fig. 1, Fig. 16).

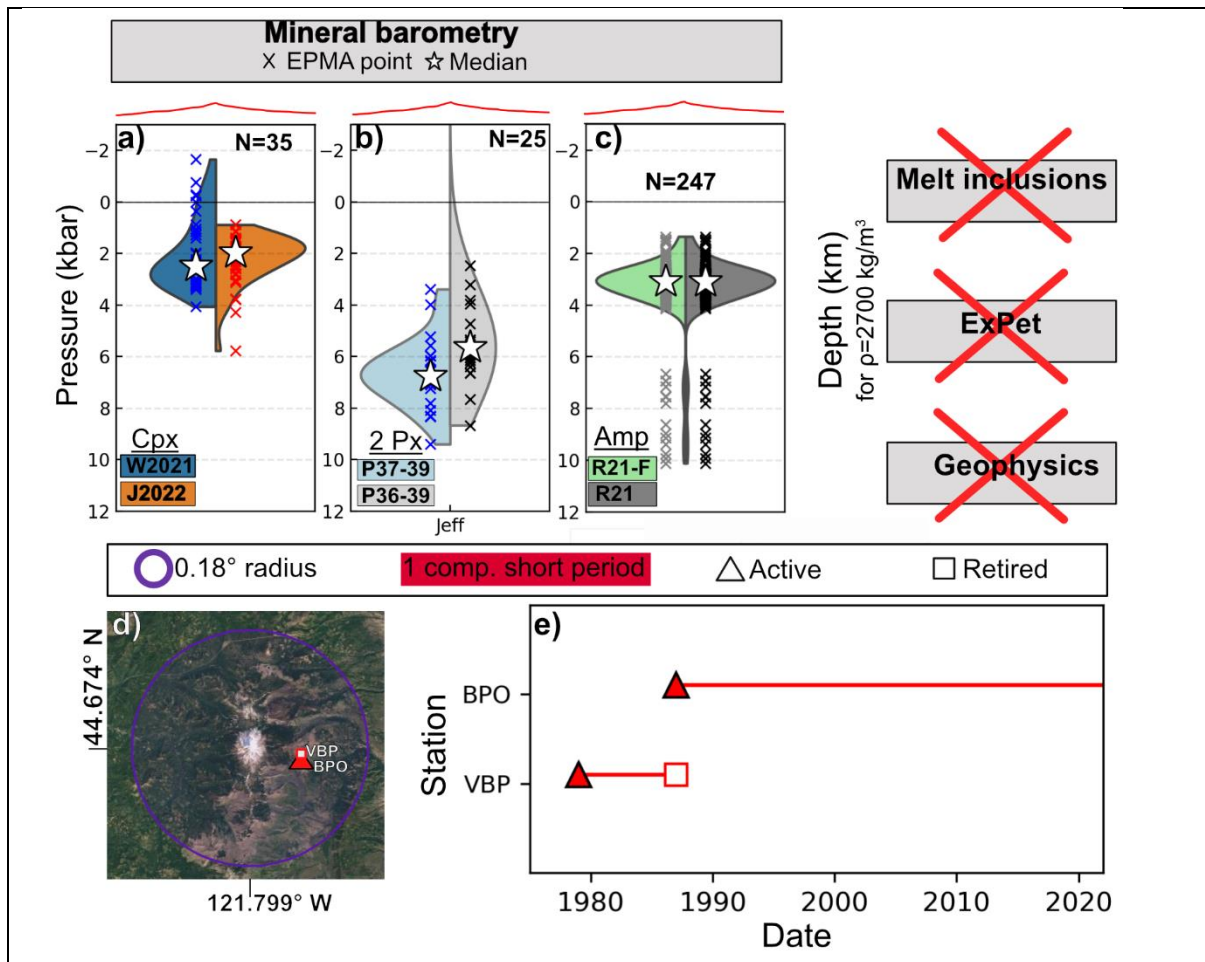


Figure 8 – **Compilation of magma storage depths at Mount Jefferson (a-c) and summary of the seismic network (d-e).** The red line shows the height above sea level across an approximately W-E section spanning 10 km transecting the summit.

935 [Regional mid crustal anomalies around Mount Hood, Mount St. Helens, Mount Adams and Mount](#)
936 [Rainier](#)

937 To avoid repetition in the following sections, we discuss the regional anomalies in the mid to lower crust
938 around Mount Hood, Mount St. Helens, Mount Adams and Mount Rainier here in a single section.

939 Stanley (1984) performed a regional magnetotelluric (MT) study, identifying a conductive zone in the
940 region between Mount St. Helens, Mount Adam and Mount Rainier termed the Southern Washington
941 Cascades Conductor (SWCC). He suggested that this feature reflects a band of conductive sediments
942 and volcanic rocks of approximately Tertiary age. Hill et al. (2009) perform a higher-resolution MT study
943 over a 35 km² area near Mount St. Helens, as well as a 2D line stretching from Mount St. Helens to just
944 north of Mount Adams across the southern portion of the SWCC. They identify a conductor stretching
945 beneath the summit of Mount St. Helens, merging with a thick conductive region at ~15 km depth, and
946 stretching across to Mount Adams, where it has some weak upper crustal features. They interpret the
947 shallow zone beneath Mount St. Helens as a magma conduit supplying the volcano, which was showing
948 unrest during the survey. By extension, they suggest that the connected mid crustal feature also
949 represents 2–12% interconnected melt, supplying the dacitic magmas erupted at Mount St. Helens and
950 Mount Adams. Bedrosian et al. (2018) further investigate this region, and specifically whether anomalies
951 result from magma or sediments, using new high density MT data from an array spanning the entire
952 SWCC. They note that the conductor beneath MSH imaged by Hill et al. (2009) extends 10s of km away
953 from the volcano, extending into a metasedimentary belt. They believe the conductivity of dacite partial
954 melt would be dwarfed by the ~10x higher conductivity of these metasediments, and as a result
955 conclude MT techniques alone cannot unambiguously distinguish between regions of magma storage
956 vs. sedimentary deposits.

957 Flinders and Shen (2017) use 3D ambient-noise tomography to investigate the velocity structure of the
958 SWCC, with a particular focus around Mount Rainier. They find a large low velocity zone in
959 approximately the same region as the MT-defined SWCC, with its top at depths of ~10 km bsl towards
960 the northern extent closer to Mount Rainier, and ~15 km depth closer to Mount St. Helens and Mount
961 Adams. They suggest that the base is likely unconstrained in the model but may extend to ~27 km bsl.
962 They also suggest that portions of the SWCC have seismic velocities most consistent with the presence
963 of ~6% melt, particularly in the context of the large number of Quaternary volcanic vents over this feature
964 (>100).

965 In addition to local anomalies at Mount St. Helens, Ulberg et al. (2020) identify a broad region with low
966 P-wave velocity at >10 km depth around Mount Rainier to Mount Adams. They speculate that this may
967 indicate fluid or melt present, or high crustal temperatures.

968 Jiang et al. (2023) use ambient noise interferometry on a regional seismic network to further investigate
969 the origin of these crustal anomalies. Crucially, their approach uses data from the EarthScope array in
970 addition to regional seismic networks, which helps to mitigate edge effects allowing them to expand
971 their reconstruction to cover the area around Mount Hood. They identify two subparallel low Vs zones
972 at 15–30 km depth bsl. One zone stretches from Mount Rainier to Mount Adams, and the other from
973 Mount St. Helens to Mt Hood They interpret these anomalies as deep crustal magma sills with ~2.5–6%
974 melt.

975 [Mount Hood](#)

976 Construction of the modern edifice at Mount Hood began at ~500 ka. Activity has since been dominated
977 by remarkably homogenous andesitic (and sometimes dacitic) lava flows and domes, with no evidence
978 for explosive eruptions in the regional tephra record (Scott and Gardner, 2017). The three most recent
979 eruptive episodes are Polallie (13–20 kyrs), Timberline (1.5 kyrs), and Old Maid (~200 yrs, Koleszar et
980 al., 2012), with the Main Stage preceding this (>29 kyrs, Scott et al., 1997). We also discuss analyses
981 from the Parkdale flow (7.5–7.7 kyrs, Scott et al., 1997) and the Main Stage Cloud Cap lavas which
982 erupted from satellite vents between ~400–600 kyr (Keith et al., 1985).

983 **Mineral Compositions:** We obtain the following mineral compositions:

- 984 • N=15 Cpx analyses from the Main Stage and Parkdale Flow from Darr (2006).
- 985 • N=123 Cpx analyses from the Main Stage Cloud Cap, Main Stage, and Polallie from Cribb
986 (1997)

987 • N=109 Amp compositions from Koleszar (2011), Koleszar et al. (2012) and Loewen (2012) from
988 the Old Maid, Timberline and Polallie eruptive episodes.

989 The median Cpx-only pressure is ~1.4 kbar for W2021, and ~1.6 kbar for J2022, with W2021
990 extending as a tail to much shallower pressures (while J2022 shows the absence of very shallow
991 pressures typical of this barometer). The median Amp-only pressure is ~1.6 kbar regardless of
992 filters, which is remarkably similar to the Cpx-only pressure estimates.

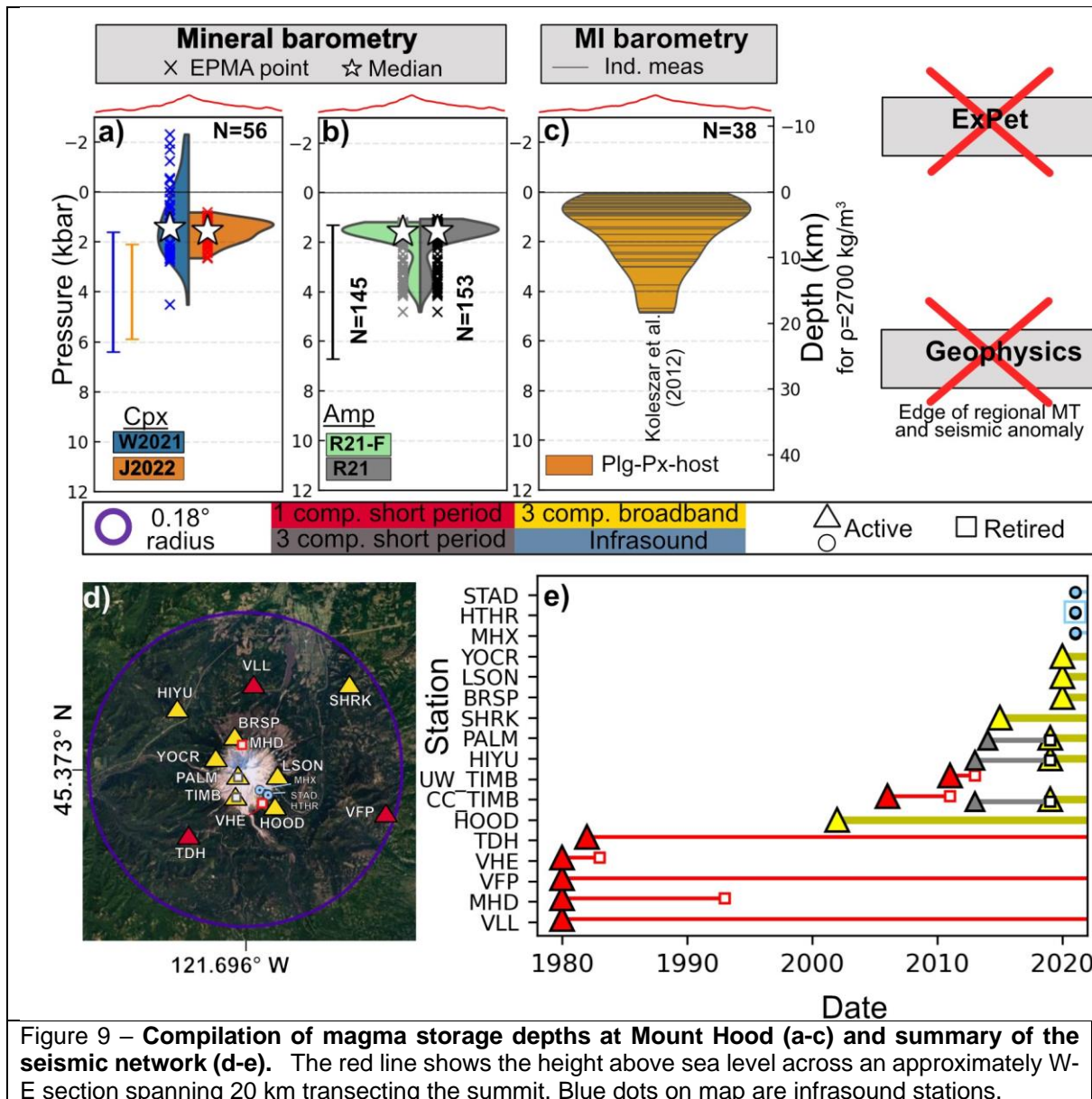
993 **Melt Inclusions:** Koleszar et al. (2012) present Plag, Opx, and Cpx hosted MIs (N=38) from the Old
994 Maid, Timberline, and Polallie Stages. A subset of MIs that were large enough for double polishing
995 (N=12) were measured using FTIR and yielded no CO₂ above the detection limit. The remaining MIs
996 (<60–80 μm diameter, N=28) were measured by SIMS. These inclusions contain CO₂ contents up to
997 2400 ppm, although they note that the lack of standards with >540 ppm CO₂ required their calibration
998 line to be extrapolated for these measurements. These high CO₂ contents are unusual in such evolved
999 materials, so Koleszar et al. (2012) suggest they may result from the presence of undetected
1000 microcracks with CO₂ contamination during sample preparation. They also note that many MIs contain
1001 vapour bubbles, which may contain additional CO₂. Their FTIR H₂O measurements range from 0.8–3.6
1002 wt%, while SIMS measurements range from 0.9–5.4 wt%. The higher SIMS H₂O contents may reflect
1003 the superior ability of smaller MIs to retain high volatile contents (e.g., less resistant to
1004 cracking/rupturing), although it is possible this disagreement also reflects calibration issues. They note
1005 that there is a general trend towards lower H₂O contents with increasing SiO₂, indicating MI entrapment
1006 during degassing induced-crystallization, which makes it hard to apply a filter based on H₂O contents.
1007 Thus, considering the poorly-constrained nature of CO₂, and the probable influence of degassing on
1008 H₂O, saturation pressure from these MIs are not a rigorous constraint on magma storage.

1009 **Experimental Petrology:** While Mount Hood andesite has been used widely as an experimental
1010 starting material, we are not aware of any experimental studies directly relating to magma storage
1011 conditions beneath Mount Hood. Additionally, erupted Mt Hood andesites are mixed magmas and are
1012 thus not representative of a single multiply-saturated liquid (Kent et al., 2010).

1013 **Geophysics:** Weaver et al. (1982) report the results from a 16–station seismic network established in
1014 1977 at Mount Hood. They find no significant velocity anomalies beneath Mount Hood indicative of
1015 magma reservoirs. Use of earthquakes directly, rather than through inversions for crustal structure, has
1016 been hindered at Mount Hood by the fact that low frequency earthquakes and tremor are exceedingly
1017 rare. Jones and Malone (2005) summarize that most earthquakes detected on the Mount Hood seismic
1018 network have characteristics of tectonic earthquakes, likely reflecting the northern edge of regional
1019 Basin and Range seismicity. Following a M4.5 earthquake in June 2002 located ~4.6 km south of Mount
1020 Hood, there was a swarm of >200 aftershocks, which Jones and Malone (2005) subdivide into four
1021 groups. A small subset of these earthquakes (Group D) occurred at very shallow depths. Jones and
1022 Malone (2005) suggest that these earthquakes may reflect volcanic processes beneath Mount Hood,
1023 although they do not speculate further as to whether these represent magma or fluid movement. Other
1024 than the regional mid-crustal anomalies discussed above, there are no further seismic constraints on
1025 upper crustal storage to our knowledge. In part, this reflects the fact that no local high-resolution study
1026 has been conducted using modern instrumentation. Poland et al. (2017) summarize available geodetic
1027 constraints at Mount Hood, which show no consistent deformation patterns that can be associated with
1028 volcanic activity since the 1980s.

1029 **Summary and Future work:** Future work remeasuring CO₂ and H₂O in MIs and their vapour bubbles
1030 using more robust SIMS or FTIR calibrations would help resolve whether the high-pressure MIs of
1031 Koleszar et al. (2012) represent a deeper magma storage region or an analytical artefact. Hints of
1032 higher-pressure storage (2–4 kbar) are perhaps seen in the Cpx and Amp pressures; coupled
1033 measurements of mineral chemistry and MIs within a single crystal would help to investigate this further.
1034 Like many of the volcanoes discussed so far, Mount Hood's seismic network has been recently
1035 densified with three-component broadband seismometers (Fig. 9e). Once sufficient earthquakes have
1036 been recorded on this network, local, passive-source inversions should provide additional constraints
1037 on the presence/absence of magma storage regions and low velocity zones, and a greater
1038 understanding of the origin of earthquakes at Mount Hood (Jones and Malone, 2005).

1039



1040

1041 **Mount St. Helens**

1042 Mount St. Helens is located 53 km west of Mount Adams and 35–50 km W of the main arc front, so can
 1043 be classified as a fore-arc volcano. It erupts primarily dacitic bulk compositions with plagioclase,
 1044 pyroxene and amphibole phenocrysts (Hildreth, 2007), although erupted products range from basaltic
 1045 to rhyodacite. Many display evidence of the mingling of basaltic and a dacitic magma (Pallister et al.,
 1046 2017). It is one of the youngest and most active volcanoes in the Cascades, erupting more than half its
 1047 75 km³ magma volume in the last 28 kyrs, and exhibiting five major explosive eruptions in the last 500
 1048 yrs. This high activity relative to other Cascade centers has been attributed to its location within a small
 1049 pull-apart basin (Pallister et al., 2017). Following its Plinian eruption in 1980 and re-awakening in 2004–
 1050 2008, it represents one of the best-studied Cascade volcanoes both in terms of petrology and
 1051 geophysics (Fig. 10).

1052 **Mineral Compositions:** We compile the following mineral data:

- 1053 • N=57 Cpx compositions from the Kalama (~1480 AD) and Castle Creek andesites (1.9–1.7 kyr
 1054 BP) from Cooper and Reid (2003).

- 1055 • N=21 Cpx from the 2004–2005 eruption from Rowe et al. (2008).
 1056 • N=4 Cpx from the Castle Creek andesite from Smith and Leeman (1993). N=49 from the 2004–
 1057 2005 episode obtained from the Rowe et al. (2008) USGS data repository, and an additional
 1058 N=77 analyses from Humphreys et al. (2019) attributed to Rowe et al. (2008).
 1059 • N=171 from the May 1980 cryptodome and pumice fall, the June-12th 1980 airfall, and the July
 1060 1980 pyroclastic flow from Humphreys et al. (2019).
 1061 • N=171 from the 1980 AD eruption from Loewen (2012).
 1062 • N=446 from samples spanning 1980–2004 AD from Thornber et al. (2008).
 1063 • N=54 from mafic Castle Creek samples from Wanke et al. (2019).

1064 The median Cpx-only pressure is 2.3 kbar using W2021, and 1.8 kbar using J2022, with relatively similar
 1065 distributions (although W2021 shows a deeper tail). Filtered and unfiltered Amp-only pressures are 3.1
 1066 and 3.2 kbar respectively, although, as for Cpx, the distributions are quite broad. In general, Amp
 1067 pressures are offset~ 1 kbar deeper than Cpx, which is well within the uncertainty of these methods.

1068 **Melt Inclusions:** Rutherford et al. (1985) measure 57 plag-hosted MIs from the May-18 pumice using
 1069 EPMA, calculating H₂O using volatiles-by difference techniques (~4.6 wt%). Blundy and Cashman
 1070 (2005) measure H₂O using SIMS in mostly Plag-hosted MIs (some Amp- and Opx-hosted) from blast
 1071 deposits, pyroclastic flows and domes from May-Oct, 1980. Texturally, many of these MIs show
 1072 evidence for connection to the outside of the crystal, and there is a correlation between H₂O and SiO₂.
 1073 These textural and chemical trends indicate decompression-induced degassing accompanying MI
 1074 entrapment, meaning that MIs saturation pressures may be weighted towards recording processes
 1075 occurring during magma ascent. Blundy and Cashman (2005) state that their preliminary FTIR
 1076 measurements indicate that CO₂ contents are very low, so pressures can be determined using H₂O-
 1077 only saturation pressures. However, Blundy et al. (2010) supplement the 2005 analyses with new SIMS
 1078 analyses of CO₂ in N=77 MIs from 9 eruptive episodes between 1970–1984, finding CO₂ above the
 1079 FTIR detection limit. We only use these later measurements. This is intriguingly similar to the scenario
 1080 at Mount Hood where Koleszar et al. (2012) find no CO₂ using FTIR, but abundant CO₂ using SIMS.
 1081 The SIMS analyses of Blundy et al. (2010) for MIs from the 1980 plinian episode have relatively low
 1082 CO₂ (<400 ppm) and high H₂O (~4–6 wt%), while the later subplinian to vulcanian and effusive events
 1083 have higher CO₂ and lower H₂O. They attribute these differences to CO₂-flushing as the eruption
 1084 progressed. Four MIs have 0.4–1.7 wt% CO₂, which Blundy et al. (2010) link to much deeper magma
 1085 storage.

1086 **Experimental phase equilibrium:** Rutherford et al. (1985) perform experiments on a bulk sample of
 1087 MSH dacitic pumice at 1–3.2 kbar, varying the fluid composition and oxygen fugacity. They show that
 1088 the observed phase assemblage and crystallinity of the May 18th 1980 magma can only be produced if
 1089 $P_{\text{H}_2\text{O}} \neq P_{\text{Total}}$, requiring either H₂O-undersaturation, or a relatively CO₂-rich melt. They conclude that the
 1090 upper part of the MSH magma reservoir was at a pressure of 2.2 ± 0.3 kbar, $P_{\text{H}_2\text{O}}$ was 50–70% of P_{total} ,
 1091 and T was 930 ± 10 °C. However, they note that the exact storage pressure is not constrained because
 1092 these conditions were not simultaneously satisfied in different experiments. Rutherford and Devine
 1093 (1988) perform additional experiments at 920 °C and 2.2 and 3.2 kbar, with variable f_{O_2} and $X_{\text{H}_2\text{O}}$ to
 1094 further investigate Amp stability. They find that the phase assemblage of the 1980 eruption including
 1095 Amp is reproduced at $P=2.2$ kbar, $T=920$ °C, and $X_{\text{H}_2\text{O}} \geq 0.67$, with a surge of Plag crystallization
 1096 occurring when $X_{\text{H}_2\text{O}}$ decreased just before eruption.

1097 Gardner et al. (1995) perform experiments at 1, 1.5, 2.5 and 3.5 kbar and 850 °C to determine storage
 1098 pressures and water fugacity of 6 dacitic magmas from the last 4000 yrs. For different dacite units, they
 1099 invoke storage depths between ~3.5–1.5 kbar. Their results suggest that 4000–3000 yrs ago, dacites
 1100 were H₂O-saturated (5.5–6.5 wt%), while more recently-erupted dacites were H₂O-undersaturated (<5
 1101 wt% H₂O). They suggest this shift represents increasing mafic input, which dilutes H₂O and adds CO₂
 1102 (and also explains the appearance of andesitic bulk compositions). Constraints on magma storage are
 1103 also provided by the stability of the mineral cummingtonite (a type of amphibole), which breaks down
 1104 to orthopyroxene (Geschwind and Rutherford, 1992), indicating similar storage conditions to Gardner
 1105 et al. (1995).

1106 Rutherford and Devine, (2008) perform experiments on the 2004–2006 dacite, suggesting that the Fe
1107 and Al-rich Amp cores formed at 2–3 kbar, and 900°C, as Amp forming in experiments at <2 kbar had
1108 lower Al than observed products. They suggest the observed An_{68–40} Plag compositions form when
1109 pressure drops to 2 kbar at 900°C, and the outer rims of some Amp phenocrysts may have formed at
1110 1–2 kbar.

1111 **Geophysics:** Scandone and Malone (1985) use subsidence recorded by electronic tiltmeters in June-
1112 November 1980 to make a first estimate of the reservoir depth supplying the 1980 eruption (~7–9 km,
1113 rlu). They also analyse earthquake hypocenters accompanying each explosive event, identifying an
1114 aseismic zone at ~ 7 km depth (rlu) extending vertically for 6+ km which they suggest is a magma
1115 reservoir connected to the surface by a ~50 m wide conduit. Barker and Malone (1991) use earthquake
1116 focal mechanisms to identify an aseismic zone at 7–11 km bsl associated with magma storage.
1117 Musumeci et al. (2002) relocate 447 earthquakes from the late 90s to produce a 1D velocity structure
1118 beneath Mount Saint Helens, and identify a magma reservoir at ~5.5–10 km depth (bsl), and a thin
1119 vertical conduit similar to that invoked by Scandone and Malone (1985). More recently, Waite and
1120 Moran, (2009) present a P-wave travel time velocity model using earthquake data recorded on the local
1121 network over 25 yrs, supplemented by 19 temporary broadband seismometers from 2005–2006. They
1122 identify a low-velocity zone at ~2–3.5 km bsl which they attribute to a shallow magma storage zone.
1123 Their model has limited resolution beneath 6 km, but they identify low velocities at ~5.5–8 km bsl in an
1124 aseismic zone, which approximately aligns with the older estimates described above.

1125 The numerous geophysical studies described above mostly imaged the upper crust, as travel time
1126 tomography struggles to produce high resolution images at >6 km depth. Kiser et al. (2016) present
1127 results from the active source portion of the iMUSH (imaging Magma Under St. Helens) project. They
1128 identify a high V_p/V_s anomaly at 4–13 km bsl which they attribute to magma storage, and a low V_p
1129 column extending from 15 km to the Moho to the southeast of Mount St. Helens. Kiser et al. (2018)
1130 build on this study, using a finite-frequency tomographic method to place more detailed constraints on
1131 the geometry of the magma storage region. They identify a number of low V_p anomalies forming a near
1132 continuous body spanning 3.5–14 km bsl, with the highest amplitude V_p anomalies at 4–6 km bsl
1133 (interpreted to represent 10–12% melt, dropping to ~8% at 7km depth, and continuing to decrease
1134 downwards).

1135 Ulberg et al. (2020) use local source V_s and V_p tomography as part of the iMUSH broadband array of
1136 70 broadband seismometers to image the upper 20 km of the crust beneath Mount St. Helens. They
1137 identify a low P- and S-wave anomaly at 6–15 km depth bsl, with a diameter of 5–7 km, which they
1138 interpret to represent a magma storage region with ~3% partial melt over ~15–20 km³. They also image
1139 the broader low P-wave velocity region discussed above in the section '*Regional mid crustal*
1140 *anomalies...*'. Ambient noise imaging from the same array showed low-velocity lower-crustal anomalies
1141 between Mount St. Helens and Mount Adams (Crosbie et al., 2019).

1142 Interestingly, neither Kiser et al. (2016, 2018), Ulberg et al. (2020), nor Crosbie et al. (2019) image the
1143 low velocity region at 2–3 km bsl identified by Waite and Moran (2009). Ulberg et al. (2020) suggest
1144 that the difference between the inversion techniques in the two studies may explain this discrepancy,
1145 while Kiser et al. (2018) suggest that the low velocity zone may have been a temporary anomaly related
1146 to dome-forming activity between 2004–2008. Alternatively, the magma body may be too small to be
1147 resolved at the relatively long wavelengths of microseismic noise used in ambient noise imaging
1148 (Crosbie et al., 2019).

1149 Lisowski et al. (2008) examine GPS deformation associated with the onset of unrest in 2004. They
1150 model the deformation in an elastic half space model as arising from a vertically-elongate magma
1151 reservoir centred at ~7–8 km (basl). Mastin et al. (2008) model geodetic data from 8 continuous GPS
1152 stations as an ellipsoidal source with its top at 5±1 km (basl), and the center offset 1.3–1.6 km east of
1153 the crater centre. The base of this source is less well constrained; they place it somewhere below 10
1154 km (likely 10–20 km basl).

1155 Anderson and Segall (2013) invert geodetic data from the 2004–2008 period, along with information on
1156 extruded lava dome geometry. Using a range of input parameters (e.g. melt H₂O), they show a
1157 probabilistic estimate of magma chamber geometry from 100 randomly sampled outputs from their

1158 Markov-Chain Monte Carlo simulations. They estimate that the centroid of the magma chamber is ~11–
 1159 18 km below the crater floor, with an aspect ratio of at least 2 (e.g. vertically elongated). On Fig. 10, we
 1160 show the extent of the magma chamber indicated on their Fig. 11 within the 67% contour line of different
 1161 simulations (e.g. 1 σ , 5.5–20.5 km). Wong and Segall (2020) build on this approach using a time-
 1162 dependent conduit flow model, inverting time series data for extruded dome volume, CO₂ emissions
 1163 and ground deformation. Their model favours an elongate chamber (width:height=0.13–0.55), at 9–17
 1164 km depth (top at 2.9–5.8 km depth). Extracting depths from their contours on their Fig. 8 to allow direct
 1165 comparison with Anderson and Segall 2013) yields depths of ~5–17 km.

1166 **Summary and Future work:** Relative to the rest of the Cascade arc, magma storage depths are well
 1167 constrained at Mount St. Helens, with various methods delimiting a vertically extensive magmatic
 1168 system ranging from ~5–12 km depth (Pallister et al., 2017). In general, the shallower geophysical
 1169 anomalies cluster at ~2–4 kbar, which is reasonably consistent with the median pressures from mineral
 1170 barometry, while MIs appear to record shallower processes, perhaps during ascent towards the surface.
 1171 However, given experimental and MI evidence for the importance of CO₂, it would be worthwhile re-
 1172 evaluating the CO₂ budget of Mount St. Helens MIs to account for any CO₂ which has partitioned into
 1173 the vapor bubble. Further MI work on more mafic cones in the general area may provide petrological
 1174 evidence for the geophysically imaged mid-crustal anomaly. The recent densification of three
 1175 component broadband stations will greatly increase the potential for local, passive-source inversions.
 1176 The biggest unanswered question revolves around whether the shallow low velocity anomaly of Waite
 1177 and Moran (2009) was an ephemeral feature which was difficult to resolve by other methods, or whether
 1178 it was an imaging artefact.

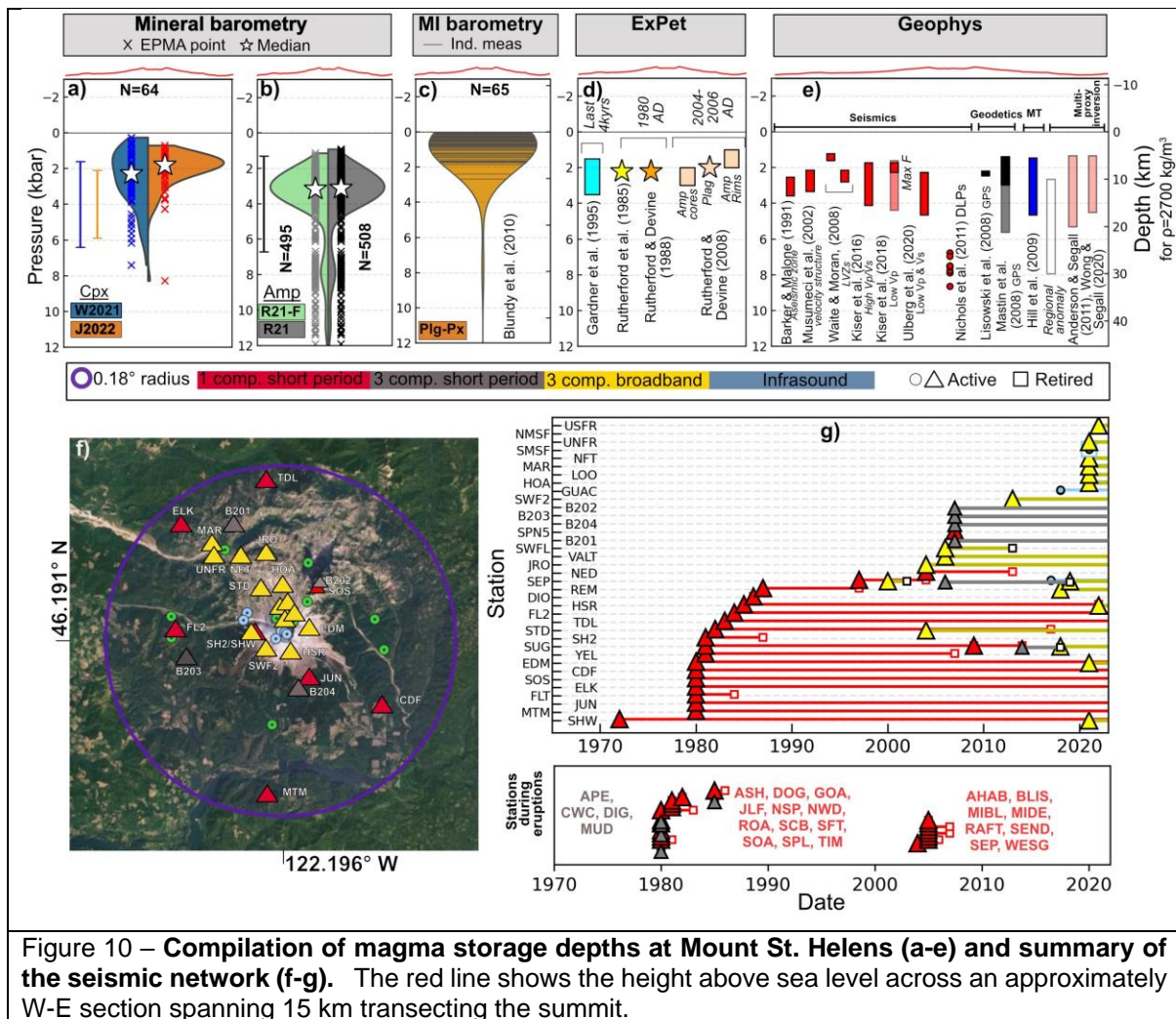


Figure 10 – **Compilation of magma storage depths at Mount St. Helens (a-e) and summary of the seismic network (f-g).** The red line shows the height above sea level across an approximately W-E section spanning 15 km transecting the summit.

1180 [Mount Adams](#)

1181 Mount Adams is an andesitic-dacitic stratovolcano, located east of Mount St. Helens along the main
1182 arc-axis. The large edifice lies in the centre of a larger volcanic field with ~120 spatter, scoria cones,
1183 and shield volcanoes. Vents within ~6 km of the summit are classified as flank vents because of
1184 compositional similarity to summit lavas, while those further away have basaltic or basaltic-andesitic
1185 compositions (Hildreth, 2007).

1186 **Mineral Compositions:** J. Fierstein supplied previously unpublished analyses for N=45 Amp and
1187 N=1219 Cpx from the post-glacial (0–15 kyr) period of Mount Adams (samples discussed in Hildreth
1188 and Fierstein, 1997). The median Cpx-only pressure is ~0.4 kbar for W2021 and ~1.3 kbar for J2022,
1189 which is a similar offset to that seen between these barometers at other edifices. In contrast, Amp-only
1190 pressures span a significantly greater range, from ~2-6 kbar, with a median pressure of 3.9 kbar.

1191 **Experimental phase equilibrium & Melt Inclusions:** We are not aware of any phase-equilibrium
1192 constraints for Mount Adams or MI studies.

1193 **Geophysics:** Apart the regional mid crustal anomalies discussed above, there are no seismic
1194 constraints for magma storage at Mount Adams, reflecting the fact there is only a single 1 component
1195 short period seismometer installed in the area (Fig. 11d), and no detailed local studies have been
1196 performed. The iMUSH array extends to the western flanks of Mount Adams, and does indicate potential
1197 for melt storage in the lower crust west of Adams (Kiser et al., 2016; Crosbie et al., 2019; Ulberg et al.,
1198 2020). However, the lack of stations on or east of the summit, due to permitting constraints, makes it
1199 difficult to image a proximal magma system. In addition, no ground based geodetic studies have been
1200 performed at Mount Adams, and while InSAR shows coherence, there were no obvious signals of
1201 deformation in the 1990s to early 2000s (Poland et al., 2017).

1202 **Summary and Future work:** The absence of upper crustal geophysical constraints, MIs and
1203 experimental petrology is very concerning, particularly given Mount Adams is classified as high threat,
1204 and ranked the 34th most hazardous US volcano. While the difference in Cpx-only and Amp-only
1205 pressures may reflect different storage regions with different crystallizing phases, these barometers are
1206 too imprecise to be sure without other proxies for magma storage. A densified seismic network would
1207 be an important next step, along with more focused petrological studies specifically targeting magma
1208 storage depths (e.g., MIs).

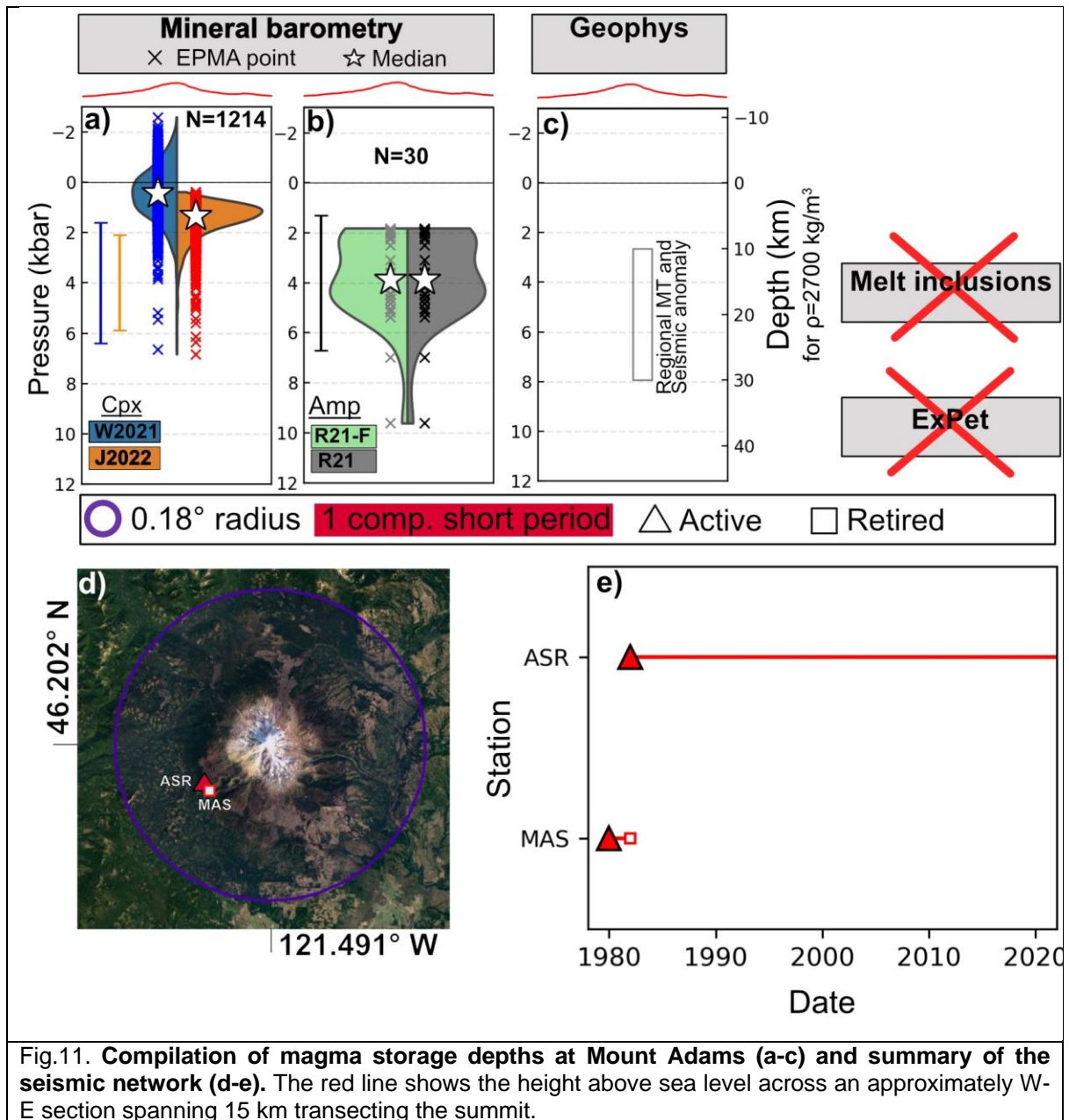


Fig.11. **Compilation of magma storage depths at Mount Adams (a-c) and summary of the seismic network (d-e).** The red line shows the height above sea level across an approximately W-E section spanning 15 km transecting the summit.

1209

1210 **Mount Rainier**

1211 Mount Rainier is the highest elevation Cascade peak, although the volume of volcanic material is
 1212 smaller than it appears (130 km^3 vs. 450 km^3 for Mount Shasta), as a result of it being built on top of
 1213 older underlying terrains. It is made predominantly of pyroxene andesites-dacites with minor amphibole
 1214 ($59\text{--}66 \text{ wt}\% \text{ SiO}_2$; Hildreth, 2007). Unlike other Cascade volcanoes with numerous peripheral vents,
 1215 Rainier's activity primarily occurs on the main edifice. While lava flows dominate, two large pumice falls
 1216 $>10 \text{ km}^3$ from $\sim 190 \text{ ka}$ and $\sim 380 \text{ ka}$ have been identified as well as ~ 10 post-glacial pumice deposits
 1217 (Hildreth, 2007; Mullineaux, 1974; Sisson and Lanphere, 2000; Sisson and Vallance, 2009).

1218 **Mineral Compositions:** We obtain the following mineral analyses:

- 1219 • N=12 Cpx and N=5 Amp analyses from the large andesitic Burroughs Mountain lava flow, which
 1220 is thought to have been emplaced at $\sim 496 \text{ kyr}$ at the beginning of activity at the modern edifice
 1221 of Mount Rainier (Stockstill, 1999).
- 1222 • Representative analyses (N=5 Cpx and N=4 Amp) from Venezky and Rutherford (1997, N=5
 1223 Cpx, N=4 Amp) from the 2.2 ka tephra layer

- 1224 • Unpublished EPMA analyses (N=13 Amp, N=35 Cpx) from the Sunset Amphitheatre dacite
 1225 (~85 ka, see Sisson et al. 2019), cognate plutonic blocks from other Rainier lava flows (T.
 1226 Sisson, Pers. Comms), and Cpx (N=27) and Amp (N=9) from K-rich spessartite samples, which
 1227 occurs in small eruptions on the flank and vent, and are thought to bypass the main plumbing
 1228 system (Sisson et al., 2014).

1229 Considering all formations together, the median Cpx-only pressure is ~2.7 kbar using W2021 and ~2
 1230 kbar using J2022. While the number of analyses is relatively small for each formation, Cpx-only
 1231 pressures from the spessartite samples are deeper than the mafic Sunset Amphitheatre samples
 1232 (median of 4.4 vs 2.2 kbar using W2021, 2.9 kbar vs. 1.4 kbar using J2022, Supporting Fig. S5). This
 1233 is consistent with the hypotheses that these spessartite melts bypass the main plumbing system.
 1234 Burroughs Mountain shows a very broad distribution of pressures, overlapping with Sunset and
 1235 spessartite samples (-2 to 10 kbar, Supporting Fig. S5a). For Amp-only barometry, the median pressure
 1236 for all samples is 3.1 kbar. Only two spessartite-hosted Amp pass the quality checks of Ridolfi (2021) –
 1237 these return pressures which are ~1-2 kbar deeper than Sunset Amphitheatre amphiboles, although far
 1238 more analyses per formation than could be obtained from the literature are required to accurately
 1239 resolve any differences in magma storage using mineral compositions (Supporting Fig. S5b).

1240 **Experimental phase equilibrium:** Venezky and Rutherford (1997) investigate natural products from
 1241 the 2.2 ka tephra layer C from Mount Rainier, and conduct experiments at 0.25–2.5 kbar. They interpret
 1242 the products of this eruption to form during mixing of an andesitic and dacitic magma. Their experiments
 1243 on a powdered Rainier dacite show that the matrix glass composition is produced at H₂O-saturated
 1244 conditions at <0.5 kbar (~2.4 km). Determining the storage conditions of the andesitic melt is harder
 1245 (see discussion in MI section below), although they suggest that the presence of Amp indicates storage
 1246 at >7 km depth, which is reasonably consistent with the Amp-only pressures we obtain.

1247 **Melt Inclusions:** We are not aware of any published MI work measuring both CO₂ and H₂O. Venezky
 1248 and Rutherford (1997) describe an “exhaustive” attempt to find suitable MIs, noting that most inclusions
 1249 were either too small to analyse, or were partially crystallized. They analyse 20 Plag- and Pyroxene-
 1250 hosted MIs in the dacitic magma, obtaining H₂O contents of 2.4–3.3 wt% by volatiles by difference. For
 1251 the andesitic magma, they obtain 4–6 wt% (although they acknowledge possible issues due to post-
 1252 entrapment crystallization). These H₂O contents were used to infer entrapment depths of ~2.4 km for
 1253 the dacite, and >7 km for the andesite. However, volatile-by-difference methods are associated with
 1254 large uncertainties (Hughes et al., 2019). Additionally, ongoing MI work indicates that Rainier melts are
 1255 relatively CO₂-rich and H₂O-poor (T. Sisson, Pers. Comms), so we do not believe it is insightful to
 1256 calculate H₂O-only saturation pressures based on volatile-by-difference methods.

1257 **Geophysics:** Moran et al. (1999) investigate P-wave velocities using a local earthquake tomography
 1258 imaging experiment. They identify a ~10–15 km wide low velocity zone at 1–14 km bsl. Based on the
 1259 P-wave speeds (6 km s⁻¹) and the absence of earthquakes within this cylindrical anomaly, they suggest
 1260 that this anomaly consists of hot fractured rock with the possible presence of small amounts of melt and
 1261 fluid. The absence of significant S-wave attenuation indicates that no large, continuous bodies of melt
 1262 or fluid exist in this volume.

1263 McGary et al. (2014) use data from the CAFE (Cascade Array for Earthscope) experiment, which
 1264 collocated seismic and magnetotelluric data in a E-W transect passing near Mount Rainier. While they
 1265 mostly image the deeper structure down to the subducting slab, they do image a crustal conductor they
 1266 infer to represent a magma reservoir. However, this feature is offset 6–10 miles from the volcanoes
 1267 summit, so further investigation of this feature is warranted to determine whether it is magma or another
 1268 source of conductivity (Bonner, 2015). Obrebski et al. (2015) jointly inverted receiver functions and
 1269 ambient-noise-derived phase-velocity dispersion curves. No unambiguous low-velocity bodies were
 1270 detected in the upper crust, although signals were complicated and station spacing of > 10 km probably
 1271 cannot resolve a magma body the size of that imaged by Moran et al. (1999). There are also 18 LP
 1272 earthquakes located by Nichols et al. (2011).

1273 From a geodetic perspective, no deformation has been detected at Mount Rainier since at least the
 1274 1980s, despite numerous levelling and GPS surveys, CGPS sites and InSAR acquisitions (Poland et
 1275 al., 2017). Overall, these geophysical constraints are reasonably consistent with depths from

1276 petrological methods, with no concrete evidence from either method for extensive magma storage
 1277 below ~6 kbar (or 20 km).

1278 **Summary and Future work:** Mount Rainier is the 3rd most hazardous volcano in the US (Ewert et al.
 1279 2018, Fig. 1), and while a lot of the hazard is somewhat decoupled from volcanic activity (e.g. edifice
 1280 collapse, lahars from existing materials), its proximity to the major population centers of Seattle, Yakima,
 1281 Tacoma and Portland should justify further petrological and geophysical study. Specifically, MI studies
 1282 could provide insights into the storage conditions of the andesitic melt, perhaps focusing on the pumice
 1283 deposits documented by Sisson and Vallance (2009). The recent densification of the seismic network
 1284 (Fig. 12f) should help to further constrain the origin of seismic anomalies beneath Mount Rainier, and
 1285 determine whether or not these reflect melt.

1286

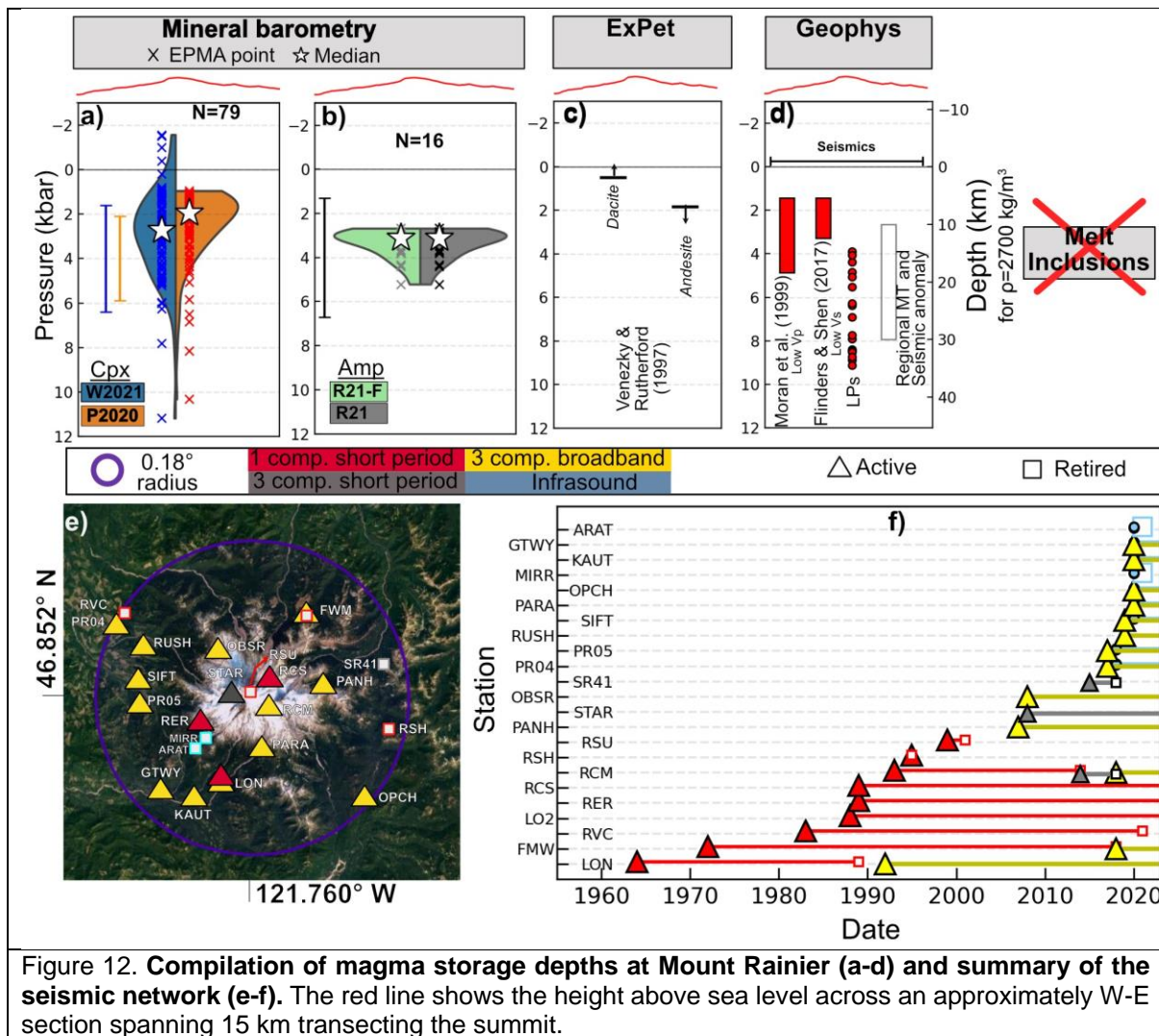


Figure 12. **Compilation of magma storage depths at Mount Rainier (a-d) and summary of the seismic network (e-f).** The red line shows the height above sea level across an approximately W-E section spanning 15 km transecting the summit.

1287

1288 **Glacier Peak**

1289 Glacier Peak is a predominantly dacitic edifice that has substantially less topographic prominence
 1290 above neighbouring peaks than many US Cascade volcanoes (Fig. 13d). The early history of Glacier
 1291 Peak was eroded during the last major glaciation. Since glacial retreat at ca. ~15 ka (Waite et al., 1995),
 1292 Glacier Peak has produced at least 9 pumice layers indicative of large explosive eruptions and past
 1293 eruptions have been characterised by numerous lahars. Thus, its activity more closely resembles Mount
 1294 St. Helens rather than the many other effusion-dominated Cascade volcanoes.

1295 **Mineral Compositions:** We were only able to obtain N=19 Cpx compositions from the Lightning Creek
1296 high magnesian basaltic andesite from Sas et al. (2017). The median Cpx-only pressure is ~2.2 kbar
1297 for both W2021 and J2022.

1298 **Melt Inclusions:** Shaw (2011) measure 16 olivine-hosted MIs from a primitive calc-alkaline basalt and
1299 a primitive low-potassium olivine tholeiite cinder cone (data reported in Venugopal et al., 2020).
1300 However, Shaw (2011) did not measure CO₂ in MI vapour bubbles. Venugopal et al. (2020) make a
1301 prediction of the amount of bubble CO₂ by assuming the same proportion of melt-vapour partitioning as
1302 at their measurements at Mount Meager. However, the partitioning of CO₂ into a vapour bubble is very
1303 dependent on the amount of PEC varies to a large extent even within a single eruption (Wieser et al.
1304 2021, 2023c), let alone between volcanoes. Thus, we favour stating minimum estimates using just glass
1305 volatile contents from Shaw (2011) rather than using the bubble reconstructions of Venugopal et al.
1306 (2020).

1307 **Experimental phase equilibrium:** We are not aware of any phase equilibrium experiments relevant
1308 to Glacier Peak.

1309 **Geophysics:** We are not aware of any geophysical constraints on magma storage, other than
1310 identification of 8 LP earthquakes (Nichols et al., 2011). There is only a single one-component short-
1311 period seismometer, so the lack of seismic constraints other than LPs is not surprising (Fig. 13). No
1312 ground-based geodetic studies have been attempted, and InSAR hasn't detected any deformation
1313 (although the ice-covered summit and heavily vegetated flanks make coherence challenging; Poland et
1314 al., 2006).

1315 **Summary and Future work:** Glacier Peak is ranked as very high threat, and the 15th most hazardous
1316 US volcano. The absence of petrological or geophysical constraints on magma storage is a very clear
1317 data gap to address with future work.

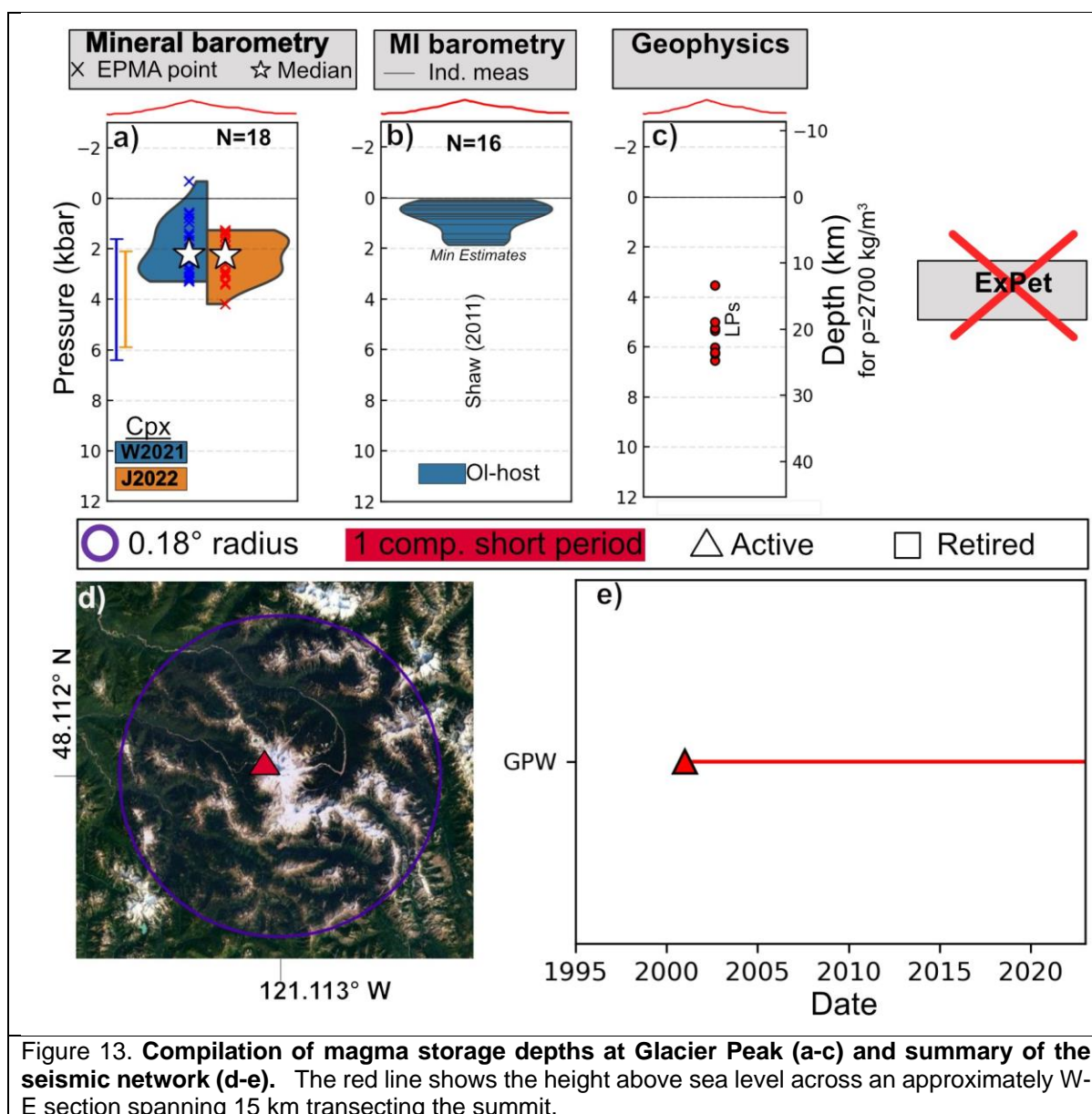


Figure 13. **Compilation of magma storage depths at Glacier Peak (a-c) and summary of the seismic network (d-e).** The red line shows the height above sea level across an approximately W-E section spanning 15 km transecting the summit.

1318

1319 **Mount Baker**

1320 Mount Baker is a stratocone situated within a larger multi-vent volcanic field that has been active since
 1321 1.3 Ma. It is one of the youngest volcanoes in the Cascades, with most of the modern edifice built over
 1322 the last 40 ka (Hildreth et al., 2003). The larger volcanic field is predominantly andesitic and rhyodacitic
 1323 in composition, with basalt and dacite making up only ~1–3% of the total volume. Mt Baker itself
 1324 comprises of andesites, two pyroxene dacites, with some olivine-bearing andesites (Hildreth et al.,
 1325 2003)

1326 **Mineral Compositions:** We obtained the following mineral analyses:

- 1327 • N=12 Amp and N=133 Cpx reported in Gross (2012) from three mid Pleistocene dacitic lava
 1328 flows Nooksack Falls (~149 ka), Cougar Divide (~613 ka) and Mazama Lake of uncertain age
 1329 (Hildreth et al., 2003).
- 1330 • Cpx from the more primitive basalts and Mg-rich andesites erupted at Mount Baker, with N=17
 1331 Cpx from Baggerman and DeBari, (2011), N=32 Cpx from Sas et al. (2017), N=28 Cpx from
 1332 Mullen and McCallum, (2014), and N=26 Cpx from Moore and DeBari, (2012).

1333 The median Cpx-only pressure is 2.4 kbar for W2021 and 1.8 kbar for J2022. There is significant overlap
 1334 between Cpx from dacitic and more mafic samples, with no consistent differences emerging for both
 1335 W2021 and J2022 (Supporting Fig. S5). The N=12 Amp from the dacites examined by Gross (2012)

1336 yield a pressure of ~2.9 kbar (between the median Cpx pressures of 1.7 and 2.9 kbar from J2022 and
1337 W2021 for these dacites).

1338 **Melt Inclusions:** Shaw (2011) measure 8 olivine-hosted MIs from Mount Baker (reported by Venugopal
1339 et al., 2020), with the same caveats regarding CO₂ as described for Glacier Peak. These MIs return
1340 pressures between 0–2 kbar, which represent minimum estimates as bubble CO₂ was not directly
1341 measured.

1342 **Experimental phase equilibrium:** We are not aware of any phase equilibrium experiments relevant
1343 to Mount Baker.

1344 **Geophysics:** Seismically, Mount Baker is relatively quiescent, with most shallow (<3 km) events
1345 thought to reflect activity of the glacier. We find one abstract describing a local seismic survey
1346 conducted at Mount Baker but no clear link to magma storage is made (Rohay and Malone, 1977). The
1347 lack of seismic data is unsurprising given the sparse coverage of the seismic network. At the time of
1348 writing, there is only a single three component broadband seismometer within 20 km. Nichols et al.
1349 (2011) report 31 LPs earthquakes from Mount Baker, more than any other Cascade volcano.

1350 Mount Baker experienced a period of thermal unrest in 1975, investigated retrospectively by Crider et
1351 al. (2011). In 1975, a large area of snow-free ground was created in the crater, with high magmatic gas
1352 emissions, and an accompanying increase in gravity in the 30 yrs following this period. While there is
1353 some debate about whether this episode can be magmatic given the lack of seismicity, Crider et al.
1354 (2011) note the presence of recent aseismic intrusions at other arc volcanoes worldwide (e.g., Lu et al.,
1355 2000), indicating that an absence of seismicity doesn't necessarily mean an intrusion didn't happen.
1356 Unfortunately, there was insufficient monitoring data to place detailed constraints on this episode
1357 beyond the speculation that it was likely caused by intrusion into the mid crust.

1358 Hodge and Crider (2010) investigate edifice deflation between 1981 to 2007 recorded by continuous
1359 GPS and EDM at Mount Baker. This deflation is best recreated by a source at ~5.8 km depth (basal,
1360 ~2000 m), located 1.5 km to the E-NE of the summit. This aligns reasonably well with Cpx-only and
1361 Amp-only pressures. Poland et al. (2017) describe challenges relating to InSAR at Mount Baker as a
1362 result of poor coherent on the edifice because of ice and snow, and vegetation on the lower flanks,
1363 meaning data is only possible to collect over a narrow window in late summer on the mid flanks.

1364 **Summary and Future work:** The paucity of data for this very high threat volcano is a concern. Mount
1365 Baker is an obvious target for MI work given the presence of tephra layers. Experimental phase
1366 equilibrium would also help to place constraints on storage conditions. Without a concerted geophysical
1367 campaign, it is unlikely that meaningful magma storage information will be gleaned from the current
1368 seismic network without significant densification.

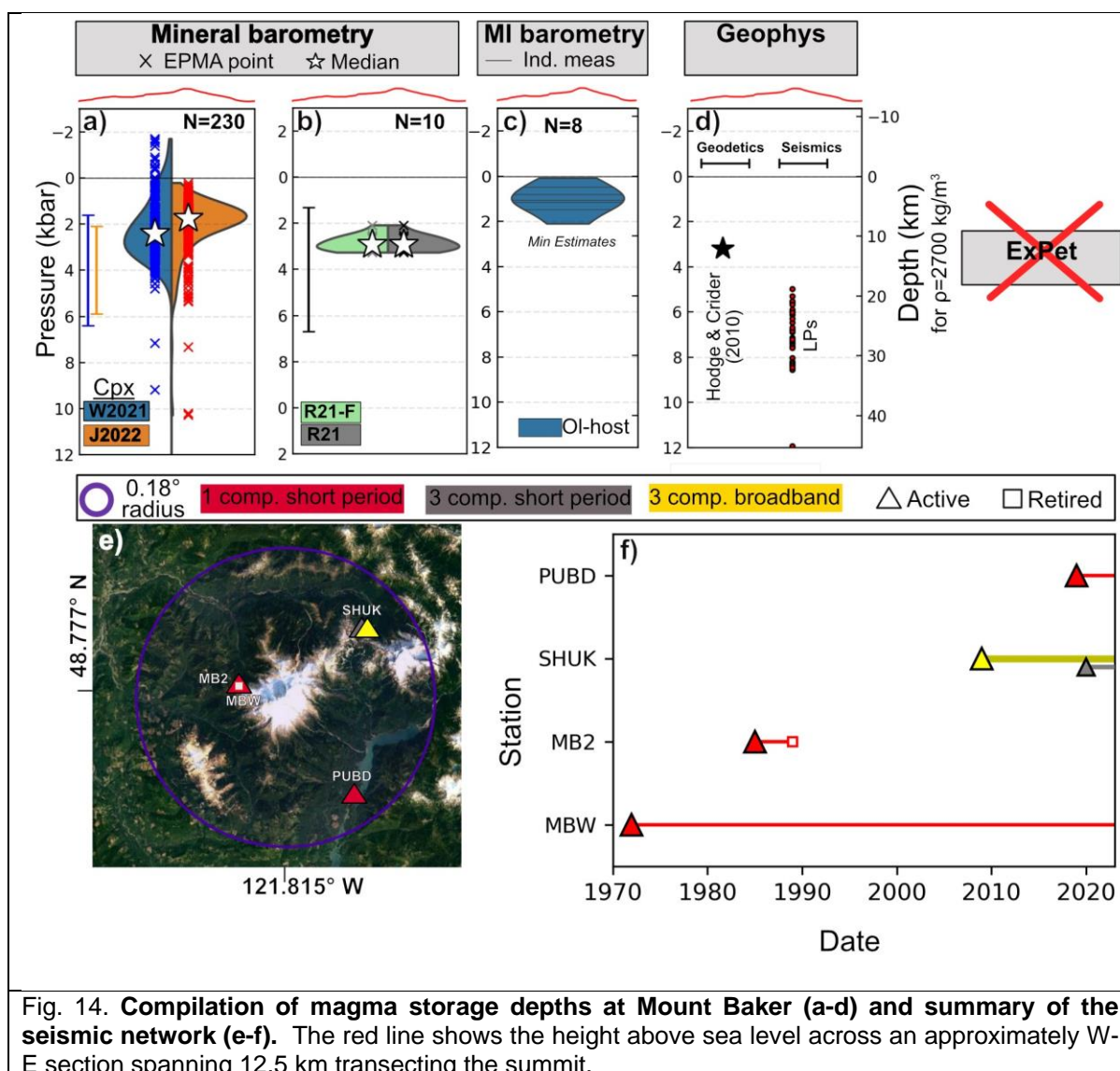


Fig. 14. **Compilation of magma storage depths at Mount Baker (a-d) and summary of the seismic network (e-f).** The red line shows the height above sea level across an approximately W-E section spanning 12.5 km transecting the summit.

1369

1370 **Canadian Garibaldi Volcanic Belt:**

1371 The Garibaldi Volcanic Belt consists of 2300 distinct vents, and 22 major edifices, including Glacier
 1372 Peak and Mount Baker (Hildreth, 2007). Here, we focus our discussion of the available data for the
 1373 Canadian segment of this volcanic belt, given differences in volcano monitoring on either side of the
 1374 border. The major Canadian edifices include Mount Garibaldi, Garibaldi Lake, Mount Meager, Salal
 1375 Glacier, Bridge River. A wide variety of compositions are present in this Canadian segment, with dacites
 1376 and rhyodacites at Mount Garibaldi and Mount Cayley, and high Si rhyolites at Mount Garibaldi
 1377 (Hildreth, 2007). These volcanoes also erupt olivine-bearing basalts and basaltic-andesites (Venugopal
 1378 et al., 2020).

1379 **Mineral Compositions:** We compile N=15 Cpx compositions from basaltic andesite samples from the
 1380 Garibaldi Lake Volcanic Field (Fillmore, 2014). We were unable to find any other mineral data. W2021
 1381 yields median pressures of 0.19 kbar, and 1.8 kbar for J2022.

1382 **Experimental phase equilibrium:** We are not aware of any experimental phase constraints on magma
 1383 storage conditions in the Garibaldi Volcanic Belt.

1384 **Melt Inclusions:** As mentioned in the introduction, Venugopal et al. (2020) perform glass and vapour
 1385 bubble measurements, but do not perform an instrument specific Raman calibration. Given that their
 1386 high CO₂ densities are thermodynamically impossible at room temperature, it seems highly likely the
 1387 amount of CO₂ in the vapour bubble was overestimated. We show their vapour-bubble reconstructed

1388 CO₂ alongside glass-only saturation pressures for completeness. Re-analysis of a subset of bubbles
 1389 could be used to correct the original Raman data (as different Raman calibrations are reasonably
 1390 parallel to one another, Lamadrid et al., 2017).

1391 **Geophysics:** There are no geodetic constraints on magma storage in the Garibaldi Volcanic belt. No-
 1392 ground based geodetic studies have been performed, and while C-band InSAR obtains some coherent
 1393 images on the volcanoes flank, InSAR is generally hindered by vegetated slopes and ice-covered
 1394 summits (Poland et al., 2017). We do not find any direct seismic constraints on magma storage beneath
 1395 these volcanoes. Querying the IRIS database from 1975-2023 for the Canadian networks yields 4
 1396 seismometer stations in the general vicinity of the Garibaldi Volcanic Belt. The broader distribution of
 1397 vents and less well defined summits relative to the US Cascades makes it harder to define clear query
 1398 criteria. Instead, we show volcanic regions on Fig. 15. There is a 3bb station close to Whistler (WSLR,
 1399 2013–present), and a second 3bb station is present near Squamish (WPB), ~27 km south of Mount
 1400 Garibaldi (1bb 1996–2018, 3bb 2018–present). There was a 3bb station ~8km W of Mount Meager and
 1401 10–15 km SW of Salal Glacier between 2016–2019, and a 3bb station about ~20km ESE along the
 1402 same river valley from 1993–1998, although it appears there are currently no stations in this area. Lu
 1403 and Bostock (2022) use the record from these 4 stations to identify 48 deep long period earthquakes
 1404 (DLPs) at ~4–45 km depth in the region near Mount Meager.

1405 **Summary and Future work:** The paucity of work on the Garibaldi Volcanic Belt likely reflects its relative
 1406 inaccessibility, snow and ice cover, and the lower hazard compared to the more active, US-based
 1407 volcanoes.

1408

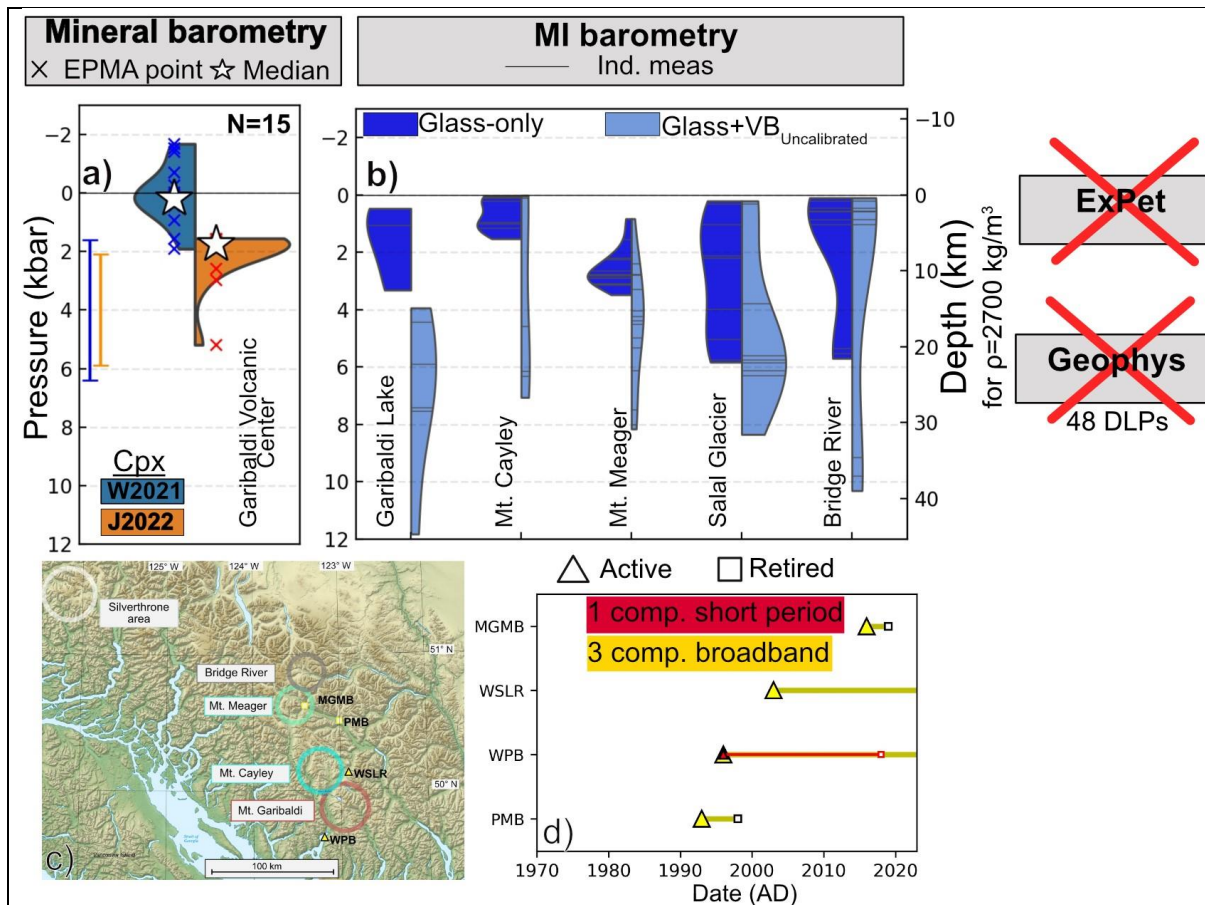


Fig. 15. Compilation of magma storage depths for the Canadian Garibaldi Volcanic Belt (a-b) and summary of the seismic network (c-d). Circles in c) show the approximate location of volcanic fields. Map in c) adapted from Sémhur (2007).

1409 [Arc-Scale trends](#)1410 [Data Availability](#)

1411 Our compilation shows the presence of many concerning data gaps affecting our knowledge of magma
1412 storage depths along the Cascade Arc. The quantity of data available along the arc is highly variable,
1413 and is also poorly correlated with the USGS threat index for individual volcanoes (Fig. 1; Ewert et al.,
1414 2018). Some systems are relatively well covered, but many high threat volcanoes show a disturbing
1415 paucity of geochemical and geophysical constraints on the nature of crustal magma storage. For
1416 example, at the second highest threat volcano in the Cascades (Mount Rainier, 3rd highest threat
1417 volcano in the US) we have no magma storage depth constraints from MIs, very few reported Amp and
1418 Cpx compositions, one experimental pressure constraint, and only two seismic constraints. Recent
1419 deployment of 13 broad band seismometers (Fig. 12f) provides potential for better seismological
1420 imaging in future (e.g., receiver functions, P and S wave topography). Mount Hood (6th highest threat
1421 in US) and Three Sisters (7th highest threat in US) are also very understudied. Available MIs from Mount
1422 Hood are limited and potentially unreliable due to SIMS calibration issues, and there are no detailed
1423 geophysical or experimental constraints on magma storage depths. Similarly, the Three Sisters have
1424 no usable MI data, no seismic studies, and no experimental studies placing precise constraints on
1425 magma storage reservoir depths. The only real depth constraints at Three Sisters come from a geodetic
1426 inversion of the 1998 inflation episode. However, it has been suggested based on spring chemistry and
1427 the lack of surface volcanism <10 ka that numerous intrusions likely occur in the deforming area with a
1428 very low probability of eruption (Evans et al., 2004). Thus, it is unclear if these geodetic estimates are
1429 providing useful information on the storage depths of melts. In addition, Mount Baker and Glacier Peak,
1430 which are both ranked as very high threat (#14 and #15 highest threat in US) have also been greatly
1431 understudied from both a petrological and geophysical perspective.

1432 [Probable trends](#)

1433 With the caveat of the relatively sparse and variable data coverage, we compile the available
1434 geophysical (Fig. 16a) and mineral (Fig. 16b) constraints on magma storage depth as a function of
1435 latitude to investigate along-arc trends in magma storage.

1436 From a geophysical perspective, the vast majority of constraints on proximal magma chambers (rather
1437 than regional anomalies) are clustered at depths corresponding to ~1–5 kbar, with only magnetotelluric
1438 anomalies, LP earthquakes and regional seismic surveys returning higher pressures.

1439 Considering the high imprecision of mineral-only barometers, Cpx-only pressures from J2022 and Amp-
1440 only pressures from R2021 are remarkably constant along the arc, although the Amp-only pressures
1441 show slightly more scatter. In general, the median pressures from these mineral-only barometers
1442 suggest that the vast majority of magma storage occurs in the upper 4 kbar (~0–15 km) of the crust.
1443 The general agreement within the ± 2 –3 kbar uncertainty of Amp and Cpx-based barometers gives us
1444 confidence in this result, along with the fact that geodetic and seismic constraints on magma storage
1445 generally have depths equivalent to ~0–5 kbar. With the limitations of the reported information, it is
1446 difficult to interpret whether the spread of individual calculated pressures for a given volcanic center
1447 represents true transc crustal storage or analytical uncertainty (Wieser et al. 2023b).

1448 The general confinement of magma storage estimates at pressures less than 4 kbar has been noted in
1449 a recent global compilation of geophysical estimates of magma storage depths in volcanic arcs, cyan
1450 histogram, Fig. 16b). Rasmussen et al. (2022) describe a correlation between water contents in melt
1451 inclusions from arcs and geophysically-determined magma storage depths, with the relationship
1452 between depth and H₂O plotting along the water-saturation curve. They propose two possible
1453 explanations: 1) H₂O controls magma storage depth through an increase in viscosity accompanying
1454 water exsolution (which they refer to as a 'mantle control') or 2) H₂O is diffusively reset at a depth
1455 determined by a 'crustal control'. The authors infer that a crustal control would cause correlations
1456 between ratios such as Nb/Ce and Ba/La to be lost, while a mantle control would preserve these
1457 relationships. Based on the preservation of strong H₂O-incompatible element ratios in the Aleutians,
1458 Rasmussen et al. (2022) favour a mantle control, with primary magmatic water contents controlling
1459 magma storage depths.

1460

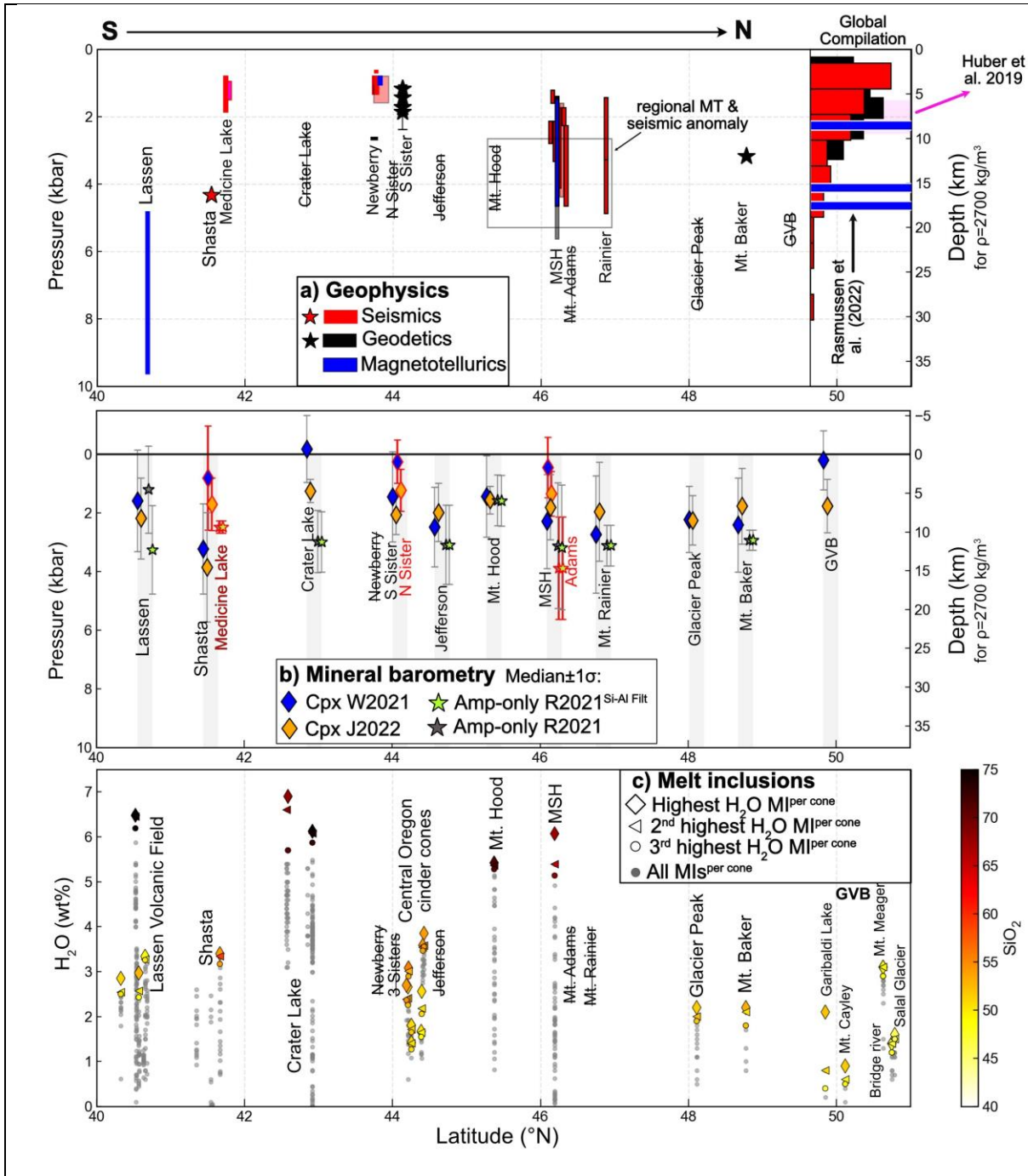


Figure 16: Summary of magma storage depths along the Cascades, with the x axis showing approximate latitude (Medicine Lake and Mount Adams are shifted slightly from true latitude to avoid overlap with Shasta and MSH respectively). a) Compilation of geophysics for each center. The histogram shows a global compilation from Rasmussen et al. (2022) using the same color scheme as for the Cascades, and the 2 ± 0.5 kbar from the compilation of Huber et al. (2019). b) Compilation of mineral barometry. Symbols show the median pressure, and errorbars show the standard deviation of calculated pressures for each volcano. Red outlines on symbols are used for Medicine Lake and MSH because of overlaps in latitude with Shasta and Mount Adams. c) H₂O contents from melt inclusions, with the 3 most H₂O-rich melt inclusions from each volcano/cinder cone colored based on the melt inclusion SiO₂ content. Tephra samples collected at different locations but from the same source (e.g., the S17 cone, Mount Shasta) are grouped as one. Volcanoes with no constraints are shown with crossed out text.

1462 To investigate the hypothesis of Rasmussen et al. (2022), we consider trends in H₂O with latitude along
1463 the Cascades, selecting the three most H₂O-rich MIs from each volcanic center (colored diamonds,
1464 triangles and circles, Fig 16c) as representative of the H₂O contents most resistant to degassing and
1465 diffusive re-equilibration. The relationship of Rasmussen et al. (2022) only applies to mafic magmas, so
1466 we color-code the most H₂O-rich melt inclusions by SiO₂ content (Fig. 16c). Unlike compiled magma
1467 storage depths, H₂O contents in the most mafic samples (yellow and orange colors) show considerable
1468 variation along strike.

1469 When considering all melt inclusion compositions, a strong positive correlation is present between SiO₂
1470 and H₂O contents (Supporting Fig. S3). If a H₂O-saturated mafic magma stalls in the crust and
1471 differentiates (as in the model of Rasmussen et al. 2022), the H₂O content in the melt would track the
1472 change in volatile solubility from basalt to rhyolite. However, different solubility models show vastly
1473 different trends in H₂O solubility over this differentiation interval (see Wieser et al. 2022c, Fig. 10), with
1474 none predicting an increase as large as that observed here (Fig. S3). Instead, this relationship between
1475 SiO₂ and H₂O is more indicative of differentiation in the presence of an exsolved fluid which is relatively
1476 CO₂-rich, meaning that CO₂ initially dominates the vapour phase, so H₂O behaves relatively
1477 incompatibly during fractional crystallization (Wieser et al., 2022c). This is supported by calculated X_{H₂O}
1478 values for Cascade mafic melt inclusions (Supporting Fig. S10), which indicate that the exsolved fluid
1479 is dominated by CO₂, particularly for melt inclusions where the vapour bubble is accounted for. This is
1480 not consistent with the model inferred by Rasmussen et al. (2022), which assumes the volatile system
1481 is dominated by a H₂O-rich vapour phase at the point of magma stalling.

1482 Thus, we suggest based on our compilation that it is more likely that a crustal process operating along
1483 the entire arc (whether due to a rheological boundary, or density-controlled) is restricting storage of all
1484 but the most mafic magmas to the upper 0–5 kbar of the crust (Chaussard and Amelung, 2014; Huber
1485 et al., 2019). Our compilation does show hints of deeper crustal magma storage, likely of more mafic
1486 magmas. However, due to the very nature of magma differentiation itself, crystals from the mafic
1487 predecessors to the more evolved erupted liquids are poorly preserved, meaning deeper magma
1488 storage is easily obscured. This preservation bias is particularly hard to see through given the small
1489 number of published mineral compositions at many Cascade volcanoes (e.g., N=18 Cpx from Glacier
1490 Peak, N=16 Amp from Mount Rainier, N=11 Cpx from Three Sisters). If we imagine that 1% of deeper
1491 formed crystals are erupted, we would need thousands of analyses to get a cluster of deeper pressures
1492 that we would be able to interpret with confidence, rather than appearing as outliers. Petrologic
1493 experiments on predecessor mafic magmas erupted at the periphery of Mount Shasta and Mount Rainier
1494 do support a period of mid- to lower-crustal storage that results in crystallization (e.g., Krawczynski et
1495 al., 2012) and/or crustal melting (e.g., Blatter et al., 2017, 2013), which is likely important to evolve
1496 mantle-derived magmas to the intermediate and silicic compositions characteristic of those stored in
1497 the upper crust. Future MI work measuring both the melt and vapour bubble, petrologic experiments,
1498 and substantially more mineral analyses are thus required to further investigate the prevalence of
1499 deeper storage of mafic melts in the Cascades arc relative to the ubiquitous upper crustal reservoirs
1500 recorded by the compiled geophysical studies and available mineral data.

1501 Conclusions

1502 A detailed review of available petrological, geochemical and geophysical constraints on the depth of
1503 magma storage beneath Cascade arc volcanoes suggest that the majority of magma storage is
1504 restricted to the upper 0–5 kbar (0–20 km) of the crust, and at reasonably constant depth along strike.
1505 However, further consideration of magma storage at higher resolution, and evaluation of latitudinal
1506 variations is limited by issues with accuracy and by high uncertainties of techniques used for estimating
1507 storage pressure, and by numerous data gaps that exist along the arc. Considering the number of high-
1508 threat volcanoes in the Cascades, the paucity of data to constrain magma storage from geochemical
1509 and geophysical perspectives is highly concerning, and a stark contrast to other high-threat volcanoes
1510 in the US (e.g., Kilauea, Poland et al., 2014).

1511 Gaps in geophysical datasets result from: 1) difficult access because of terrain, snow and ice cover, 2)
1512 the fact many Cascade volcanoes have been relatively quiescent in the last few decades, 3) dense
1513 geophysical imaging campaigns are costly and uncommon, and 4) permitting issues in wilderness areas
1514 hindering the establishment of dense monitoring networks (Moran and Benjamin, 2021; Poland et al.,

1515 2017). Gaps in geochemical and petrological datasets reflect a lack of study of many important systems,
1516 specific technique limitations (e.g., neglecting CO₂ vapour bubbles, poor quality EPMA analyses of
1517 mineral compositions, Wieser et al., 2023b), and poor data reporting (e.g., publishing only
1518 representative mineral analyses). We therefore recommend targeted melt inclusion, petrologic,
1519 experimental and further geophysical studies of the understudied high threat volcanoes in the Cascades
1520 arc to determine their depths of magma storage, which are critical for interpreting future monitoring
1521 signals and will influence the style, size, and frequency of future eruptions.

1522 Acknowledgements

1523 The authors acknowledge support from a National Science Foundation Grants 1948862 and 1850779
1524 (to AJRK), 1949173 (to CBT), and 1948834 (to GAA). We also acknowledge support from the National
1525 Science Foundation ICER-20–26904 granted to OFM Research (PI. Ghiorso) for maintaining the ENKI
1526 server used to perform saturation pressure calculations using VEScal. This study relies heavily on data
1527 provided by corresponding authors, many of whom went to considerable effort to track down decade-
1528 old data. We thank Martin Streck for help extracting mineral compositions from his online textural tool,
1529 Judy Fierstein for sharing a large quantity of mineral data from Mount Adams, Nicole Moore for sharing
1530 mineral data from Mt Baker, Allison Koleszar for sharing amphibole data from Mt Hood, Warner Cribb
1531 for sharing pdf tables of mineral data from his thesis on Mount Hood, Heather Wright for sharing mineral
1532 data from Crater Lake, Thomas Sisson for sharing data from Rainier, Kristina Walowski and Melissa
1533 Scruggs for help reconstructing their Cpx-Liq datasets, Michael Clynne and Bryan Platt for sharing large
1534 amounts of data from Brokeoff Volcano, and Tim Druitt and Charlie Bacon for posting large quantities
1535 of handwritten EPMA data from Crater Lake. We thank Ellen Aster for help interpreting her vapour
1536 bubble data from Lassen. We thank Matthew Gleeson for sending many journal pdfs which were behind
1537 paywalls. We thank Nick Barber for his VMSG QGIS course, which we used to help extract topographic
1538 profiles of the Cascades. We are extremely grateful to Julie Donnelly-Nolan, Mellisa Scruggs, and Paul
1539 Segall for exceptionally thorough reviews that helped us track down some missing studies, and greatly
1540 improved the flow of the draft, and Paul Asimow for editorial handling. Throughout this paper, the post-
1541 colonial names are used for Cascade volcanic centres. We acknowledge that Indigenous cultures of
1542 the region have names for these volcanoes, and we hope that one day the official names of these
1543 volcanoes reflect these names.

1544 Open Research

1545 A compiled dataset of mineral compositions, melt inclusions and seismic stations, along with the Jupyter
1546 Notebooks used to compile, filter and plot data are available on Penny Wieser's GitHub
1547 (https://github.com/PennyWieser/Cascade_data_Compilation/tree/main). Upon article acceptance, this
1548 will be archived on Zenodo.

1549 References

- 1550 Abers, G.A., Hacker, B.R., 2016. A MATLAB toolbox and Excel workbook for calculating the densities,
1551 seismic wave speeds, and major element composition of minerals and rocks at pressure and
1552 temperature. *Geochem. Geophys. Geosyst.* 17, 616–624.
1553 <https://doi.org/10.1002/2015GC006171>
- 1554 Achauer, U., Evans, J.R., Stauber, D.A., 1988. High-resolution seismic tomography of compressional
1555 wave velocity structure at Newberry Volcano, Oregon Cascade Range. *J. Geophys. Res.* 93,
1556 10135–10147. <https://doi.org/10.1029/JB093iB09p10135>
- 1557 Anderson, A.T., 1974. Evidence for a Picritic, Volatile-rich Magma beneath Mt. Shasta, California.
1558 *Journal of Petrology* 15, 243–267.
- 1559 Anderson, K., Segall, P., 2013. Bayesian inversion of data from effusive volcanic eruptions using
1560 physics-based models: Application to Mount St. Helens 2004–2008. *J. Geophys. Res. Solid*
1561 *Earth* 118, 2017–2037. <https://doi.org/10.1002/jgrb.50169>
- 1562 Applegarth, L.J., Tuffen, H., James, M.R., Pinkerton, H., Cashman, K.V., 2013. Direct observations of
1563 degassing-induced crystallization in basalts. *Geology* 41, 243–246.
1564 <https://doi.org/10.1130/G33641.1>

- 1565 Aster, E.M., Wallace, P.J., Moore, L.R., Watkins, J., Gazel, E., Bodnar, R.J., 2016. Reconstructing CO₂
1566 concentrations in basaltic melt inclusions using Raman analysis of vapor bubbles. *Journal of*
1567 *Volcanology and Geothermal Research* 323, 148–162.
1568 <https://doi.org/10.1016/j.jvolgeores.2016.04.028>
- 1569 Bacon, C.R., Lanphere, M.A., 2006. Eruptive history and geochronology of Mount Mazama and the
1570 Crater Lake region, Oregon. *Geological Society of America Bulletin* 118, 1331–1359.
1571 <https://doi.org/10.1130/B25906.1>
- 1572 Bacon, C.R., Newman, S., Stolper, E., 1992. Water, CO₂, Cl, and F in melt inclusions in phenocrysts
1573 from three Holocene explosive eruptions, Crater Lake, Oregon. *American Mineralogist* 77,
1574 1021–1030.
- 1575 Baggerman, T.D., DeBari, S.M., 2011. The generation of a diverse suite of Late Pleistocene and
1576 Holocene basalt through dacite lavas from the northern Cascade arc at Mount Baker,
1577 Washington. *Contrib Mineral Petrol* 161, 75–99. <https://doi.org/10.1007/s00410-010-0522-2>
- 1578 Baker, M.B., Grove, T.L., Price, R., 1994. Primitive basalts and andesites from the Mt. Shasta region,
1579 N. California: products of varying melt fraction and water content. *Contr. Mineral. and*
1580 *Petrol.* 118, 111–129. <https://doi.org/10.1007/BF01052863>
- 1581 Barker, S.E., Malone, S.D., 1991. Magmatic system geometry at Mount St. Helens modeled from the
1582 stress field associated with post-eruptive earthquakes. *J. Geophys. Res.* 96, 11883.
1583 <https://doi.org/10.1029/91JB00430>
- 1584 Barr, J., Grove, T.L., Elkins-Tanton, L., 2007. High-magnesian andesite from Mount Shasta: A product
1585 of magma mixing and contamination, not a primitive melt: Comment and Reply: Comment.
1586 *Geology* 35, e147–e147.
- 1587 Bartels, K.S., Kinzler, R.J., Grove, T.L., 1991. High pressure phase relations of primitive high-alumina
1588 basalts from Medicine Lake volcano, northern California. *Contr. Mineral. and Petrol.* 108,
1589 253–270. <https://doi.org/10.1007/BF00285935>
- 1590 Beachly, M.W., Hooft, E.E.E., Toomey, D.R., Waite, G.P., 2012. Upper crustal structure of Newberry
1591 Volcano from P-wave tomography and finite difference waveform modeling: NEWBERRY
1592 FINITE DIFFERENCE MODELING. *J. Geophys. Res.* 117.
1593 <https://doi.org/10.1029/2012JB009458>
- 1594 Bedrosian, P.A., Peacock, J.R., Bowles-Martinez, E., Schultz, A., Hill, G.J., 2018. Crustal inheritance
1595 and a top-down control on arc magmatism at Mount St Helens. *Nature Geosci* 11, 865–870.
1596 <https://doi.org/10.1038/s41561-018-0217-2>
- 1597 Benz, H.M., Zandt, G., Oppenheimer, D.H., 1992. Lithospheric structure of northern California from
1598 teleseismic images of the upper mantle. *J. Geophys. Res.* 97, 4791.
1599 <https://doi.org/10.1029/92JB00067>
- 1600 Blatter, D.L., Sisson, T.W., Hankins, W.B., 2017. Voluminous arc dacites as amphibole reaction-
1601 boundary liquids. *Contrib Mineral Petrol* 172, 27. [https://doi.org/10.1007/s00410-017-1340-](https://doi.org/10.1007/s00410-017-1340-6)
1602 [6](https://doi.org/10.1007/s00410-017-1340-6)
- 1603 Blatter, D.L., Sisson, T.W., Hankins, W.B., 2013. Crystallization of oxidized, moderately hydrous arc
1604 basalt at mid- to lower-crustal pressures: implications for andesite genesis. *Contrib Mineral*
1605 *Petrol* 166, 861–886. <https://doi.org/10.1007/s00410-013-0920-3>
- 1606 Blundy, J., 2022. Chemical Differentiation by Mineralogical Buffering in Crustal Hot Zones. *Journal of*
1607 *Petrology* 63, egac054. <https://doi.org/10.1093/petrology/egac054>
- 1608 Blundy, J., Cashman, K., 2005. Rapid decompression-driven crystallization recorded by melt
1609 inclusions from Mount St. Helens volcano. *Geol* 33, 793. <https://doi.org/10.1130/G21668.1>
- 1610 Blundy, J., Cashman, K.V., Rust, A., Witham, F., 2010. A case for CO₂-rich arc magmas. *Earth and*
1611 *Planetary Science Letters* 290, 289–301. <https://doi.org/10.1016/j.epsl.2009.12.013>
- 1612 Bonner, R., 2015. A magnetotelluric investigation of shallow conductivity sources beneath the
1613 Cascadia Volcanic Arc. Honors Thesis, Oregon State University.

- 1614 Bowles-Martinez, E., Schultz, A., 2020. Composition of Magma and Characteristics of the
 1615 Hydrothermal System of Newberry Volcano, Oregon, From Magnetotellurics. *Geochem.*
 1616 *Geophys. Geosyst.* 21. <https://doi.org/10.1029/2019GC008831>
- 1617 Bullen, T.D., Clynne, M.A., 1990. Trace element and isotopic constraints on magmatic evolution at
 1618 Lassen Volcanic Center. *J. Geophys. Res.* 95, 19671.
 1619 <https://doi.org/10.1029/JB095iB12p19671>
- 1620 Cashman, K.V., Sparks, R.S.J., Blundy, J.D., 2017. Vertically extensive and unstable magmatic systems:
 1621 A unified view of igneous processes. *Science* 355, eaag3055.
 1622 <https://doi.org/10.1126/science.aag3055>
- 1623 Chaussard, E., Amelung, F., 2014. Regional controls on magma ascent and storage in volcanic arcs.
 1624 *Geochem. Geophys. Geosyst.* 15, 1407–1418. <https://doi.org/10.1002/2013GC005216>
- 1625 Chiarabba, C., Amato, A., Evans, J., 1995. Variations on the NeHT high-resolution tomography
 1626 method: A test of technique and results for Medicine Lake Volcano, northern California.
 1627 *Journal of Geophysical Research B3*, 4035–4052.
- 1628 Christiansen, R., Calvert, A., Champion, D., 2013. Voluminous tholeiitic basalts near Mount Shasta,
 1629 California, as regional strain markers. Presented at the AGU Fall Meeting Abstracts, pp.
 1630 V11D-03.
- 1631 Christiansen, R.L., Calvert, A.T., Champion, D.E., Gardner, C.A., Fierstein, J.E., Vazquez, J.A., 2020. The
 1632 remarkable volcanism of Shastina, a stratocone segment of Mount Shasta, California.
 1633 *Geosphere* 16, 1153–1178. <https://doi.org/10.1130/GES02080.1>
- 1634 Christiansen, R.L., Calvert, A.T., Grove, T.L., 2017. *Geologic Field-Trip Guide to Mount Shasta*
 1635 *Volcano, Northern California.*
- 1636 Clynne, M.A., 1999. A Complex Magma Mixing Origin for Rocks Erupted in 1915, Lassen Peak,
 1637 California. *Journal of Petrology* 40, 105–132. <https://doi.org/10.1093/petroj/40.1.105>
- 1638 Clynne, M.A., Christiansen, R.L., Trimble, D.A., McGeehin, J.P., 2008. Radiocarbon dates from
 1639 volcanic deposits of the Chaos Crags and Cinder Cone eruptive sequences and other
 1640 deposits, Lassen Volcanic National Park and vicinity, California. U.S. Geological Survey Open-
 1641 File Report 02-290.
- 1642 Clynne, M.A., Muffler, L., 2010. *Geologic Map of Lassen Volcanic National Park and Vicinity,*
 1643 *California.* U.S. Geological Survey Scientific Investigations Map 2899.
- 1644 Conrey, R., 1991. *Geology and petrology of the Mt. Jefferson area, High Cascade range, Oregon.* PhD
 1645 Thesis Washington State University.
- 1646 Cooper, K.M., Reid, M.R., 2003. Re-examination of crystal ages in recent Mount St. Helens lavas:
 1647 implications for magma reservoir processes. *Earth and Planetary Science Letters* 213, 149–
 1648 167. [https://doi.org/10.1016/S0012-821X\(03\)00262-0](https://doi.org/10.1016/S0012-821X(03)00262-0)
- 1649 Couperthwaite, F.K., Wieser, P.E., Kent, A.J.R., Ruth, D.C.S., Gazel, E., DeVitre, C.L., 2022. Combining
 1650 Fe-Mg diffusion in olivine and volatile concentrations from olivine-hosted melt inclusions to
 1651 constrain eruption timescales and magma storage depths beneath Paint Pot Crater,
 1652 Medicine Lake. Presented at the Chapman Conference on Distributed Volcanism.
- 1653 Cribb, J.W., 1997. *A Petrologic and Geochemical Investigation of the Evolutionary History of Calc-
 1654 alkaline Magmas, Mount Hood, Oregon.* Ohio State University PhD thesis.
- 1655 Crider, J.G., Frank, D., Malone, S.D., Poland, M.P., Werner, C., Caplan-Auerbach, J., 2011. Magma at
 1656 depth: a retrospective analysis of the 1975 unrest at Mount Baker, Washington, USA. *Bull*
 1657 *Volcanol* 73, 175–189. <https://doi.org/10.1007/s00445-010-0441-0>
- 1658 Crosbie, K.J., Abers, G.A., Mann, M.E., Janiszewski, H.A., Creager, K.C., Ulberg, C.W., Moran, S.C.,
 1659 2019. Shear Velocity Structure From Ambient Noise and Teleseismic Surface Wave
 1660 Tomography in the Cascades Around Mount St. Helens. *J. Geophys. Res. Solid Earth* 124,
 1661 8358–8375. <https://doi.org/10.1029/2019JB017836>
- 1662 Danyushevsky, L.V., Plechov, P., 2011. Petrolog3: Integrated software for modeling crystallization
 1663 processes. *Geochemistry, Geophysics, Geosystems* 12, n/a-n/a.
 1664 <https://doi.org/10.1029/2011GC003516>

- 1665 Darr, C., 2006. Magma Chamber Processes Over the Past 475,000 Years at Mount Hood, Oregon:
1666 Insights From Crystal Zoning and Crystal Size Distribution Studies. Oregon State University
1667 Masters Thesis.
- 1668 Das, T., Nolet, G., 1998. Crustal thickness map of the western United States by partitioned waveform
1669 inversion. *J. Geophys. Res.* 103, 30021–30038. <https://doi.org/10.1029/98JB01119>
- 1670 DeVitre, C.L., Allison, C.M., Gazel, E., 2021. A high-precision CO₂ densimeter for Raman spectroscopy
1671 using a Fluid Density Calibration Apparatus. *Chemical Geology* 584, 120522.
1672 <https://doi.org/10.1016/j.chemgeo.2021.120522>
- 1673 DeVitre, C.L., Dayton, K., Gazel, E., Pamukçu, A., Gaetani, G., Wieser, P.E., 2023. Laser heating effect
1674 on Raman analysis of CO₂ co-existing as liquid and vapor in olivine-hosted melt inclusion
1675 bubbles. *Volcanica* 6, 201–219. <https://doi.org/10.30909/vol.06.02.201219>
- 1676 DiGuilio, J., 2015. Reconstructing the Physical Record of a Four-Million-Year Volcanic System:
1677 Geochemistry, Thermobarometry, and Geologic Map of the Mount Jefferson Area, Oregon.
1678 Oregon State University Masters Thesis.
- 1679 Dixon, J.E., 1997. Degassing of alkalic basalts. *American Mineralogist* 82, 368–378.
1680 <https://doi.org/10.2138/am-1997-3-415>
- 1681 Donnelly-Nolan, J.M., 2008. Chemical analyses of pre-Holocene rocks from Medicine Lake Volcano
1682 and vicinity, northern California. U.S. Geol. Surv. Open-File Rept. 2008-1094.
- 1683 Donnelly-Nolan, J.M., Grove, T.L., Lanphere, M.A., Champion, D.E., Ramsey, D.W., 2008. Eruptive
1684 history and tectonic setting of Medicine Lake Volcano, a large rear-arc volcano in the
1685 southern Cascades. *Journal of Volcanology and Geothermal Research* 177, 313–328.
1686 <https://doi.org/10.1016/j.jvolgeores.2008.04.023>
- 1687 Donnelly-Nolan, Stovall, W.K., Ramsey, D.W., Ewert, J., Jensen, R., 2011. Newberry Volcano—central
1688 Oregon’s sleeping giant. USGS Fact Sheet 2011-3145.
- 1689 Druitt, T.H., Bacon, C.R., 1989. Petrology of the zoned calcalkaline magma chamber of Mount
1690 Mazama, Crater Lake, Oregon. *Contr. Mineral. and Petrol.* 101, 245–259.
1691 <https://doi.org/10.1007/BF00375310>
- 1692 Ducea, M.N., Saleeby, J.B., Bergantz, G., 2015. The Architecture, Chemistry, and Evolution of
1693 Continental Magmatic Arcs. *Annu. Rev. Earth Planet. Sci.* 43, 299–331.
1694 <https://doi.org/10.1146/annurev-earth-060614-105049>
- 1695 Dufek, J., Cashman, K., Hooft, E., Bedrosian, P., 2022. The Nature of Active Magma Reservoirs and
1696 Storage Underneath Cascade Volcanoes. *Elements* 18, 239–245.
1697 <https://doi.org/10.2138/gselements.18.4.239>
- 1698 Dzurisin, D., 1999. Results of repeated leveling surveys at Newberry Volcano, Oregon, and near
1699 Lassen Peak Volcano, California. *Bulletin of Volcanology* 61, 83–91.
1700 <https://doi.org/10.1007/s004450050264>
- 1701 Dzurisin, D., Donnelly-Nolan, J.M., Evans, J.R., Walter, S.R., 1991. Crustal subsidence, seismicity, and
1702 structure near Medicine Lake Volcano, California. *J. Geophys. Res.* 96, 16319.
1703 <https://doi.org/10.1029/91JB01452>
- 1704 Dzurisin, D., Lisowski, M., Wicks, C.W., 2009. Continuing inflation at Three Sisters volcanic center,
1705 central Oregon Cascade Range, USA, from GPS, leveling, and InSAR observations. *Bull*
1706 *Volcanol* 71, 1091–1110. <https://doi.org/10.1007/s00445-009-0296-4>
- 1707 Dzurisin, D., Lisowski, M., Wicks, C.W., Poland, M.P., Endo, E.T., 2006. Geodetic observations and
1708 modeling of magmatic inflation at the Three Sisters volcanic center, central Oregon Cascade
1709 Range, USA. *Journal of Volcanology and Geothermal Research* 150, 35–54.
1710 <https://doi.org/10.1016/j.jvolgeores.2005.07.011>
- 1711 Dzurisin, D., Poland, M.P., Bürgmann, R., 2002. Steady subsidence of Medicine Lake volcano,
1712 northern California, revealed by repeated leveling surveys. *J. Geophys. Res.* 107, ECV 8-1-
1713 ECV 8-16. <https://doi.org/10.1029/2001JB000893>

- 1714 Evans, J.R., Zucca, J.J., 1988. Active high-resolution seismic tomography of compressional wave
 1715 velocity and attenuation structure at Medicine Lake Volcano, Northern California Cascade
 1716 Range. *J. Geophys. Res.* 93, 15016–15036. <https://doi.org/10.1029/JB093iB12p15016>
- 1717 Evans, W.C., van Soest, M.C., Mariner, R.H., Hurwitz, S., Ingebritsen, S.E., Wicks, C.W., Schmidt, M.E.,
 1718 2004. Magmatic intrusion west of Three Sisters, central Oregon, USA: The perspective from
 1719 spring geochemistry. *Geol* 32, 69. <https://doi.org/10.1130/G19974.1>
- 1720 Ewert, J., Diefenbach, A.K., Ramsey, D.W., 2018. 2018 update to the U.S. Geological Survey national
 1721 volcanic threat assessment (Scientific Investigations Report 2018-5140), Scientific
 1722 Investigations Report.
- 1723 Fierstein, J., Hildreth, W., Calvert, A.T., 2011. Eruptive history of South Sister, Oregon Cascades.
 1724 *Journal of Volcanology and Geothermal Research* 207, 145–179.
 1725 <https://doi.org/10.1016/j.jvolgeores.2011.06.003>
- 1726 Fillmore, J.A., 2014. The Origin of Adakites in the Garibaldi Volcanic Complex, southwestern British
 1727 Columbia, Canada. Master of Science, University of Regina.
- 1728 Flinders, A.F., Shen, Y., 2017. Seismic evidence for a possible deep crustal hot zone beneath
 1729 Southwest Washington. *Sci Rep* 7, 7400. <https://doi.org/10.1038/s41598-017-07123-w>
- 1730 Gerlach, D.C., Grove, T.L., 1982. Petrology of Medicine Lake Highland volcanics: Characterization of
 1731 endmembers of magma mixing. *Contr. Mineral. and Petrol.* 80, 147–159.
 1732 <https://doi.org/10.1007/BF00374892>
- 1733 Geschwind, C.-H., Rutherford, M.J., 1992. Cummingtonite and the evolution of the Mount St. Helens
 1734 (Washington) magma system: an experimental study. *Geology* 20, 1011–1014.
- 1735 Ghiorso, M.S., Gualda, G.A.R., 2015. An H₂O–CO₂ mixed fluid saturation model compatible with
 1736 rhyolite-MELTS. *Contrib Mineral Petrol* 169, 53. <https://doi.org/10.1007/s00410-015-1141-8>
- 1737 Gleeson, M.L.M., Gibson, S.A., Stock, M.J., 2021. Upper Mantle Mush Zones beneath Low Melt Flux
 1738 Ocean Island Volcanoes: Insights from Isla Floreana, Galápagos. *Journal of Petrology* 61,
 1739 egaa094. <https://doi.org/10.1093/petrology/egaa094>
- 1740 Gross, J., 2012. Felsic magmas from Mt. Baker in the northern Cascade arc: Origin and role in
 1741 andesite production, Western Washington University Masters Thesis,
 1742 <https://cedar.wwwu.edu/wwuet/239/>. ed.
- 1743 Grove, T., Parman, S., Bowring, S., Price, R., Baker, M., 2002. The role of an H₂O-rich fluid
 1744 component in the generation of primitive basaltic andesites and andesites from the Mt.
 1745 Shasta region, N California. *Contrib Mineral Petrol* 142, 375–396.
 1746 <https://doi.org/10.1007/s004100100299>
- 1747 Grove, T.L., Baker, M.B., Price, R.C., Parman, S.W., Elkins-Tanton, L.T., Chatterjee, N., Montener, O.,
 1748 2005. Magnesian andesite and dacite lavas from Mt. Shasta, northern California: products of
 1749 fractional crystallization of H₂O-rich mantle melts. *Contrib Mineral Petrol* 148, 542–565.
 1750 <https://doi.org/10.1007/s00410-004-0619-6>
- 1751 Grove, T.L., Donnelly-Nolan, J.M., 1986. The evolution of young silicic lavas at Medicine Lake
 1752 Volcano, California: Implications for the origin of compositional gaps in calc-alkaline series
 1753 lavas. *Contr. Mineral. and Petrol.* 92, 281–302. <https://doi.org/10.1007/BF00572157>
- 1754 Grove, T.L., Donnelly-Nolan, J.M., Housh, T., 1997. Magmatic processes that generated the rhyolite
 1755 of Glass Mountain, Medicine Lake volcano, N. California. *Contributions to Mineralogy and
 1756 Petrology* 127, 205–223. <https://doi.org/10.1007/s004100050276>
- 1757 Grove, T.L., Elkins-Tanton, L.T., Parman, S.W., Chatterjee, N., Montener, O., Gaetani, G.A., 2003.
 1758 Fractional crystallization and mantle-melting controls on calc-alkaline differentiation trends.
 1759 *Contributions to Mineralogy and Petrology* 145, 515–533. <https://doi.org/10.1007/s00410-003-0448-z>
- 1760
- 1761 Grove, T.L., Gerlach, D.C., Sando, T.W., 1982. Origin of calc-alkaline series lavas at Medicine Lake
 1762 Volcano by fractionation, assimilation and mixing. *Contr. Mineral. and Petrol.* 80, 160–182.
 1763 <https://doi.org/10.1007/BF00374893>

- 1764 Grove, T.L., Kinzler, R.J., Baker, M.B., Donnelly-Nolan, J.M., Leshner, C.E., 1988. Assimilation of granite
 1765 by basaltic magma at Burnt Lava flow, Medicine Lake volcano, northern California:
 1766 Decoupling of heat and mass transfer. *Contr. Mineral. and Petrol.* 99, 320–343.
 1767 <https://doi.org/10.1007/BF00375365>
- 1768 Gualda, G.A.R., Ghiorsio, M.S., Lemons, R.V., Carley, T.L., 2012. Rhyolite-MELTS: a Modified
 1769 Calibration of MELTS Optimized for Silica-rich, Fluid-bearing Magmatic Systems. *Journal of*
 1770 *Petrology* 53, 875–890. <https://doi.org/10.1093/petrology/egr080>
- 1771 Guffanti, M., Weaver, C.S., 1988. Distribution of Late Cenozoic volcanic vents in the Cascade range:
 1772 Volcanic arc segmentation and regional tectonic considerations. *J. Geophys. Res.* 93, 6513.
 1773 <https://doi.org/10.1029/JB093iB06p06513>
- 1774 Harris, R.A., Iyer, H.M., Dawson, P.B., 1991. Imaging the Juan de Fuca Plate beneath southern
 1775 Oregon using teleseismic *P* wave residuals. *J. Geophys. Res.* 96, 19879–19889.
 1776 <https://doi.org/10.1029/91JB02046>
- 1777 Heath, B.A., Hooft, E.E.E., Toomey, D.R., 2018. Autocorrelation of the Seismic Wavefield at Newberry
 1778 Volcano: Reflections From the Magmatic and Geothermal Systems. *Geophys. Res. Lett.* 45,
 1779 2311–2318. <https://doi.org/10.1002/2017GL076706>
- 1780 Heath, B.A., Hooft, E.E.E., Toomey, D.R., Bezada, M.J., 2015. Imaging the magmatic system of N
 1781 ewberry V olcano using joint active source and teleseismic tomography. *Geochem. Geophys.*
 1782 *Geosyst.* 16, 4433–4448. <https://doi.org/10.1002/2015GC006129>
- 1783 Heiken, G., 1978. Plinian-type eruptions in the medicine lake highland, california, and the nature of
 1784 the underlying magma. *Journal of Volcanology and Geothermal Research* 4, 375–402.
 1785 [https://doi.org/10.1016/0377-0273\(78\)90023-9](https://doi.org/10.1016/0377-0273(78)90023-9)
- 1786 Hildreth, W., 2007. Quaternary magmatism in the Cascades- Geological Perspectives, USGS
 1787 Professional paper 1744.
- 1788 Hildreth, W., Fierstein, J., 2015. Geologic map of the Simcoe Mountains Volcanic Field, main central
 1789 segment, Yakama Nation, Washington (Scientific Investigations Map 3315), Scientific
 1790 Investigations Map.
- 1791 Hildreth, W., Fierstein, J., 1997. Recent eruptions of Mount Adams, Washington Cascades, USA.
 1792 *Bulletin of Volcanology* 58, 472–490. <https://doi.org/10.1007/s004450050156>
- 1793 Hildreth, W., Fierstein, J., Calvert, A.T., Robinson, J.E., Lindquist, T.A., Nimz, K., 2012. Geologic map
 1794 of three sisters volcanic cluster, cascade range, Oregon. Pamphlet to accompany Scientific
 1795 Investigations Map 3186, US Geological Survey.
- 1796 Hildreth, W., Fierstein, J., Lanphere, M., 2003. Eruptive history and geochronology of the Mount
 1797 Baker volcanic field, Washington. *Geological Society of America Bulletin* 115, 729–764.
 1798 [https://doi.org/10.1130/0016-7606\(2003\)115<0729:EHAGOT>2.0.CO;2](https://doi.org/10.1130/0016-7606(2003)115<0729:EHAGOT>2.0.CO;2)
- 1799 Hill, G.J., Caldwell, T.G., Heise, W., Chertkoff, D.G., Bibby, H.M., Burgess, M.K., Cull, J.P., Cas, R.A.F.,
 1800 2009. Distribution of melt beneath Mount St Helens and Mount Adams inferred from
 1801 magnetotelluric data. *Nature Geosci* 2, 785–789. <https://doi.org/10.1038/ngeo661>
- 1802 Hilley, G., Brodsky, E., Roman, D., Shillington, D., Tobin, H., 2022. SZ4D Implementation Plan.
 1803 Stanford Digital Repository. <https://doi.org/10.25740/HY589FC7561>
- 1804 Hodge, B.E., Crider, J.G., 2010. Investigating mechanisms of edifice deflation, 1981–2007, at Mount
 1805 Baker volcano, Washington, United States. *J. Geophys. Res.* 115, B04401.
 1806 <https://doi.org/10.1029/2009JB006730>
- 1807 Hollyday, A.E., Leiter, S.H., Walowski, K.J., 2020. Pre-eruptive storage, evolution, and ascent
 1808 timescales of a high-Mg basaltic andesite in the southern Cascade Arc. *Contrib Mineral*
 1809 *Petrol* 175, 88. <https://doi.org/10.1007/s00410-020-01730-z>
- 1810 Huber, C., Townsend, M., Degruyter, W., Bachmann, O., 2019. Optimal depth of subvolcanic magma
 1811 chamber growth controlled by volatiles and crust rheology. *Nat. Geosci.* 12, 762–768.
 1812 <https://doi.org/10.1038/s41561-019-0415-6>

- 1813 Hughes, E.C., Buse, B., Kearns, S.L., Blundy, J.D., Kilgour, G., Mader, H.M., 2019. Low analytical totals
 1814 in EPMA of hydrous silicate glass due to sub-surface charging: Obtaining accurate volatiles by
 1815 difference. *Chemical Geology* 505, 48–56. <https://doi.org/10.1016/j.chemgeo.2018.11.015>
- 1816 Humphreys, M.C.S., Cooper, G.F., Zhang, J., Loewen, M., Kent, A.J.R., Macpherson, C.G., Davidson,
 1817 J.P., 2019. Unravelling the complexity of magma plumbing at Mount St. Helens: a new trace
 1818 element partitioning scheme for amphibole. *Contrib Mineral Petrol* 174, 9.
 1819 <https://doi.org/10.1007/s00410-018-1543-5>
- 1820 Iacono-Marziano, G., Morizet, Y., Le Trong, E., Gaillard, F., 2012. New experimental data and semi-
 1821 empirical parameterization of H₂O–CO₂ solubility in mafic melts. *Geochimica et*
 1822 *Cosmochimica Acta* 97, 1–23. <https://doi.org/10.1016/j.gca.2012.08.035>
- 1823 Iacovino, K., Matthews, S., Wieser, P.E., Moore, G., Begue, F., 2021. VESlcal Part I: An open-source
 1824 thermodynamic model engine for mixed volatile (H₂O–CO₂) solubility in silicate melt. *Earth*
 1825 *and Space Science*. <https://doi.org/10.1029/2020EA001584>
- 1826 Jiang, C., Schmandt, B., Abers, G.A., Kiser, E., Miller, M.S., 2023. Segmentation and radial anisotropy
 1827 of the deep crustal magmatic system beneath the Cascades arc. *Geochemistry, Geophysics,*
 1828 *Geosystems*. <https://doi.org/10.1002/essoar.10512621.1>
- 1829 Johnson, E.R., Cashman, K.V., 2020. Understanding the storage conditions and fluctuating eruption
 1830 style of a young monogenetic volcano: Blue Lake crater (<3 ka), High Cascades, Oregon.
 1831 *Journal of Volcanology and Geothermal Research* 408, 107103.
 1832 <https://doi.org/10.1016/j.jvolgeores.2020.107103>
- 1833 Jones, J., Malone, S.D., 2005. Mount Hood Earthquake Activity: Volcanic or Tectonic Origins? *Bulletin*
 1834 *of the Seismological Society of America* 95, 818–832. <https://doi.org/10.1785/0120040019>
- 1835 Jorgenson, C., Higgins, O., Petrelli, M., Bégué, F., Caricchi, L., 2022. A Machine Learning-Based
 1836 Approach to Clinopyroxene Thermobarometry: Model Optimization and Distribution for Use
 1837 in Earth Sciences. *JGR Solid Earth* 127. <https://doi.org/10.1029/2021JB022904>
- 1838 Keith, T.E., Donnelly-Nolan, J., Markman, J., Beeson, M., 1985. K–Ar ages of rocks in the Mount Hood
 1839 area, Oregon. *Isochron-West* 42, 12–17.
- 1840 Kent, A.J.R., Darr, C., Koleszar, A.M., Salisbury, M.J., Cooper, K.M., 2010. Preferential eruption of
 1841 andesitic magmas through recharge filtering. *Nature Geosci* 3, 631–636.
 1842 <https://doi.org/10.1038/ngeo924>
- 1843 Kinzler, R., 1985. A Field, Petrologic, and Geochemical Study of the Callahan Lava Flow, a Basaltic
 1844 Andesite from Medicine Lake Shield Volcano, California. MSci Thesis, MIT.
- 1845 Kinzler, R.J., Donnelly-Nolan, J.M., Grove, T.L., 2000. Late Holocene hydrous mafic magmatism at the
 1846 Paint Pot Crater and Callahan flows, Medicine Lake Volcano, N. California and the influence
 1847 of H₂O in the generation of silicic magmas. *Contrib Mineral Petrol* 138, 1–16.
 1848 <https://doi.org/10.1007/PL00007657>
- 1849 Kiser, E., Levander, A., Zelt, C., Schmandt, B., Hansen, S., 2018. Focusing of melt near the top of the
 1850 Mount St. Helens (USA) magma reservoir and its relationship to major volcanic eruptions.
 1851 *Geology* 46, 775–778. <https://doi.org/10.1130/G45140.1>
- 1852 Kiser, E., Palomeras, I., Levander, A., Zelt, C., Harder, S., Schmandt, B., Hansen, S., Creager, K.,
 1853 Ulberg, C., 2016. Magma reservoirs from the upper crust to the Moho inferred from high-
 1854 resolution V_p and V_s models beneath Mount St. Helens, Washington State, USA. *Geology* 44,
 1855 411–414. <https://doi.org/10.1130/G37591.1>
- 1856 Koleszar, A.M., 2011. Controls on Eruption Style and Magma Compositions at Mount Hood, Oregon.
 1857 Oregon State University PhD thesis.
- 1858 Koleszar, A.M., Kent, A.J.R., Wallace, P.J., Scott, W.E., 2012. Controls on long-term low explosivity at
 1859 andesitic arc volcanoes: Insights from Mount Hood, Oregon. *Journal of Volcanology and*
 1860 *Geothermal Research* 219–220, 1–14. <https://doi.org/10.1016/j.jvolgeores.2012.01.003>
- 1861 Krawczynski, M.J., Grove, T.L., Behrens, H., 2012. Amphibole stability in primitive arc magmas:
 1862 effects of temperature, H₂O content, and oxygen fugacity. *Contrib Mineral Petrol* 164, 317–
 1863 339. <https://doi.org/10.1007/s00410-012-0740-x>

- 1864 Lamadrid, H.M., Moore, L.R., Moncada, D., Rimstidt, J.D., Burruss, R.C., Bodnar, R.J., 2017.
 1865 Reassessment of the Raman CO₂ densimeter. *Chemical Geology* 450, 210–222.
 1866 <https://doi.org/10.1016/j.chemgeo.2016.12.034>
- 1867 Le Voyer, M., Rose-Koga, E.F., Shimizu, N., Grove, T.L., Schiano, P., 2010. Two Contrasting H₂O-rich
 1868 Components in Primary Melt Inclusions from Mount Shasta. *Journal of Petrology* 51, 1571–
 1869 1595. <https://doi.org/10.1093/petrology/egq030>
- 1870 Lee, C.-T.A., Anderson, D.L., 2015. Continental crust formation at arcs, the arclogite “delamination”
 1871 cycle, and one origin for fertile melting anomalies in the mantle. *Science Bulletin* 60, 1141–
 1872 1156. <https://doi.org/10.1007/s11434-015-0828-6>
- 1873 Lerner, A.H., O’Hara, D., Karlstrom, L., Ebmeier, S.K., Anderson, K.R., Hurwitz, S., 2020. The
 1874 Prevalence and Significance of Offset Magma Reservoirs at Arc Volcanoes. *Geophys. Res.*
 1875 *Let.* 47. <https://doi.org/10.1029/2020GL087856>
- 1876 Linneman, S.R., Myers, J.D., 1990. Magmatic inclusions in the Holocene rhyolites of Newberry
 1877 volcano, central Oregon. *Journal of Geophysical Research: Solid Earth* 95, 17677–17691.
- 1878 Lipman, P.W., Banks, N.G., Rhodes, J.M., 1985. Degassing-induced crystallization of basaltic magma
 1879 and effects on lava rheology. *Nature* 317, 604–607. <https://doi.org/10.1038/317604a0>
- 1880 Lisowski, M., Dzurisin, D., Denlinger, R.P., Iwatsubo, E., 2008. Analysis of GPS-Measured Deformation
 1881 Associated with the 2004–2006 Dome-Building Eruption of Mount St. Helens, Washington,
 1882 in: *A Volcano Rekindled: The Renewed Eruption of Mount St. Helens, 2004–2006*, USGS
 1883 Professional Paper 1750.
- 1884 Loewen, M.W., 2012. Volatile Mobility of Trace Metals in Volcanic Systems. PhD dissertation, Oregon
 1885 State University. 237.
- 1886 Lowenstern, J.B., 2003. Melt inclusions come of age: Volatiles, volcanoes, and sorby’s legacy, in:
 1887 *Developments in Volcanology*. Elsevier, pp. 1–21. [https://doi.org/10.1016/S1871-](https://doi.org/10.1016/S1871-644X(03)80021-9)
 1888 [644X\(03\)80021-9](https://doi.org/10.1016/S1871-644X(03)80021-9)
- 1889 Lu, L., Bostock, M.G., 2022. Deep long-period earthquakes near Mount Meager, British Columbia.
 1890 *Canadian Journal of Earth Sciences* 59, 407–417.
- 1891 Lu, Z., Wicks, C., Dzurisin, D., Thatcher, W., Freymueller, J.T., McNutt, S.R., Mann, D., 2000. Aseismic
 1892 inflation of Westdahl volcano, Alaska, revealed by satellite radar interferometry. *Geophysical*
 1893 *Research Letters* 27, 1567–1570.
- 1894 Magee, C., Stevenson, C.T.E., Ebmeier, S.K., Keir, D., Hammond, J.O.S., Gottsmann, J.H., Whaler, K.A.,
 1895 Schofield, N., Jackson, C.A.-L., Petronis, M.S., O’Driscoll, B., Morgan, J., Cruden, A., Vollgger,
 1896 S.A., Dering, G., Micklethwaite, S., Jackson, M.D., 2018. Magma Plumbing Systems: A
 1897 Geophysical Perspective. *Journal of Petrology* 59, 1217–1251.
 1898 <https://doi.org/10.1093/petrology/egy064>
- 1899 Mandeville, C.W., Webster, J.D., Tappen, C., Taylor, B.E., Timbal, A., Sasaki, A., Hauri, E., Bacon, C.R.,
 1900 2009. Stable isotope and petrologic evidence for open-system degassing during the climactic
 1901 and pre-climactic eruptions of Mt. Mazama, Crater Lake, Oregon. *Geochimica et*
 1902 *Cosmochimica Acta* 73, 2978–3012. <https://doi.org/10.1016/j.gca.2009.01.019>
- 1903 Mandler, B.E., Donnelly-Nolan, J.M., Grove, T.L., 2014. Straddling the tholeiitic/calc-alkaline
 1904 transition: the effects of modest amounts of water on magmatic differentiation at Newberry
 1905 Volcano, Oregon. *Contrib Mineral Petrol* 168, 1066. [https://doi.org/10.1007/s00410-014-](https://doi.org/10.1007/s00410-014-1066-7)
 1906 [1066-7](https://doi.org/10.1007/s00410-014-1066-7)
- 1907 Mastin, L.G., Roeloffs, E., Beeler, N.M., Quick, J.E., 2008. Constraints on the Size, Overpressure, and
 1908 Volatile Content of the Mount St. Helens Magma System from Geodetic and Dome-Growth
 1909 Measurements During the 2004–2006+ Eruption. *A Volcano Rekindled: The Renewed*
 1910 *Eruption of Mount St. Helens, 2004–2006*. U.S. Geological Survey Professional Paper 1750
 1911 461–488.
- 1912 McCrory, P.A., Blair, J.L., Waldhauser, F., Oppenheimer, D.H., 2012. Juan de Fuca slab geometry and
 1913 its relation to Wadati-Benioff zone seismicity: JDF SLAB GEOMETRY AND WBZ SEISMICITY. *J.*
 1914 *Geophys. Res.* 117. <https://doi.org/10.1029/2012JB009407>

- 1915 McGary, R.S., Evans, R.L., Wannamaker, P.E., Elsenbeck, J., Rondenay, S., 2014. Pathway from
 1916 subducting slab to surface for melt and fluids beneath Mount Rainier. *Nature* 511, 338–340.
 1917 <https://doi.org/10.1038/nature13493>
- 1918 Mercer, C.N., Johnston, A.D., 2008. Experimental studies of the P–T–H₂O near-liquidus phase
 1919 relations of basaltic andesite from North Sister Volcano, High Oregon Cascades: constraints
 1920 on lower-crustal mineral assemblages. *Contrib Mineral Petrol* 155, 571–592.
 1921 <https://doi.org/10.1007/s00410-007-0259-8>
- 1922 Mironov, N.L., Tobelko, D.P., Smirnov, S.Z., Portnyagin, M.V., Krasheninnikov, S.P., 2020. Estimation
 1923 of CO₂ Content in the Gas Phase of Melt Inclusions Using Raman Spectroscopy: Case Study
 1924 of Inclusions in Olivine from the Karymsky Volcano (Kamchatka). *Russian Geology and
 1925 Geophysics* 61, 600–610. <https://doi.org/10.15372/RGG2019169>
- 1926 Moore, L.R., Gazel, E., Tuohy, R., Lloyd, A.S., Esposito, R., Steele-MacInnis, M., Hauri, E.H., Wallace,
 1927 P.J., Plank, T., Bodnar, R.J., 2015. Bubbles matter: An assessment of the contribution of
 1928 vapor bubbles to melt inclusion volatile budgets. *American Mineralogist* 100, 806–823.
 1929 <https://doi.org/10.2138/am-2015-5036>
- 1930 Moore, L.R., Mironov, N., Portnyagin, M., Gazel, E., Bodnar, R.J., 2018. Volatile contents of primitive
 1931 bubble-bearing melt inclusions from Klyuchevskoy volcano, Kamchatka: Comparison of
 1932 volatile contents determined by mass-balance versus experimental homogenization. *Journal
 1933 of Volcanology and Geothermal Research* 358, 124–131.
 1934 <https://doi.org/10.1016/j.jvolgeores.2018.03.007>
- 1935 Moore, N.E., DeBari, S.M., 2012. Mafic magmas from Mount Baker in the northern Cascade arc,
 1936 Washington: probes into mantle and crustal processes. *Contrib Mineral Petrol* 163, 521–546.
 1937 <https://doi.org/10.1007/s00410-011-0686-4>
- 1938 Moran, S., Benjamin, P., 2021. Permitting Volcano Monitoring Stations in Wilderness/Restricted
 1939 Areas: A Case Study From Mount Hood, Oregon, in: D138. Presented at the GSA Meeting,
 1940 Portland.
- 1941 Moran, S.C., Lees, J.M., Malone, S.D., 1999. *P* wave crustal velocity structure in the greater Mount
 1942 Rainier area from local earthquake tomography. *J. Geophys. Res.* 104, 10775–10786.
 1943 <https://doi.org/10.1029/1999JB900036>
- 1944 Mordensky, S.P., Wallace, P.J., 2018. Magma storage below Cascades shield volcanoes as inferred
 1945 from melt inclusion data: A comparison of long-lived and short-lived magma plumbing
 1946 systems. *Journal of Volcanology and Geothermal Research* 368, 1–12.
 1947 <https://doi.org/10.1016/j.jvolgeores.2018.10.011>
- 1948 Mullen, E.K., McCallum, I.S., 2014. Origin of Basalts in a Hot Subduction Setting: Petrological and
 1949 Geochemical Insights from Mt. Baker, Northern Cascade Arc. *Journal of Petrology* 55, 241–
 1950 281. <https://doi.org/10.1093/petrology/egt064>
- 1951 Mullineaux, D.R., 1974. Pumice and other pyroclastic deposits in Mount Rainier National Park,
 1952 Washington. US Government Printing Office.
- 1953 Musumeci, C., Gresta, S., Malone, S.D., 2002. Magma system recharge of Mount St. Helens from
 1954 precise relative hypocenter location of microearthquakes: MAGMA RECHARGE OF ST.
 1955 HELENS FROM HYPOCENTERS. *J. Geophys. Res.* 107, ESE 16-1-ESE 16-9.
 1956 <https://doi.org/10.1029/2001JB000629>
- 1957 Nakada, S., Bacon, C.R., Gartner, A.E., 1994. Origin of Phenocrysts and Compositional Diversity in
 1958 Pre-Mazama Rhyodacite Lavas, Crater Lake, Oregon. *Journal of Petrology* 35, 127–162.
 1959 <https://doi.org/10.1093/petrology/35.1.127>
- 1960 NASA/METI/AIST/Japan Space systems And U.S./Japan ASTER Science Team, 2019. ASTER Global
 1961 Digital Elevation Model V003. <https://doi.org/10.5067/ASTER/ASTGTM.003>
- 1962 Neave, D.A., Putirka, K.D., 2017. A new clinopyroxene-liquid barometer, and implications for magma
 1963 storage pressures under Icelandic rift zones. *American Mineralogist* 102, 777–794.
 1964 <https://doi.org/10.2138/am-2017-5968>

- 1965 Nichols, M.L., Malone, S.D., Moran, S.C., Thelen, W.A., Vidale, J.E., 2011. Deep long-period
 1966 earthquakes beneath Washington and Oregon volcanoes. *Journal of Volcanology and*
 1967 *Geothermal Research* 200, 116–128. <https://doi.org/10.1016/j.jvolgeores.2010.12.005>
- 1968 Obrebski, M., Abers, G.A., Foster, A., 2015. Magmatic arc structure around Mount Rainier, WA,
 1969 from the joint inversion of receiver functions and surface wave dispersion. *Geochemistry,*
 1970 *Geophysics, Geosystems* 16, 178–194.
- 1971 O’Hara, D., Karlstrom, L., Ramsey, D.W., 2020. Time-evolving surface and subsurface signatures of
 1972 Quaternary volcanism in the Cascades arc. *Geology* 48, 1088–1093.
 1973 <https://doi.org/10.1130/G47706.1>
- 1974 Pallister, J.S., Clynne, M.A., Wright, H.M., Van Eaton, A.R., Vallance, J.W., Sherrod, D.R., Kokelaar,
 1975 B.P., 2017. Field-trip guide to Mount St. Helens, Washington-An overview of the eruptive
 1976 history and petrology, tephra deposits, 1980 pyroclastic density current deposits, and the
 1977 crater. *Scientific Investigations Report*.
- 1978 Park, S.K., Ostos, L.C., 2013. Constraints from magnetotelluric measurements on magmatic processes
 1979 and upper mantle structure in the vicinity of Lassen volcanic center, northern California.
 1980 *Geosphere* 9, 382–393. <https://doi.org/10.1130/GES00799.1>
- 1981 Parker, A.L., Biggs, J., Lu, Z., 2016. Time-scale and mechanism of subsidence at Lassen Volcanic
 1982 Center, CA, from InSAR. *Journal of Volcanology and Geothermal Research* 320, 117–127.
 1983 <https://doi.org/10.1016/j.jvolgeores.2016.04.013>
- 1984 Parker, A.L., Biggs, J., Lu, Z., 2014. Investigating long-term subsidence at Medicine Lake Volcano, CA,
 1985 using multitemporal InSAR. *Geophysical Journal International* 199, 844–859.
 1986 <https://doi.org/10.1093/gji/ggu304>
- 1987 Parsons, T., Trehu, A.M., Luetgert, J.H., Miller, K., Kilbride, F., Wells, R.E., Fisher, M.A., Flueh, E., ten
 1988 Brink, U.S., Christensen, N.I., 1998. A new view into the Cascadia subduction zone and
 1989 volcanic arc: Implications for earthquake hazards along the Washington margin. *Geol* 26,
 1990 199. [https://doi.org/10.1130/0091-7613\(1998\)026<0199:ANVITC>2.3.CO;2](https://doi.org/10.1130/0091-7613(1998)026<0199:ANVITC>2.3.CO;2)
- 1991 Phillips, M., Till, C.B., 2022. Crustal storage and ascent history of the Mt. Shasta primitive magnesian
 1992 andesite: implications for arc magma crustal flux rates. *Contrib Mineral Petrol* 177, 9.
 1993 <https://doi.org/10.1007/s00410-021-01853-x>
- 1994 Pitcher, B.W., Kent, A.J.R., 2019. Statistics and segmentation: Using Big Data to assess Cascades arc
 1995 compositional variability. *Geochimica et Cosmochimica Acta* 265, 443–467.
 1996 <https://doi.org/10.1016/j.gca.2019.08.035>
- 1997 Pitt, A.M., Hill, D.P., Walter, S.W., Johnson, M.J.S., 2002. Midcrustal, Long-period Earthquakes
 1998 beneath Northern California Volcanic Areas. *Seismological Research Letters* 73, 144–152.
- 1999 Platt, B., 2020. Constraining Internal Eruption Trigger Mechanisms for Flows at Brokeoff Volcano,
 2000 Lassen Volcanic Center, California. *California State Fresno Masters Thesis*.
- 2001 Poland, M., Bawden, G., Liwoski, M., Dzurisin, D., 2004. Newly discovered subsidence at Lassen Peak,
 2002 southern Cascade Range, California, from InSAR and GPS. Presented at the AGU Fall
 2003 Meeting, San Fran. Abstract G51A-0068.
- 2004 Poland, M., Bürgmann, R., Dzurisin, D., Lisowski, M., Masterlark, T., Owen, S., Fink, J., 2006.
 2005 Constraints on the mechanism of long-term, steady subsidence at Medicine Lake volcano,
 2006 northern California, from GPS, leveling, and InSAR. *Journal of Volcanology and Geothermal*
 2007 *Research* 150, 55–78. <https://doi.org/10.1016/j.jvolgeores.2005.07.007>
- 2008 Poland, M.P., Lisowski, M., Dzurisin, D., Kramer, R., McLay, M., Pauk, B., 2017. Volcano geodesy in
 2009 the Cascade arc, USA. *Bull Volcanol* 79, 59. <https://doi.org/10.1007/s00445-017-1140-x>
- 2010 Poland, M.P., Miklius, A., Emily, M.-B., 2014. Magma Supply, Storage, and Transport at Shield-Stage
 2011 Hawaiian Volcanoes, in: *Characteristics of Hawaiian Volcanoes*, Professional Paper 1801. U.S.
 2012 Geological Survey, pp. 179–234.
- 2013 Priest, G.R., Hladky, F.R., Mertzman, S.A., Murray, R.B., Wiley, T.J., 2013. Volcanic signature of Basin
 2014 and Range extension on the shrinking Cascade arc, Klamath Falls-Keno area, Oregon. *J.*
 2015 *Geophys. Res. Solid Earth* 118, 4013–4038. <https://doi.org/10.1002/jgrb.50290>

- 2016 Pritchard, M.E., Mather, T.A., McNutt, S.R., Delgado, F.J., Reath, K., 2019. Thoughts on the criteria to
2017 determine the origin of volcanic unrest as magmatic or non-magmatic. *Phil. Trans. R. Soc. A*
2018 377, 20180008. <https://doi.org/10.1098/rsta.2018.0008>
- 2019 Putirka, K., Johnson, M., Kinzler, R., Longhi, J., Walker, D., 1996. Thermobarometry of mafic igneous
2020 rocks based on clinopyroxene-liquid equilibria, 0-30 kbar. *Contributions to Mineralogy and*
2021 *Petrology* 123, 92–108. <https://doi.org/10.1007/s004100050145>
- 2022 Putirka, K.D., 2008. Thermometers and Barometers for Volcanic Systems. *Reviews in Mineralogy and*
2023 *Geochemistry* 69, 61–120. <https://doi.org/10.2138/rmg.2008.69.3>
- 2024 QGIS.org, 2022. QGIS Geographic Information System. <http://www.qgis.org>.
- 2025 Quinn, E., 2014. Experimental Determination of Pre-Eruptive Storage Conditions And Continuous
2026 Decompression of Rhyodacite Magma Erupted from Chaos Crags, Lassen Volcanic Center,
2027 California. MSci thesis, Humboldt State University.
- 2028 Rasmussen, D.J., 2019. The Aleutian arc through and through: Subduction dynamics and the
2029 generation, storage, and eruption of hydrous magmas. Doctor of Philosophy, Columbia
2030 University.
- 2031 Rasmussen, D.J., Plank, T.A., Roman, D.C., Zimmer, M.M., 2022. Magmatic water content controls
2032 the pre-eruptive depth of arc magmas. *Science* 375, 1169–1172.
2033 <https://doi.org/10.1126/science.abm5174>
- 2034 Reeg, H., 2008. Seismic Structure of the Crust and upper Mantle of the Sierra Nevada, California.
2035 MSci Thesis, University of Colorado.
- 2036 Riddick, S.N., Schmidt, D.A., 2011. Time-dependent changes in volcanic inflation rate near Three
2037 Sisters, Oregon, revealed by InSAR. *Geochem. Geophys. Geosyst.* 12, n/a-n/a.
2038 <https://doi.org/10.1029/2011GC003826>
- 2039 Ridolfi, F., 2021. Amp-TB2: An Updated Model for Calcic Amphibole Thermobarometry. *Minerals* 11,
2040 324. <https://doi.org/10.3390/min11030324>
- 2041 Ritter, J.R.R., Evans, J.R., 1997. Deep structure of Medicine Lake volcano, California. *Tectonophysics*
2042 275, 221–241. [https://doi.org/10.1016/S0040-1951\(97\)00022-X](https://doi.org/10.1016/S0040-1951(97)00022-X)
- 2043 Rohay, A., Malone, S.D., 1977. Seismic velocity anomalies in the vicinity of Mt. Baker, Washington
2044 (Abstract). Presented at the Geological Society of America 9 (4).
- 2045 Rowe, M., Thornber, C.R., Gooding, D., Pallister, J., 2008. Catalog of Mount St. Helens 2004 - 2005
2046 Tephra Samples with Major- and Trace-Element Geochemistry. U.S. Geological Survey Open-
2047 File Report 2008-1131.
- 2048 Rudnick, R.L., 1995. Making continental crust. *Nature* 378, 571–578.
2049 <https://doi.org/10.1038/378571a0>
- 2050 Ruscitto, D.M., Wallace, P.J., Johnson, E.R., Kent, A.J.R., Bindeman, I.N., 2010. Volatile contents of
2051 mafic magmas from cinder cones in the Central Oregon High Cascades: Implications for
2052 magma formation and mantle conditions in a hot arc. *Earth and Planetary Science Letters*
2053 298, 153–161. <https://doi.org/10.1016/j.epsl.2010.07.037>
- 2054 Ruscitto, D.M., Wallace, P.J., Kent, A.J.R., 2011. Revisiting the compositions and volatile contents of
2055 olivine-hosted melt inclusions from the Mount Shasta region: implications for the formation
2056 of high-Mg andesites. *Contrib Mineral Petrol* 162, 109–132. <https://doi.org/10.1007/s00410-010-0587-y>
- 2058 Rutherford, M.J., Devine, J.D., 2008. Chapter 31: Magmatic Conditions and Processes in the Storage
2059 Zone of the 2004–2006 Mount St. Helens Dacite, in: *A Volcano Rekindled: The Renewed*
2060 *Eruption of Mount St. Helens, 2004–2006*. Professional Paper 1750-31.
- 2061 Rutherford, M.J., Devine, J.D., 1988. The May 18, 1980, eruption of Mount St. Helens: 3. Stability and
2062 chemistry of amphibole in the magma chamber. *J. Geophys. Res.* 93, 11949.
2063 <https://doi.org/10.1029/JB093iB10p11949>
- 2064 Rutherford, M.J., Sigurdsson, H., Carey, S., Davis, A., 1985. The May 18, 1980, eruption of Mount St.
2065 Helens: 1. Melt composition and experimental phase equilibria. *J. Geophys. Res.* 90, 2929.
2066 <https://doi.org/10.1029/JB090iB04p02929>

- 2067 Ryan, W.B.F., Carbotte, S.M., Coplan, J.O., O'Hara, S., Melkonian, A., Arko, R., Weissel, R.A., Ferrini,
2068 V., Goodwillie, A., Nitsche, F., Bonczkowski, J., Zemsky, R., 2009. Global Multi-Resolution
2069 Topography synthesis. *Geochem. Geophys. Geosyst.* 10, n/a-n/a.
2070 <https://doi.org/10.1029/2008GC002332>
- 2071 Sas, M., DeBari, S., Clynne, M., Rusk, B., 2017. Using mineral geochemistry to decipher slab, mantle,
2072 and crustal input in the generation of high-Mg andesites and basaltic andesites from the
2073 northern Cascade Arc. *msam*. <https://doi.org/10.2138/am-2017-5756>
- 2074 Scandone, R., Malone, S.D., 1985. Magma supply, magma discharge and readjustment of the feeding
2075 system of mount St. Helens during 1980. *Journal of Volcanology and Geothermal Research*
2076 23, 239–262. [https://doi.org/10.1016/0377-0273\(85\)90036-8](https://doi.org/10.1016/0377-0273(85)90036-8)
- 2077 Schmidt, M.E., Grunder, A.L., 2011. Deep Mafic Roots to Arc Volcanoes: Mafic Recharge and
2078 Differentiation of Basaltic Andesite at North Sister Volcano, Oregon Cascades. *Journal of*
2079 *Petrology* 52, 603–641. <https://doi.org/10.1093/petrology/egq094>
- 2080 Schmidt, M.E., Grunder, A.L., Rowe, M.C., 2008. Segmentation of the Cascade Arc as indicated by Sr
2081 and Nd isotopic variation among diverse primitive basalts. *Earth and Planetary Science*
2082 *Letters* 266, 166–181. <https://doi.org/10.1016/j.epsl.2007.11.013>
- 2083 Schwab, B., Castro, J., 2007. PRE-ERUPTIVE STORAGE CONDITIONS OF 1915 LASSEN PEAK DACITE.
2084 Presented at the GSA Denver Annual Meeting.
- 2085 Scott, W.E., Gardner, C., 2017. Field-trip guide to Mount Hood, Oregon, highlighting eruptive history
2086 and hazards:
- 2087 Scott, W.E., Gardner, C., Tilling, R.I., Lanphere, M.A., 1997. Geologic history of Mount Hood Volcano.
2088 Oregon: A Field-Trip Guidebook: U.S. Geological Survey Open-File Report, 97–263.
- 2089 Scruggs, M.A., Putirka, K.D., 2018. Eruption triggering by partial crystallization of mafic enclaves at
2090 Chaos Crags, Lassen Volcanic Center, California. *American Mineralogist* 103, 1575–1590.
2091 <https://doi.org/10.2138/am-2018-6058>
- 2092 Sémhur, 2007. Map of Garibaldi Volcanic Belt. Presented at the
2093 https://commons.wikimedia.org/wiki/File:Garibaldi_Volcanic_Belt-en.svg.
- 2094 Shaw, S., 2011. H₂O contents in olivine-hosted melt inclusions from primitive magmas in the
2095 Northern Cascade arc. Masters Thesis, Western Washington University. MSci thesis, Western
2096 Washington University.
- 2097 Shehata, M.A., Mizunaga, H., 2022. Moho depth and tectonic implications of the western United
2098 States: insights from gravity data interpretation. *Geosci. Lett.* 9, 23.
2099 <https://doi.org/10.1186/s40562-022-00233-y>
- 2100 Sheppard, P.R., Ort, M.H., Anderson, K.C., Clynne, M.A., May, E.M., 2009. Multiple
2101 dendrochronological responses to the eruption of Cinder Cone, Lassen Volcanic National
2102 Park, California. *Dendrochronologia* 27, 213–221.
2103 <https://doi.org/10.1016/j.dendro.2009.09.001>
- 2104 Sherrod, D., Mastin, L., Scott, W., Schilling, S., 1997. Volcano Hazards at Newberry Volcano, Oregon.
2105 USGS Open File Report 97-513.
- 2106 Shishkina, T.A., Botcharnikov, R.E., Holtz, F., Almeev, R.R., Jazwa, A.M., Jakubiak, A.A., 2014.
2107 Compositional and pressure effects on the solubility of H₂O and CO₂ in mafic melts.
2108 *Chemical Geology* 388, 112–129. <https://doi.org/10.1016/j.chemgeo.2014.09.001>
- 2109 Sisson, T.W., Lanphere, M.A., 2000. The geologic history of Mount Rainier volcano. *Washington*
2110 *Geology* (28).
- 2111 Sisson, T.W., Layne, G.D., 1993. H₂O in basalt and basaltic andesite glass inclusions from four
2112 subduction-related volcanoes. *Earth and Planetary Science Letters* 117, 619–635.
- 2113 Sisson, T.W., Salters, V.J.M., Larson, P.B., 2014. Petrogenesis of Mount Rainier andesite: Magma flux
2114 and geologic controls on the contrasting differentiation styles at stratovolcanoes of the
2115 southern Washington Cascades. *Geological Society of America Bulletin* 126, 122–144.
2116 <https://doi.org/10.1130/B30852.1>

- 2117 Sisson, T.W., Schmitt, A.K., Danišik, M., Calvert, A.T., Pempena, N., Huang, C.-Y., Shen, C.-C., 2019.
 2118 Age of the dacite of Sunset Amphitheater, a voluminous Pleistocene tephra from Mount
 2119 Rainier (USA), and implications for Cascade glacial stratigraphy. *Journal of Volcanology and*
 2120 *Geothermal Research* 376, 27–43. <https://doi.org/10.1016/j.jvolgeores.2019.03.003>
- 2121 Sisson, T.W., Vallance, J.W., 2009. Frequent eruptions of Mount Rainier over the last ~2,600 years.
 2122 *Bull Volcanol* 71, 595–618. <https://doi.org/10.1007/s00445-008-0245-7>
- 2123 Smith, D., Leeman, W.P., 1993. The origin of Mount St. Helens Andesites. *Journal of Volcanology and*
 2124 *Geothermal Research* 55 (3).
- 2125 Stanley, W.D., 1984. Tectonic study of Cascade Range and Columbia Plateau in Washington State
 2126 based upon magnetotelluric soundings. *J. Geophys. Res.* 89, 4447–4460.
 2127 <https://doi.org/10.1029/JB089iB06p04447>
- 2128 Stauber, D.A., Green, S.M., Iyer, H.M., 1988. Three-dimensional *P* velocity structure of the crust
 2129 below Newberry Volcano, Oregon. *J. Geophys. Res.* 93, 10095–10107.
 2130 <https://doi.org/10.1029/JB093iB09p10095>
- 2131 Stockstill, K., 1999. The Origin and Evolution of the Burroughs Mountain Lava Flow, Mount Rainier,
 2132 Washington. Michigan State University Masters Thesis.
- 2133 Streck, M.J., Leeman, W.P., 2018. Petrology of “Mt. Shasta” high-magnesian andesite (HMA): A
 2134 product of multi-stage crustal assembly. *American Mineralogist* 103, 216–240.
 2135 <https://doi.org/10.2138/am-2018-6151>
- 2136 Taira, T., Brenguier, F., 2016. Response of hydrothermal system to stress transients at Lassen
 2137 Volcanic Center, California, inferred from seismic interferometry with ambient noise. *Earth*
 2138 *Planets Space* 68, 162. <https://doi.org/10.1186/s40623-016-0538-6>
- 2139 Thornber, C.R., Pallister, J., Rowe, M., McConnell, S., Herriott, T.M., Eckberg, A., 2008. Catalog of
 2140 Mount St. Helens 2004-2007 dome samples with major- and trace-element chemistry.
- 2141 Thurber, C., Zhang, H., Brocher, T., Langenheim, V., 2009. Regional three-dimensional seismic
 2142 velocity model of the crust and uppermost mantle of northern California: N. CALIFORNIA 3-D
 2143 SEISMIC VELOCITY MODEL. *J. Geophys. Res.* 114. <https://doi.org/10.1029/2008JB005766>
- 2144 Till, C.B., Kent, A.J.R., Abers, G.A., Janiszewski, H.A., Gaherty, J.B., Pitcher, B.W., 2019. The causes of
 2145 spatiotemporal variations in erupted fluxes and compositions along a volcanic arc. *Nat*
 2146 *Commun* 10, 1350. <https://doi.org/10.1038/s41467-019-09113-0>
- 2147 Turner, S.J., Izbekov, P., Langmuir, C., 2013. The magma plumbing system of Bezymianny Volcano:
 2148 Insights from a 54year time series of trace element whole-rock geochemistry and amphibole
 2149 compositions. *Journal of Volcanology and Geothermal Research* 263, 108–121.
 2150 <https://doi.org/10.1016/j.jvolgeores.2012.12.014>
- 2151 Ulberg, C.W., Creager, K.C., Moran, S.C., Abers, G.A., Thelen, W.A., Levander, A., Kiser, E., Schmandt,
 2152 B., Hansen, S.M., Crosson, R.S., 2020. Local Source *V_p* and *V_s* Tomography in the Mount St.
 2153 Helens Region With the iMUSH Broadband Array. *Geochem. Geophys. Geosyst.* 21.
 2154 <https://doi.org/10.1029/2019GC008888>
- 2155 Underwood, S.J., Feeley, T.C., Clynne, M.A., 2012. Hydrogen isotope investigation of amphibole and
 2156 biotite phenocrysts in silicic magmas erupted at Lassen Volcanic Center, California. *Journal of*
 2157 *Volcanology and Geothermal Research* 227–228, 32–49.
 2158 <https://doi.org/10.1016/j.jvolgeores.2012.02.019>
- 2159 USGS, 2022. Mt Shasta Hazards.
- 2160 Ustunisik, G., Loewen, M.W., Nielsen, R.L., Tepley, F.J., 2016. Interpretation of the provenance of
 2161 small-scale heterogeneity as documented in a single eruptive unit from Mt. Jefferson,
 2162 Central Oregon Cascades. *Geochem. Geophys. Geosyst.* 17, 3469–3487.
 2163 <https://doi.org/10.1002/2016GC006297>
- 2164 Venezky, D.Y., Rutherford, M.J., 1997. Preeruption conditions and timing of dacite-andesite magma
 2165 mixing in the 2.2 ka eruption at Mount Rainier. *J. Geophys. Res.* 102, 20069–20086.
 2166 <https://doi.org/10.1029/97JB01590>

- 2167 Venugopal, S., Schiavi, F., Moune, S., Bolfan-Casanova, N., Druitt, T., Williams-Jones, G., 2020. Melt
 2168 inclusion vapour bubbles: the hidden reservoir for major and volatile elements. *Sci Rep* 10,
 2169 9034. <https://doi.org/10.1038/s41598-020-65226-3>
- 2170 Wagner, T.P., Donnelly-Nolan, J.M., Grove, T.L., 1995. Evidence of hydrous differentiation and crystal
 2171 accumulation in the low-MgO, high-Al₂O₃ Lake Basalt from Medicine Lake volcano,
 2172 California. *Contrib Mineral Petrol* 121, 201–216. <https://doi.org/10.1007/s004100050099>
- 2173 Waite, G.P., Moran, S.C., 2009. VP Structure of Mount St. Helens, Washington, USA, imaged with
 2174 local earthquake tomography. *Journal of Volcanology and Geothermal Research* 182, 113–
 2175 122. <https://doi.org/10.1016/j.jvolgeores.2009.02.009>
- 2176 Waite, R., Mastin, L.G., Beget, J., 1995. Volcanic Hazard Zonation for Glacier Peak Volcano,
 2177 Washington (USGS Open File report 95-499), Open-File Report.
- 2178 Walowski, K.J., Wallace, P.J., Cashman, K.V., Marks, J.K., Clynne, M.A., Ruprecht, P., 2019.
 2179 Understanding melt evolution and eruption dynamics of the 1666 C.E. eruption of Cinder
 2180 Cone, Lassen Volcanic National Park, California: Insights from olivine-hosted melt inclusions.
 2181 *Journal of Volcanology and Geothermal Research* 387, 106665.
 2182 <https://doi.org/10.1016/j.jvolgeores.2019.106665>
- 2183 Walowski, K.J., Wallace, P.J., Clynne, M.A., Rasmussen, D.J., Weis, D., 2016. Slab melting and magma
 2184 formation beneath the southern Cascade arc. *Earth and Planetary Science Letters* 446, 100–
 2185 112. <https://doi.org/10.1016/j.epsl.2016.03.044>
- 2186 Wang, X., Hou, T., Wang, M., Zhang, C., Zhang, Z., Pan, R., Marxer, F., Zhang, H., 2021. A new
 2187 clinopyroxene McBirney ometer for mafic to intermediate magmatic systems. *Eur. J.*
 2188 *Mineral.* 33, 621–637. <https://doi.org/10.5194/ejm-33-621-2021>
- 2189 Wanke, M., Clynne, M.A., von Quadt, A., Vennemann, T.W., Bachmann, O., 2019. Geochemical and
 2190 petrological diversity of mafic magmas from Mount St. Helens. *Contrib Mineral Petrol* 174,
 2191 10. <https://doi.org/10.1007/s00410-018-1544-4>
- 2192 Waters, L.E., Andrews, B.J., Frey, H.M., 2021. Daly Gaps at South Sister, Oregon, USA, generated via
 2193 partial melting. *Contrib Mineral Petrol* 176, 52. <https://doi.org/10.1007/s00410-021-01805-5>
- 2194 Weaver, C.S., Green, S.M., Iyer, H.M., 1982. Seismicity of Mount Hood and structure as determined
 2195 from teleseismic *P* wave delay studies. *J. Geophys. Res.* 87, 2782.
 2196 <https://doi.org/10.1029/JB087iB04p02782>
- 2197 Weaver, C.S., Norris, R., Jonientz-Trisler, C., 1990. Results of Seismological Monitoring in the Cascade
 2198 Range, 1962-1989: Earthquakes, eruptions, avalanches and other curiosities. *Geoscience*
 2199 *Canada* 17(3), 158–162.
- 2200 White, R., McCausland, W., 2016. Volcano-tectonic earthquakes: A new tool for estimating intrusive
 2201 volumes and forecasting eruptions. *Journal of Volcanology and Geothermal Research* 309,
 2202 139–155. <https://doi.org/10.1016/j.jvolgeores.2015.10.020>
- 2203 Wicks, C.W., 2002. Magmatic activity beneath the quiescent Three Sisters volcanic center, central
 2204 Oregon Cascade Range, USA. *Geophys. Res. Lett.* 29, 1122.
 2205 <https://doi.org/10.1029/2001GL014205>
- 2206 Wieser, P., Gleeson, M.L.M., Matthews, S., DeVitre, C.L., Gazel, E., 2023c. Determining the Pressure –
 2207 Temperature – Composition (P-T-X) conditions of magma storage. *EarthArxiv Preprint*.
 2208 doi.org/10.31223/X50M44.
- 2209 Wieser, P., Iacovino, K., Matthews, S., Moore, G., Allison, C., 2022c. VESlcal Part II: A critical
 2210 approach to volatile solubility modelling using an open-source Python3 engine (preprint).
 2211 *Earth Sciences*. <https://doi.org/10.31223/X5K03T>
- 2212 Wieser, P. E., Edmonds, M., Gansecki, C., Maclennan, J., Jenner, F.E., Kunz, B., Antoshechkina, P.,
 2213 Trusdell, F., Lee, R.L., Eimf, 2022b. Explosive Activity on Kilauea’s Lower East Rift Zone Fueled
 2214 by a Volatile-Rich, Dacitic Melt. *Geochem Geophys Geosyst* 23.
 2215 <https://doi.org/10.1029/2021GC010046>

- 2216 Wieser, P.E., Kent, A.J., Till, C., 2023b. Barometers behaving badly II: A critical evaluation of Cpx-only
2217 and Cpx-Liq thermobarometry in variably-hydrous arc magmas. EarthArxiv.
2218 <https://doi.org/10.31223/X59655>
- 2219 Wieser, Penny E, Kent, A.J.R., Till, C.B., Donovan, J., Neave, D.A., Blatter, D.L., Krawczynski, M.J.,
2220 2023a. Barometers Behaving Badly I: Assessing the Influence of Analytical and Experimental
2221 Uncertainty on Clinopyroxene Thermobarometry Calculations at Crustal Conditions. *Journal*
2222 *of Petrology* 64, egac126. <https://doi.org/10.1093/petrology/egac126>
- 2223 Wieser, P.E., Lamadrid, H., Maclennan, J., Edmonds, M., Matthews, S., Iacovino, K., Jenner, F.E.,
2224 Gansecki, C., Trusdell, F., Lee, R.L., Ilyinskaya, E., 2021. Reconstructing Magma Storage
2225 Depths for the 2018 Kīlauean Eruption From Melt Inclusion CO₂ Contents: The Importance
2226 of Vapor Bubbles. *Geochem Geophys Geosyst* 22. <https://doi.org/10.1029/2020GC009364>
- 2227 Wieser, P.E., Petrelli, M., Lubbers, J., Wieser, E., Ozaydin, S., Kent, A., Till, C., 2022. Thermobar: An
2228 open-source Python3 tool for thermobarometry and hygrometry. *Volcanica* 5, 349–384.
2229 <https://doi.org/10.30909/vol.05.02.349384>
- 2230 Wong, Y., Segall, P., 2020. Joint Inversions of Ground Deformation, Extrusion Flux, and Gas Emissions
2231 Using Physics-Based Models for the Mount St. Helens 2004–2008 Eruption. *Geochem.*
2232 *Geophys. Geosyst.* 21. <https://doi.org/10.1029/2020GC009343>
- 2233 Wright, H.M., Bacon, C.R., Vazquez, J.A., Sisson, T.W., 2012. Sixty thousand years of magmatic
2234 volatile history before the caldera-forming eruption of Mount Mazama, Crater Lake, Oregon.
2235 *Contrib Mineral Petrol* 164, 1027–1052. <https://doi.org/10.1007/s00410-012-0787-8>
- 2236 Zhang, H., Thurber, C.H., Shelly, D., Ide, S., Beroza, G.C., Hasegawa, A., 2004. High-resolution
2237 subducting-slab structure beneath northern Honshu, Japan, revealed by double-difference
2238 tomography. *Geol* 32, 361. <https://doi.org/10.1130/G20261.2>
- 2239 Zucca, J.J., Evans, J.R., 1992. Active high-resolution compressional wave attenuation tomography at
2240 Newberry Volcano, Central Cascade Range. *J. Geophys. Res.* 97, 11047.
2241 <https://doi.org/10.1029/92JB00492>
2242